FEEDBACK PROCESSES IN ASTROPHYSICAL SYSTEMS FROM GALAXIES TO CLUSTERS: A MULTI-WAVELENGTH APPROACH

DISSERTATION

zur Erlangung des Doktorgrades
an der Fakultät für Mathematik, Informatik und Naturwissenschaften
Fachereich Physik
der Universität Hamburg

vorgelegt von
KATHRIN MARIA BÖCKMANN

Hamburg
2023

Gutachter der Dissertation: Prof. Dr. Marcus Brüggen
Prof. Dr. Francesco de Gasperin

Zusammensetzung der Prüfungskommission: Prof. Dr. Marcus Brüggen
Prof. Dr. Francesco de Gasperin
Prof. Dr. Stephan Rosswog
Prof. Dr. Jochen Liske
Prof. Dr. Peter Hauschildt

Vorsitzender der Prüfungskommission: Prof. Dr. Jochen Liske

Datum der Disputation: 07.12.2023

Vorsitzender des Fach-Promotionsausschusses PHYSIK: Prof. Dr. Markus Drescher

Leiter des Fachbereichs PHYSIK: Prof. Dr. Wolfgang J. Parak

Dekan der Fakultät MIN: Prof. Dr. Norbert Ritter

Design your own Universe

In memory of
Ludger Böckmann
1948-2017

Eidesstattliche Versicherung

Hiermit versichere ich an Eides statt, die vorliegende Dissertationsschrift selbst verfasst und keine anderen als die angegebenen Hilfsmittel und Quellen benutzt zu haben.

Hamburg, den 07.10.2023

(Kathrin Böckmann)

Zusammenfassung

Extragalaktische Systeme wie Galaxien und Galaxienhaufen sind keine statischen Objekte, die in definierten räumlichen Grenzen eingegrenzt sind. Vielmehr handelt es sich um dynamische und ständig wachsende und sich entwickelnde Einheiten. Das Wachstum dieser Objekte im großen Maßstab wird von verschiedenen astrophysikalischen Rückkopplungsereignissen beeinflusst, darunter Supernovae, galaktische Winde und Aktivitäten von Schwarzen Löchern, die zu Materiezu- und -abflüssen führen. Diese Ereignisse haben eine Reichweite, die über die Systeme selbst hinausgeht, und beeinflussen die größere kosmische Umgebung. Diese Arbeit untersucht die Wechselwirkungen zwischen Galaxien, dem umgebenden circum-galaktischen Medium (CGM) individueller Galaxien und Galaxienhaufen, wobei der Schwerpunkt auf Rückkopplungsmechanismen unter Verwendung von Survey-Daten von verschiedenen Teleskopen liegt.

Insgesamt werden drei verschiedene Projekte vorgestellt, die unterschiedliche Rückkopplungsmechanismen und deren Auswirkungen auf das Strukturwachstum untersuchen. Im ersten Projekt verwenden wir Radiobeobachtungen des MeerKAT-Teleskops, um Magnetfelder im CGM zu messen. Wir haben die Rotationsmaße um vordergründige sternenbildende Galaxien herum gemessen, um die Stärke des Magnetfelds im CGM abzuleiten. Im zweiten Projekt verwenden wir Röntgendaten des eROSITA-Teleskops, öffentliche optische Daten aus der Legacy Survey und Radio-Daten des ASKAP-Teleskops, um die Rückkopplung durch aktive galaktische Kerne in Galaxienhaufen zu untersuchen. Im dritten Projekt stacken wir Daten des ACT-Teleskops, um den thermischen Sunyaev-Zel'dovich-Effekt um massereiche Galaxien herum zu messen und die Rückkopplung durch aktive galaktische Kerne zu untersuchen und wie sie das CGM dieser Galaxien beeinflusst.

Zusammenfassend untersuchen diese Studien das komplexe Wechselspiel zwischen dem Gas in Galaxien, dem CGM und Galaxienhaufen, wobei der Schwerpunkt insbesondere auf rückkopplungsinduzierten Prozessen wie Ein- und Ausströmungen von Gas und deren Auswirkungen auf das Strukturwachstum liegt. All diese Arbeiten haben gemeinsam, dass der Vergleich unserer Beobachtungsdaten mit Simulationsdaten Diskrepanzen aufzeigt. Dies verdeutlicht die Notwendigkeit von numerischen Simulationen mit höherer Auflösung, die unterschiedliche Randbedingungen berücksichtigen, sowie die Notwendigkeit von neuen Teleskopen, die tiefere Daten generieren und größere Himmelsbereiche abdecken.

Abstract

Extragalactic systems, such as galaxies and galaxy clusters, are not static objects confined within defined spatial boundaries; rather, they are dynamic and continually evolving and growing. The growth of these objects on a large-scale is influenced by various astrophysical feedback events, including supernovae, galactic winds, and black hole activity, leading to inflows and outflows of matter. These events have a reach that extends beyond the systems themselves, impacting the larger cosmic environment. This thesis explores the interactions between galaxies, the circumgalactic medium (CGM) which surrounds the individual galaxies and galaxy clusters, focusing on feedback mechanisms using survey data from different telescopes.

Three projects are presented that investigate different feedback mechanisms and their impact on structure growth. In the first project we use radio observations from the MeerKAT telescope to measure magnetic fields in the CGM. We measure the rotation measure around foreground star-forming galaxies to derive constraints on the magnetic field strength of the CGM. In the second project we use X-ray data from the eROSITA telescope, public optical data from the legacy survey and radio data from the ASKAP telescope to investigate feedback from Active Galactic Nuclei (AGN) in galaxy clusters. In the third project we stack data from the ACT telescope to measure the thermal Sunyaev-Zel'dovich effect around massive galaxies to study AGN feedback and how it affects the CGM of these galaxies.

Collectively, these studies investigate the complex interplay between the gas contained in galaxies, the CGM and clusters, especially focusing on feedback induced processes like in- and outflows of gas and how these processes affect the structure growth. All these works have in common that comparisons of our observational data with simulation data reveal discrepancies. This demonstrates the need for numerical simulations with higher resolution that take into account different boundary conditions, as well as the need for new telescopes that generate deeper data and cover larger celestial areas.

Previous publications

This thesis is based on (but does not include all of) the following publications, which I have led as first author or took part to as co-author:

- E. Bulbul, A. Liu, M. Kluge, X. Zhang, J. S. Sanders, Y. E. Bahar, V. Ghirardini, E. Artis, R. Seppi, C. Garrel, M. E. Ramos-Ceja, J. Comparat, F. Balzer, K. Böckmann, M. Brüggen, N. Clerc, K. Dennerl, K. Dolag, M. Freyberg, S. Grandis, 5, D. Grün, F. Kleinebreil, S. Krippendorf, G. Lamer, A. Merloni, K. Migkas, K. Nandra, F. Pacaud, P. Predehl, T. H. Reiprich, T. Schrabback, 8, A. Veronica, J. Weller, S. Zelmer, "The SRG/eROSITA All-Sky Survey - The First Catalog of Galaxy Clusters and Groups in the Western Galactic Hemisphere", 2023 A&A, submitted
- K. Böckmann, M. Brüggen, V. Heesen, A. Basu, S. P. O'Sullivan, I. Heywood, M. Jarvis, A. Scaife, J. Stil, R. Taylor, N. J. Adams, R. A. A. Bowler, M. N. Tudorache, "Probing magnetic fields in the circumgalactic medium using polarization data from MIGHTEE", 2023, A&A, Volume 678, A56
- K. Böckmann, M. Brüggen, B. Koribalski, A. Veronica, T. H. Reiprich, E. Bulbul, Y. E. Bahar, F. Balzer, J. Comparat, C. Garrel, V. Ghirardini, G. Gürkan, M. Kluge, D. Leahy, A. Merloni, A. Liu, M. E. Ramos-Ceja, M. Salvato, J. Sanders, S. Shabala, X. Zhang, "Central radio galaxies in galaxy clusters: Joint surveys by eROSITA and ASKAP", 2023, A&A, Volume 677, A188
- J. Meinke, S. Cohen, J. Moore, K. Böckmann, P. Mauskopf, E. Scannapieco, "Evidence of Extended Dust and Feedback around z$\sim$1 Quiescent Galaxies via Millimeter Observations", 2023, The Astrophysical Journal, Volume 954, Issue 2, id.119, 21 pp.
- J. Meinke, K. Böckmann, S. Cohen, P. Mauskopf, E. Scannapieco, R. Sarmento, E. Lunde, J. Cottle, "The Thermal Sunyaev-Zel'dovich Effect from Massive, Quiescent 0.5 $\lesssim$ z $\lesssim$ 1.5 Galaxies", 2021, The Astrophysical Journal, Volume 913, Issue 2, id.88, 14 pp.

Contents

1 Introduction

The journey through extragalactic astrophysics began with the work of Edwin Hubble in the early 20th century, who, through observations of Cepheid variable stars and their redshifts, established a correlation between distance and redshift in galaxies now famously known as Hubble's Law. Hubble's Law transformed our perspective on the universe, revealing an expanding cosmos and laying the foundation for the modern field of extragalactic astronomy. Today we are capable of observing extragalactic targets from neighboring galaxies in our local galaxy group to distant galaxy clusters and quasars that have formed shortly after the big bang. Observations across the whole magnetic spectrum are used to identify and to characterize these sources and the detection of many galaxies and galaxy clusters across a wide redshift range is crucial to examine and understand cosmological problems. Extragalactic systems, like galaxies and galaxy clusters, are far from static entities confined to defined boundaries. They are dynamic and constantly evolving, influenced by various astrophysical events like supernovae, galactic winds, and black hole activity, which lead to the movement of matter in and out of these systems. These events have broader implications, impacting the larger cosmic environment. This thesis explores how galaxies interact with the surrounding circumgalactic medium, with a particular focus on the feedback mechanisms involved.

In general, feedback refers to the interactions between different components of an astrophysical system that can regulate the behavior of the system and affect its evolution over time, playing an important role in shaping the structures in the Universe. Astrophysical feedback processes describe mechanisms through which various astrophysical phenomena influence and regulate the formation and evolution of galaxies, stars, and other cosmic structures. These processes involve the exchange of energy, momentum, and matter between different components of a system, leading to complex interactions and self-regulation.
One example on small scales is stellar feedback, where the energy and momentum generated by stars and their remnants can influence the surrounding gas and dust, leading to changes in the rate of star formation. This feedback can regulate the star formation process, slowing it down or even halting it when conditions become unfavorable. After giving a short introduction on galaxy evolution and galaxies itself in section 1.1 and section 1.2 stellar feedback is described in more detail in section 1.2.3.
An example on larger scales is feedback from Active Galactic Nuclei (AGN, see section 1.2.5), where the energy released by the accretion of matter onto a black hole can impact the surrounding gas and dust, leading to changes in the structure and behavior of the host galaxy. This feedback can regulate the growth of the black hole and influence the star formation and evolution of the galaxy, its surrounding medium and even a whole galaxy cluster.

A medium highly sensitive to feedback processes is the circumgalactic medium (CGM) (section 1.3). The CGM is the medium surrounding a galaxy and is typically defined up to the virial radius, which describes the size of a gravitationally bound halo. The CGM hosts many interactions: Feedback processes usually eject a significant fraction of gas out of the galaxy into the CGM. This gas then heats the CGM by interacting with the cold gas accreted by cosmic filaments. As the CGM acts as a gas reservoir for the fueling of star-formation of a galaxy it is basically sensitive to all kinds of feedback, including feedback from magnetic fields, stellar and AGN feedback. Magnetic fields and magnetic field detection in the CGM are the topics of section 1.3.6 and section 1.3.7.

If we zoom out even further and observe even larger areas than individual galaxies and their CGM, we eventually reach the largest coherent structures in the universe: Galaxy clusters. Clusters are the largest gravitationally bound systems in the Universe and are also subject to feedback processes, especially to AGN feedback originating from the clusters brightest central galaxy (BCG). Galaxy clusters are described in section 1.4. One method to find and examine clusters also in terms of how AGN feedback influences the ICM and CGM is to detect the thermal Sunyaev-Zel'dovich effect, which is subject of section 1.4.1.
After introducing the theoretical background on the topics mentioned above, three scientific projects are described in chapter 2, chapter 3 and chapter 4, where we use different observation techniques and surveys to study feedback processes in extragalactic systems. We conclude this thesis in chapter 5.

1.1 Galaxy Evolution

In our Universe, structures form via the gravitational instability of an initially overdense region. An overdense region interacts with the surrounding matter via gravity and attracts matter towards its center so that the overdensity increases. In the early Universe, the distribution of matter was approximately uniform with slight variations in density originating from inflationary processes. Initially, the density fluctuations grew linearly due to cosmic expansion until gravitational attraction became dominant in regions with higher densities. This resulted in the collapse of dark matter into self-gravitating halos, which are the sites for galaxy formation. The spatial distribution and mass spectrum of these halos, known as the halo mass function and correlation functions, respectively, are solely determined by the power spectrum of the initial density fluctuations.

During the process of dark matter collapse, gas accretes onto the halo and experiences heating to the virial temperature due to accretion shock. However, before the gas can move into the central region of the halo and form stars, it must undergo cooling. Several cooling mechanisms are important, such as bremsstrahlung (free-free) for temperatures greater than 10^6 K, metal-line cooling between 10^5 – 10^6 K, and atomic cooling for hydrogen and helium temperatures ranging from 10^4 – 10^5 K. Additionally, various heating mechanisms exist, including Compton heating, photoionization and photoelectric heating from black hole accretion, stellar sources, cosmic ray heating and shocks from supernova ejecta, outflows and accretion shocks. These processes contribute to the multi-phase nature of the interstellar medium (ISM) and the CGM, where hot ionized gas, warm neutral gas, and cold molecular gas coexist in equipartition.

In general, galaxy formation can be seen as a competition of inflows and outflows to regulate the fuel supply for star formation and black hole growth. When cold gas with temperatures below 10^5 K condenses it begins to form stars. This gas is primarily composed of hydrogen but also contains traces of metals. The star formation embeds the baryons to the stars throughout the stars lifespan. When a star runs out of hydrogen fuel the resulting supernova drives gas and energy from the local region of a galaxy to its outer regions and ejects chemical enriched gas from the galaxy into the surrounding medium. If the ejected gas starts to cool and condenses again it is available to another process of star-formation, resulting in stars with higher fractions of metals and subsequently higher metallicity.

The evolution of galaxies is significantly influenced by environmental effects arising from halo mergers, such as gas stripping via ram pressure and galaxy mergers. These physical processes play crucial roles in shaping the evolution of galaxies. Also, feedback processes play an important role in shaping the properties and growth of galaxies and galaxy clusters over cosmic time scales. Two types of feedback processes can be described: *Positive* feedback and *negative* feedback. *Positive* feedback involves the amplification of certain processes within galaxies, often triggered by the formation of massive stars or supermassive black holes. This amplification can lead to accelerated star formation rates, the dispersal of gas and metals, and the initiation of galactic outflows. *Negative* feedback, in turn, acts as a regulatory mechanism, damping excessive growth and ensuring a balance within galaxies and their surroundings. It involves processes such as supernova explosions, AGN outbursts and radiation pressure. These mechanisms can suppress star formation, expel gas from galaxies, and even quench the activity of supermassive black holes. For detailed reviews on galaxy evolution we refer to e.g. Dodelson & Efstathiou (2004); Naab & Ostriker (2017); Silk & Mamon (2012); Somerville & Davé (2015a)).

1.2 Galaxies

Galaxies are optically visible structures that populate the Universe. They consist of stars, gas, dust and dark matter and are held together by gravity. Galaxies are visible in the optical regime as stars are made up of baryonic matter that emit electromagnetic radiation. Ranging in size from dwarf galaxies with masses of $\sim 10^9$ $\mathrm{M}_\odot$ to massive galaxies with masses of $\sim 10^{11}$ $\mathrm{M}_\odot$, galaxies exhibit a variety of shapes, sizes, and properties (Labbé et al., 2023; Revaz & Jablonka, 2018). Galaxies are usually categorized based on their morphology: Elliptical galaxies, disc galaxies and irregular galaxies (Blanton & Moustakas, 2009; Mo et al., 2010). Fig. 1.1 shows an example for each of these galaxy types captured by the Hubble Space Telescope (HST). In this work we especially focus on star-forming disc galaxies and massive elliptical galaxies, which are described in detail below.

1.2.1 Star-forming Disc Galaxies

A disc galaxy is a type of galaxy characterized by a prominent, flattened disk component. This disc structure is composed of stars, gas, and dust, and it usually exhibits rotational motion. Disc galaxies can be further classified into different types, including spiral galaxies, lenticular

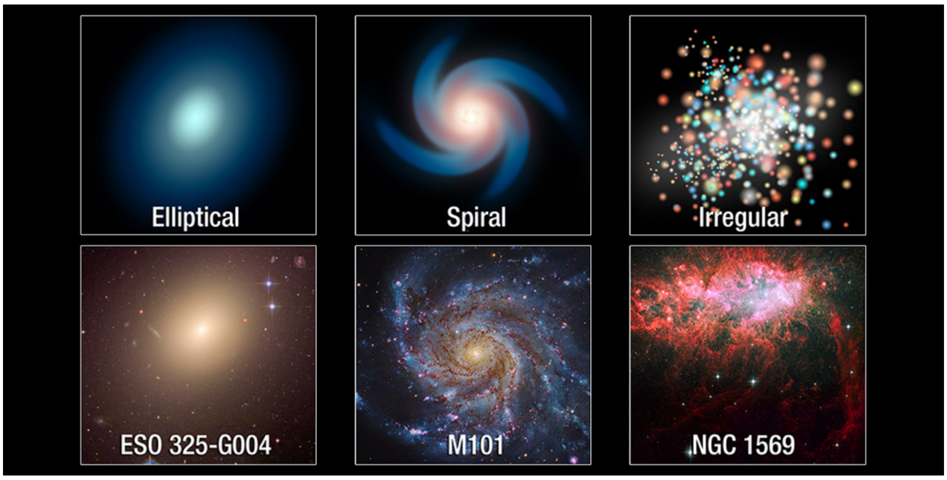

Figure 1.1 This graphic compares illustrations of the three main types of galaxies (top) with HST observations of galaxies (bottom) that fit the three categories: Massive elliptical galaxies, spiral disc galaxies and irregular galaxies. Credit: A. Feild (STScI)

galaxies, and irregular galaxies, based on additional features and characteristics. Star-forming disc galaxies begin with vast clouds of molecular gas and dust, the materials from which stars are born. Gravity initiates the collapse of these gas clouds, giving rise to protostellar cores. As these cores condense further, nuclear fusion ignites, marking the birth of stars. These new stars light up the spiral arms of the galaxy, forming the patterns that trace the density waves within the disc.

In a disc galaxy, the stars and other material within the disk orbit around a central bulge or nucleus. The disk component of a disc galaxy is often rich in interstellar gas and dust, which provides the fuel for ongoing star formation. The stars contained in the disk are typically younger, as the active star-forming regions are primarily located within the disk. These young stars are often found in the spiral arms of spiral galaxies or scattered throughout the disk of lenticular galaxies. Massive, hot, blue stars blaze brightly and live relatively short lives, while cooler, redder stars shine more dimly and persist for longer timescales. Supernovae inject new elements into the interstellar medium, enriching it with heavier elements. These elements then become the building blocks for the next generation of stars. Star formation is a balance between gravity's pull and various feedback mechanisms that limit further growth. The energy and winds released by massive stars create bubbles and channels in the surrounding gas, dispersing it and suppressing further star formation. Stellar radiation also exerts pressure on the gas, preventing it from collapsing into new stars too rapidly. This intricate interplay between star formation and feedback maintains the galaxy's equilibrium and regulates its evolutionary trajectory. For more about these types of galaxies we refer to e.g. work of Dutton & van den Bosch (2012); Kormendy (2016); Mo et al. (2010).

1.2.2 Massive Elliptical Galaxies

In distinction to star-forming disc galaxies with high star-formation rates, we also find old massive elliptical galaxies populating the universe. Elliptical galaxies are more massive systems than disc galaxies reaching stellar masses up to $\mathrm{M}_* \sim 10^{12}\mathrm{M}_\odot$. They often reside in centers of gravitationally bound systems such as galaxy groups and clusters. Massive galaxies form slowly over cosmic epochs through smaller galaxies that collide and merge, gradually building up their mass. During these interactions stars are torn from their orbits, gas is stripped away, and gravitational forces reshape the galaxies structures. The aftermath of these collisions often results in the creation of a single, massive elliptical galaxy at the center of the newly formed galaxy cluster. Massive elliptical galaxies exhibit a distinct structure characterized by a smooth, featureless and spheroidal structure. Unlike the spiral arms of disc shaped star-forming galaxies, these massive elliptical galaxies lack ongoing star formation and are composed mostly of older stars. The tightly packed stars within them create a gravitational environment conducive to rapid interactions and mergers, further fueling their growth. At the cores of massive elliptical galaxies resides a supermassive black hole (SMBH). These SMBHs play an important role in galactic dynamics: As they accrete surrounding material, they emit intense radiation, generating quasars or active galactic nuclei. The feedback from these central engines can influence star formation, heat surrounding gas, and regulate the growth of the galaxy itself. For a more detailed description about the formation and characteristics of massive elliptical galaxies we refer to e.g. Kormendy (2016).

1.2.3 Stellar Feedback

Continuing our journey from star-forming disc galaxies to massive elliptical galaxies, the next important step is to understand stellar feedback, which is a fundamental factor in galaxy dynamics and evolution. Stellar feedback processes are all interactions of stars with the surrounding interstellar medium (ISM) of the galaxy. This includes radiation pressure, ionizing radiation, protostellar jets, stellar winds and supernovae. These feedback effects are able to move gas by momentum as well as to increase the thermal energy. Hence, stellar feedback processes are distinguishable as momentum-driven and energy-driven. Cooling in the ISM is very efficient at low temperatures, but this efficiency drops at higher temperatures and lower densities. If the cooling time is very large, the feedback effect is more energy conserving and a longer cooling time also increases the energy sustainability. In turn, if the cooling time is short, momentum drives the expansion and energy is lost (Krumholz, 2015). The individual processes differ in their influence on the ISM and the importance of these processes can therefore be measured by their individual impact.

One specific example for stellar feedback are stellar winds. Stellar winds of massive stars show typical mass loss rates of the order of $1\ \mathrm{M}_\odot\ \mathrm{Myr}^{-1}$ and wind velocities of a few $1000\ \mathrm{km\ s}^{-1}$. Stars with masses of more than $60\ \mathrm{M}_\odot$ can exceed these values, resulting in a cumulative wind luminosity over the lifetime of 10^{51} erg which is equivalent to a supernova explosion (Kudritzki & Puls, 2000). The importance of stellar winds is highly discussed (Naab & Ostriker, 2017). Some simulations suggest that at galactic scales winds are negligible (Hopkins, 2014). Other simulations indicate that stellar winds are a strong regulator for the star formation rate, as

they prevent gas accretion on stars and reduce Jeans-unstable gas at larger scales Gatto et al. (2015, 2017).
In contrast to the steady process of stellar winds, the explosion and subsequent feedback of a massive star as a supernova is a singular event. A supernova releases 10^{51} erg, resulting in a supersonic shock expanding into the surrounding medium that is heated up to temperatures of 10^6 K. Supernovae create hot gas as well as imparting momentum into the gas during a multi staged evolution. The supernova remnant distributes metals and is a major source of X-rays and cosmic rays.

Stellar feedback processes predominantly occur within galaxies, particularly in regions with active star formation. These regions, often found in spiral arms or within massive star clusters, provide the ideal conditions for massive stars to form and subsequently drive these feedback mechanisms. The impact of stellar feedback can be observed in the morphology, chemical composition, and overall evolution of galaxies, demonstrating interplay between stars and their environments.

1.2.4 Radio Galaxies/Active Galactic Nuclei

Galaxies are not only visibile in the optical regimes via their emitted starlight, many galaxies are also sources of radio emission. The non-thermal radio emission of galaxies can come from two different types of sources: Galactic halos or Active Galactic Nuclei (AGN). Almost every galaxy hosts a supermassive black hole (mass $> 10^6$ $M_\odot$) in the center, but only a small fraction ($\sim 3\%$) of galaxies have *active* SMBHs, which are particularly found in massive elliptical galaxies (Rosswog & Brüggen, 2011). These black holes grow mainly through episodes of radiatively-efficient accretion of gas, when they become extremely luminous and visible as AGN. When the nucleus of a galaxy is active, the SMBH at its center accretes nearby material, whereby gravitational potential is converted to kinetic energy and thermal radiation. In some cases, the energy release can produce two relativistic jets that extend up bipolar and symmetric to scales of a few hundred kiloparsecs (kpc) from the galactic center. The accretion disk, torus, and corona of an AGN emits over the whole electromagnetic spectrum: Radio, infrared, optical, UV and X-ray wavelengths. However, the jets that consist of a plasma of relativistic particles, which is propelled by magnetic fields, emit synchrotron radiation in the radio regime. The radio jets of an AGN can extend up to hundreds of kpc into the intergalactic medium, beyond the optical bulge of its host galaxy. Active radio galaxies are transient sources with a duty cycle that can change the morphology of their emission. The spectral properties, sizes and shapes of radio galaxies can vary on timescales of months to many years (Morganti, 2017).

When observing a galaxy cluster (section 1.4) at radio frequencies, the brightest sources of emission are typically arising from active galaxies within the clusters. Most clusters host large, elliptical galaxies called the brightest cluster galaxies (BCGs) that reside at the cluster center in the minimum of the cluster potential well. BCGs are very likely to be radio loud, with compact or extended AGN radio emission (Best et al., 2007; Lin & Mohr, 2004).
AGN are capable of releasing $\sim 10\%$ of the rest-mass energy of accreted material into their surroundings, which has an impact on the host galaxy (Marconi et al., 2004). It has the potential to modify the condition of the gas and influence the star-formation in the host, an effect

which is called *AGN feedback*. In local galaxies, the black hole mass correlates tightly with the central velocity dispersion and the bulge mass, suggesting either co-evolution or feedback regulation between SMBHs and their host galaxies (Fabian, 2012; McConnell & Ma, 2013). AGN feedback is described in detail in the next section section 1.2.5.

1.2.5 AGN Feedback

Feedback from AGN refers to the processes by which the central SMBHs of galaxies influence their host galaxies and the surrounding interstellar and intergalactic medium. Two different modes of AGN feedback are found in observations: The *radiative* or quasar mode and the *radio* or jet mode (Cattaneo et al., 2009; Heckman & Best, 2014). The radiative mode is responsible for uniform heating and ionization of the environment around it by the radiation emitted by an AGN. This can have a dual effect on star formation: On one hand, it can promote star formation by compressing gas and triggering its collapse. On the other hand, it can suppress star formation by heating and dispersing gas, making it more difficult for new stars to form. The balance between these effects depends on the intensity and duration of the AGN activity. In radio mode AGN jets expel radio-heated gas from the accreting black hole matter outwards into the ICM and push away the existing X-ray heated cluster gas (Shabala et al., 2020). AGN can launch powerful jets of high-speed particles and radiation into the interstellar and intergalactic medium. These jets can shock and push aside gas, creating cavities and bubbles in the surrounding medium. As these structures expand, they can influence the rate of star formation by compressing or displacing gas clouds. Therefore, also radio mode AGN is a dual effect on star formation. AGN activity in form of radio jets prevents the cooling of gas and subsequent star formation, but also contribute to star formation by projecting jets towards the ICM and compressing the gas. An increment of radiative losses of the ICM leads to an increment in heating of the gas by the AGN in turn. The more gas cools the higher the energy output that is able to quench the radiative losses. This is known as the *AGN feedback loop* (Gaspari et al., 2020; McNamara et al., 2016a).

Magnetic fields in accretion disks play a crucial role in the accretion process. They can transport angular momentum, channeling matter onto the central object while also regulating the rate of accretion through magnetic braking and disk winds. Jets are highly collimated, energetic outflows of matter that are observed in various astrophysical objects, including young stellar objects, active galactic nuclei, and neutron stars. Magnetic fields are thought to be responsible for launching and collimating these jets. The interaction between the magnetic field and the accretion disk or the rotating central object provides the mechanism to extract energy and momentum from the system, driving the jet.

AGN feedback has been observed in a wide range of systems from isolated elliptical galaxies to massive clusters. The most powerful AGN operating in radio mode can be found in the brightest cluster galaxies (BCGs) that are usually massive elliptical galaxies residing at the bottom of the clusters potential (e.g. reviews by Fabian (2012), Gitti et al. (2012), (McNamara & Nulsen, 2012)). Deep X-ray observations with X-ray telescopes like *XMM-Newton* and *Chandra* have revealed that most of the systems with radio mode AGN show disturbed X-ray morphologies caused by AGN ejected jets. These surface brightness features, including

cavities in the X-ray images and sharp density discontinuities interpreted as shocks, indicate a strong correlation between the ICM and the central AGN. The thermodynamical properties of the intracluster gas is also affected by AGN feedback in terms of the gas entropy distribution and transport of high-metallicity gas from the center of the cluster to its outskirts. The X-ray cavities or bubbles that have been discovered in X-ray images of clusters are often filled with radio emission. This leads to the assumption that radio plasma produced by AGN outflows displace the X-ray emitting gas of the ICM. One of the main results of these observations was the revelation of a scaling relation between the cavity power and the radio luminosity (Bîrzan et al., 2020; Birzan et al., 2004; Rafferty et al., 2006; Timmerman et al., 2022).
AGN feedback does not only act on cluster size scales but it has significant effects on the CGM, which is the tenuous and extended region of gas surrounding galaxies but outside their central regions. For example, AGN feedback can influence the metal enrichment of the CGM. The outflows generated by AGN can carry enriched material, including heavy elements produced in supernovae, into the CGM. This process can contribute to the enrichment of the CGM with elements heavier than hydrogen and helium. AGN feedback can also regulate the overall in- and outflow of gas in the CGM. While AGN-driven outflows can expel gas from galaxies and into the CGM, the feedback process can also compress CGM gas and lead to accretion onto galaxies.

Fig. 1.2 illustrates the self-regulated multiphase AGN feeding and feedback cycle on three scales: Micro, meso and macro. The larger macro halo includes galaxies, groups, or clusters. The normalization length is associated with either the virial radius or the Schwarzschild radius. The lower insets of the image illustrate crucial phases of the feeding cycle. This includes the representation of multiphase condensation rain from the turbulent X-ray plasma halo, followed by the growth of the central SMBH through the chaotic cold accretion phase. In the upper insets, key stages of the feedback cycle are portrayed. This includes the generation of hot X-ray ultrafast outflows and focused relativistic jets, the interaction of multi-phase ambient gas (or its potential in-situ formation), and the eventual release of AGN heating involving elements such as bubbles, shocks, and turbulence.

1.3 The Circumgalactic Medium

The diffuse gas embedded between the interstellar medium (ISM) and the baryon-rich intergalactic medium (IGM) of a galaxy is known as the circumgalactic medium (CGM) or the 'galaxy corona'. The existence of this extended gaseous halo has been a fundamental prediction of galaxy formation theory since (White & Frenk, 1991). Observations and simulations from all across the whole electromagnetic spectrum and redshifts suggest that the CGM gas has a major impact on galaxy evolution and two roles in the chemical history and evolution of a galaxy: It receives enriched material that was expelled in the form of outflows, but it also acts as a reservoir of fuel for future star formation, including the infalling IGM gas (Machado et al., 2018).

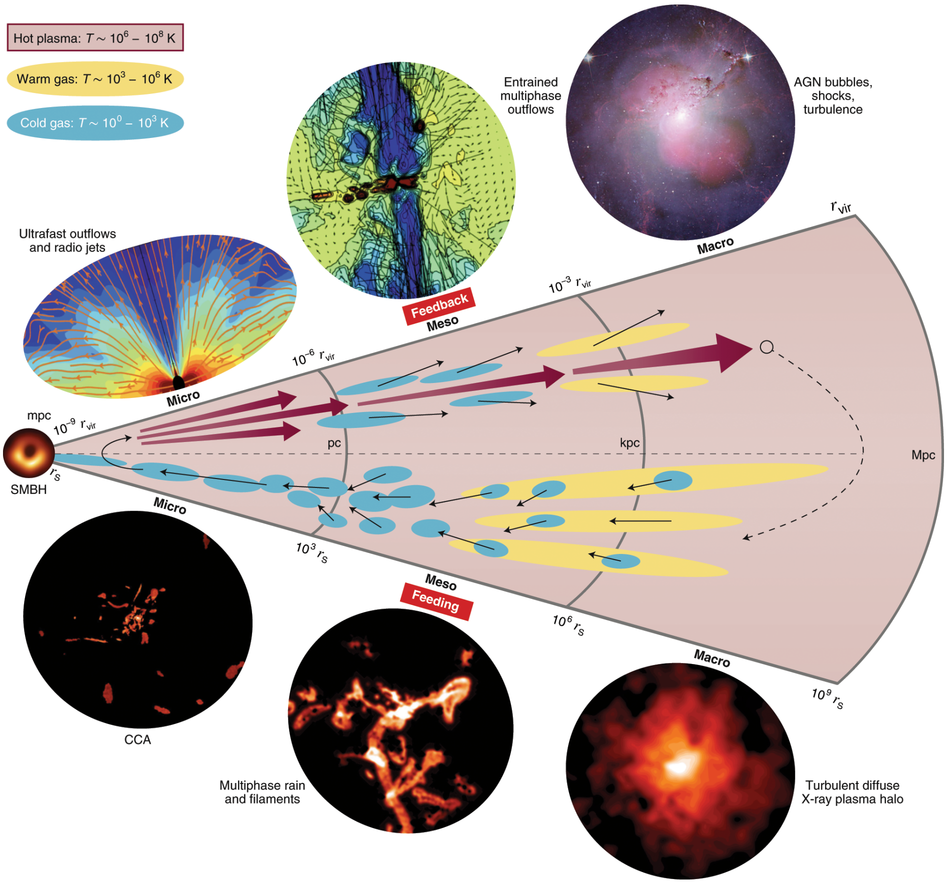

Figure 1.2 The illustration shows the three key scales: micro, meso and macro, which cover a geometric increase of roughly three orders of magnitude each. The macro halo is either a galaxy, group, or cluster and the normalization length is either its virial or Schwarzschild radius (which has been directly imaged by the Event Horizon Telescope 22 – middle left inset). The lower insets show crucial phases of the feeding cycle: The multiphase condensation rain out of the turbulent X-ray plasma halo and consequent chaotic cold accretion phase growing the central SMBH. The upper insets show key phases of the feedback cycle: The generation of hot X-ray ultrafast outflows and collimated relativistic jets, the entrainment of multiphase ambient gas and the final AGN heating deposition via bubbles, shocks, and turbulence (Perseus image credit: ESA/Hubble Media). The multiphase feeding and feedback processes loop for hundreds of cycles during the whole Hubble time (Gaspari et al., 2020).

The halo gas is a very dilute gas with $n_{\mathrm{H}} \lesssim 10^{-2}$. Also it is a multi-phase medium characterized by complex ionization states and rich dynamics with temperatures spanning over the range of two magnitudes $10^4 < T < 10^6$ K. The different phases are divided into sub-sections based on the temperature of each phase: The cool gas with temperatures $< 10^5$ K, the warm gas where $10^5 < T < 10^6$ K and the hot phase with temperatures $> 10^6$ K (Putman et al., 2012). These CGM gas structures coexist and may interact, but the extent to which they interact, the relative fraction of each gas population, and their physical distributions and sizes are still uncertain and not yet fully understood (Werk et al., 2014). Fig. 1.3 illustrates the different phases and their coexistence in the CGM and their various in- and outflow directions.

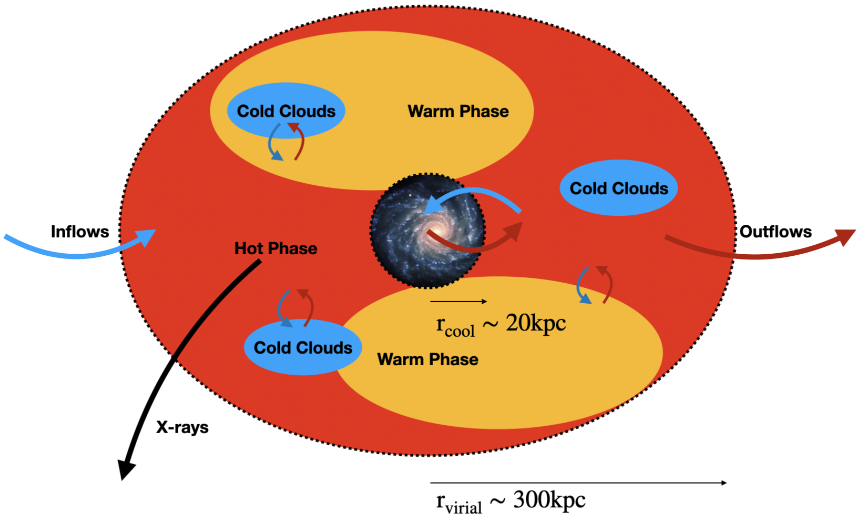

Figure 1.3 This image illustrates the coexistence of the different CGM phases and the various in- and outflow directions. The hot phase in massive galaxies is heated up to sufficient temperatures that it emits X-rays.

The CGM represents the result of galactic feedback processes and the complex interface between the IGM and the ISM of the galaxy itself. Outflows that are mainly driven by feedback from supernovae, but also from AGN, drive large masses of metal-enriched gas into the CGM and also the IGM. In contrast, inflows carry gas through the galaxy halo into the galaxy itself which results in the fueling of star formation. These in- and outflow processes significantly affect the baryon distribution of the galaxy and the mass within the CGM is of similar content as the mass that lies within the galaxy (Peeples et al., 2014; Werk et al., 2014). Subsequently, the gas of the CGM is a combination of new material from the IGM and recycled material from the galaxy itself and regulates the overall galactic gas supply of a galaxy. As the properties of the CGM are directly shaped by the baryon cycle and all out- and inflows of gas are passing through it, it is of specific interest when studying galaxy evolution. Therefore, the CGM plays an important role in uncovering the major problems of galaxy evolution that have been detected in the last decade: On the one hand the problem of missing baryons, referring to the issue that observationally the budget of baryons is still not fully accounted for, and on the other hand the quenching of star formation in galaxies (Hafen et al., 2019; Tumlinson et al., 2017).

To understand the cosmic baryon cycle it is crucial to characterize the relationship and evolution between gas, metal and stars in galaxies. From the beginning of our Universe baryons collapse with dark matter into structures like galaxy clusters and galaxies and stars over time. Today, we find that only $\sim 10\%$ of the baryons collapsed to dense environments leaving $\sim 90\%$ to the various phases of dilute gas. Metals, elements heavier than helium, are produced within stars via nuclear fusion reactions and expelled through supernova explosions (Orr et al., 2021). These explosions are leading to a distribution of metals on larger scales such as the ISM and the CGM (Péroux et al., 2020). Metallicity is an important tracer of the gas origin. If gas has a high metallicity it contains matter that has already undergone cycles of star formation.

The metallicity of a gas is a key property as it is a probe for the enrichment of the gas and provides information on the origin of the gas: On the one hand from metal-enriched out- or inflows or, on the other hand from metal-poor inflows (de Gouveia Dal Pino et al., 2020).

To investigate the thermodynamic history of the CGM and how the CGM gas responds to heating and cooling, pressure and entropy are studied. Gradual heating raises the entropy of gas, but not necessarily its temperature. The same happens with radiative cooling: Radiative cooling lowers the entropy of a gas, but does in turn not necessarily lower its temperature. If a gas cloud passes through a shock front causes a sudden jump in both entropy and temperature, but the temperature of the shocked gas might then decrease adiabatically as buoyancy pushes it upward toward layers of lower pressure (Donahue & Voit, 2022a). However, in astronomy gas is more commonly described in terms of temperature T and density n (and not pressure P and entropy K, as these are more directly measured with observations). A useful tool to describe gas in terms of P and K in an illustrative way are phase diagrams with P and K being the axes. Fig. 1.4 shows an example of a phase diagram where the cooling time structure in the CGM of four different galaxies is displayed. Notably the dependence of cooling time and specific entropy on radius in each of these galactic atmospheres is very similar, even though pressure differs by three orders of magnitude, density differs by two orders of magnitude, and temperature differs by an order of magnitude.

1.3.1 CGM in Simulations

As the CGM is specifically hard to observe directly, simulations play an important role in investigating the CGM. The first simulations of the CGM have been implemented in the early 2000s. Early simulations in this field were often simplified and based on hydrodynamic models that did not include all the relevant physics and interactions. The first simulations of galaxy formation did not implement feedback processes and predicted overly massive and dense galaxies. With the advancement of computational capabilities, cosmological simulations started to include more realistic treatments of gas physics, gravity, and the expansion of the universe in the last decade. These simulations aimed to study the formation and evolution of galaxies in a cosmological context, which naturally included the CGM. Prominent simulations such as the Illustris project (Vogelsberger et al., 2014) and EAGLE (Oppenheimer et al., 2016) incorporated a wide range of physical processes such as gravity, hydrodynamics, cooling, star formation, and feedback from supernovae and AGN. These simulations provided insights into the CGM's properties and its role in regulating star formation in galaxies.

The CGM has been extensively studied in both cosmological hydrodynamic simulations with statistical samples of galaxies and cosmological zoom-in simulations of individual halos. By analyzing simulations of the large cosmological box (Hafen et al., 2019; Nelson et al., 2020; Oppenheimer et al., 2018) it is possible to have a statistic over many halos of different masses. On the other hand, zoom-in simulations allow to reach a greater level of detail on a single halo, with the inclusion of more detailed physics (Hummels et al., 2013; Peeples et al., 2019; Suresh et al., 2019). Some simulations manage to find a compromise between the improved resolution and the increase of computational cost, adopting refinement criteria that explicitly

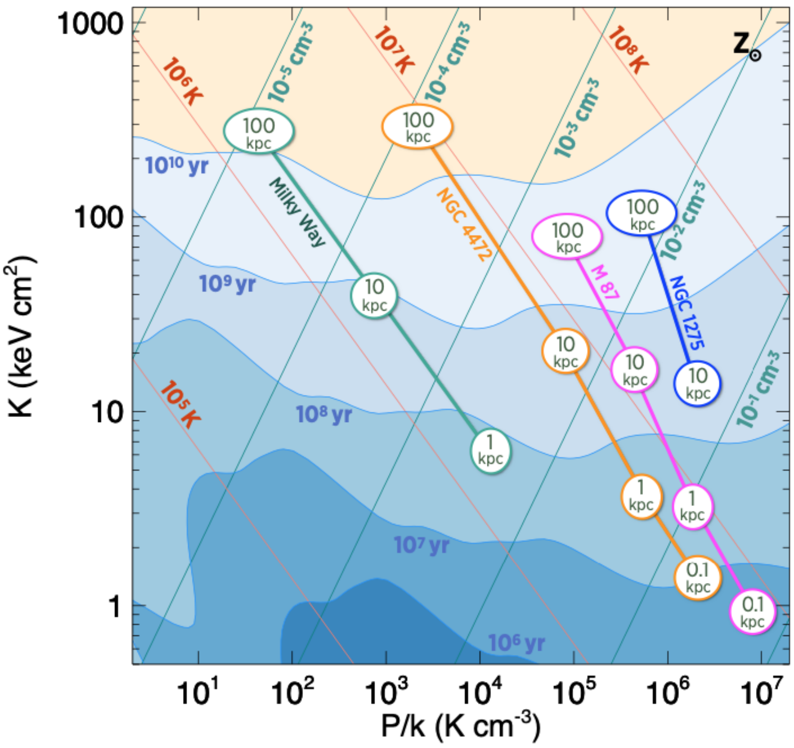

Figure 1.4 This figure shows the consistency of cooling time structures in the CGM of massive galaxies where four different galaxies are represented. The horizontal axis shows P/k in units of K cm $^{-3}$ and the vertical axis shows K in units of keV cm^2. The diagonal lines rising from left to right are lines on constant density and the one declining from left to right are lines of constant temperature. We see that all galaxies have the same cooling times of $t_{\rm cool} \sim 10^9$ yr at $\sim$ 10 kpc and $t_{\rm cool} \sim 10^{10}$ yr at $\sim$ 100 kpc, although the gas pressures of the galaxies differ by more than three orders of magnitude. Taken from (Donahue & Voit, 2022a).

target the CGM, as additional spatial refinement up to the virial radius (Hummels et al., 2019; van de Voort et al., 2019).
Fig. 1.5 shows the results of a simulation of gas properties around three star forming galaxies and one quiescent galaxy of different stellar masses with 10^9 $M_\odot < M_{*,\rm gal} < 10^{11}$ $M_\odot$ at redshift $z = 0.2$. Specifically the total column density in the three different temperature phases and the metallicity are displayed. We see that the CGM comes with multiple phases at all presented galaxy masses, where cool clumpy gas is embedded in a warmer surrounding medium. The total mass of both cool and hot gas and also the metallicity increases with galaxy mass. The quiescent galaxy hosts even more hot gas than the star-forming galaxies, which is due to a more massive halo and a larger central AGN (Suresh et al., 2017; Vogelsberger et al., 2014).

The CGM is highly sensitive to feedback processes as the CGM hosts many interactions: Feedback processes usually eject a significant fraction of gas out of the galaxy into the CGM. This gas then heats the CGM by interacting with the cold gas accreted by cosmic filaments.

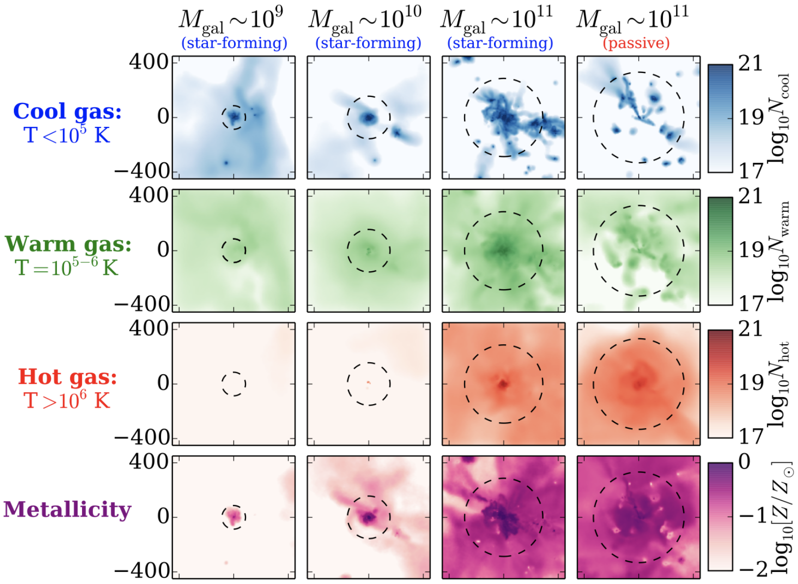

Figure 1.5 This image displays the distribution of the gas of the different temperature phases and the metallicity around four representative galaxies at $z = 0.2$ in boxes of a side length of 400 kpc how it was simulated in (Suresh et al., 2017). The mass of gas of all phases increases with galaxy mass with the quiescent galaxy showing more mass in the hot phase than its star-forming counterpart. The dashed lines indicate the virial radius.

The CGM is a very complex medium to simulate, possibly showing a high sensitivity to the ejection of gas from galaxies, as well as being the site of interaction of different thermal phases. This complexity makes it a suitable medium to produce new constraints to the various subgrid models for galaxy formation. Using subgrid model cosmological simulations and semi-analytic models have demonstrated that the inclusion of star formation and AGN feedback and the resulting galactic winds are essential to match observed statistical properties of galaxies (Somerville & Davé, 2015a). Therefore, nowadays it is well established that efficient feedback is needed to supress star formation and produce realistic disc galaxies fulfilling several observed relations (Aumer et al., 2013; Scannapieco et al., 2012; Vogelsberger et al., 2013). Furthermore, the modeling of feedback including chemical evolution has allowed simulations to describe the enrichment of baryons as galaxies form and evolve in a cosmological context (Gibson et al., 2013; Tissera et al., 2012).

One important feedback process that has to be taken into account in CGM simulations is supernovae feedback. As supernovae produce large energies and the majority of metals and drive galactic outflows that transport energy, as well as mass and metals into the CGM and even further they are of large interest when studying the matter cycles in Galaxies (Fielding et al., 2018). Small box simulations with smaller scales in the kpc-regime and with pc resolution have examined how SNe drive galactic outflows from the ISM. These simulations quantified outflow rates of mass, energy and metals and show that hot outflows have a larger volume fraction in contrast to the cooler phases. They are also faster, whereas the cooler phases occupy a smaller volume and are slower (Fielding et al., 2018; Hu, 2019; Kim & Ostriker, 2018; Li & Bryan, 2020).

AGN feedback is also important to include into CGM simulations. One significant initial inconsistency between observations and cosmological hydrodynamic simulations of the CGM was a consistent underestimation of observed O VI by a factor of 3 to 5. This problem has been successfully addressed in recent times through the integration of supplementary AGN feedback mechanisms (Oppenheimer et al., 2018). Simulations with very high-resolution numerical calculations have become possible with increasing computing power. These simulations have reproduced the observed fraction of hydrogen and metals around different types of galaxies (Butsky et al., 2020; Fielding et al., 2020; Nelson et al., 2020; Oppenheimer et al., 2016). Idealized hydrodynamics simulations have revealed the co-existence of cool ($T \sim 10^4 - 10^{4.5}$ K) and warm ($T > 10^6$ K) gas within the virial radius of the dark matter halo (Lochhaas et al., 2020). The predictions inferred from these simulations agree reasonably well with the observations (Nelson et al., 2021; Oppenheimer et al., 2016).

An unresolved issue in galaxy formation is the so-called *missing baryon problem*: Calculations inferred from the Big Bang nucleosynthesis cosmology (BBN) are leading to a value of a baryon density of $\rho_\mathrm{b} = (4.19 + / - 0.08) \times 10^{-28}$ kg m^{-3} today (or, expressed in fraction of ρ_crit and h: $\Omega_\mathrm{b} h^2 = 0.02190$ to 0.02271) (Pitrou et al., 2018). Estimates on the baryon density using cosmological parameters which are independent from the former lead to a value of $\Omega_\mathrm{b}^2 = 0.0224 + / - 0.0001$ (PlanckCollaboration et al., 2018). Cosmological simulations of large-scale structure formations predict that the distribution of collapsed baryons vs. the distributed matter is inefficient and that only $10 - 20\%$ of all baryons reside within collapsed objects such as galaxies and clusters. 80% are distributed over a wide range of phases and temperatures in form of unbound plasma between galaxies and clusters (Smith et al., 2011; Tepper-García et al., 2011).
This prediction from simulations of the baryon content of the Universe has been an open question in the last decade as it is in contrast to observations which are lacking a significant amount of baryons when summing up all baryons existing in plasma, gas, dust, stars and black holes. Observations of the Lyα forest of absorption lines suggest that the warm-hot intergalactic medium (WHIM) contains $\sim 30\%$ of the low-redshift baryons. Another $\sim 30 - 40\%$ is predicted to exist within shock-heated gas of the unbound WHIM, which sums up to $\sim 60 - 70\%$ of the baryon budget. Another $\sim 5\%$ is predicted to reside inside the CGM and $\sim 4\%$ and $\sim 7\%$ in galaxies and cluster respectively. Overall, up to $\approx 30\%$ of baryons are therefore missing (Danforth & Shull, 2008; Shull et al., 2012; Smith et al., 2011).

Besides the shortage of baryons on universal scales, baryons are also missing in galaxy-scale halos, known as the galaxy halo missing baryon problem: Compared to the cosmological Ω_b/Ω_m ratio, galaxies and their halos come up significantly short on baryons, missing $\sim 60\%$ of baryons (Sokołowska et al., 2016; Werk et al., 2014). Models of galaxy formation predict that the center of a galaxy only contains a fraction of the baryons that are available, as galaxies are inefficient and only convert a small fraction of the contained gas into stars. With the help of simulations it has become apparent that a viable amount of baryons exist within the different phases of the CGM. Fig. 1.6 shows a chart where the fraction of baryon budget of different phases of a galaxy are displayed and how the proportions were analyzed (Werk et al., 2014).

In general, simulations of the CGM are crucial to understand the complex processes that take place in the different phases of the CGM. As the CGM is challenging to observe directly, simulations allow us to virtually explore these environments, providing insights into the distribution, composition, and dynamics of the CGM. Key findings from simulations are:

1. Simulations confirm the multi-phase nature of the CGM, showing the coexistence of various temperature and density phases.

2. Feedback processes such as star formation and AGN feedback are necessary to produce realistic galaxies fulfilling the observed relations.

3. Recent simulations have explored the enrichment of the CGM by metals, particularly oxygen. While some simulations initially underestimated OVI content, advanced models incorporating magnetohydrodynamics, additional AGN feedback, and cosmic rays have succeeded in reconciling simulated OVI observations with real data.

4. Simulations have addressed the missing baryon problem by analyzing the distribution of baryons within galaxies, clusters, and the warm-hot intergalactic medium. They reveal discrepancies between theoretical predictions and observations, suggesting that a significant fraction of baryons exists in unbound plasma and diffuse phases.

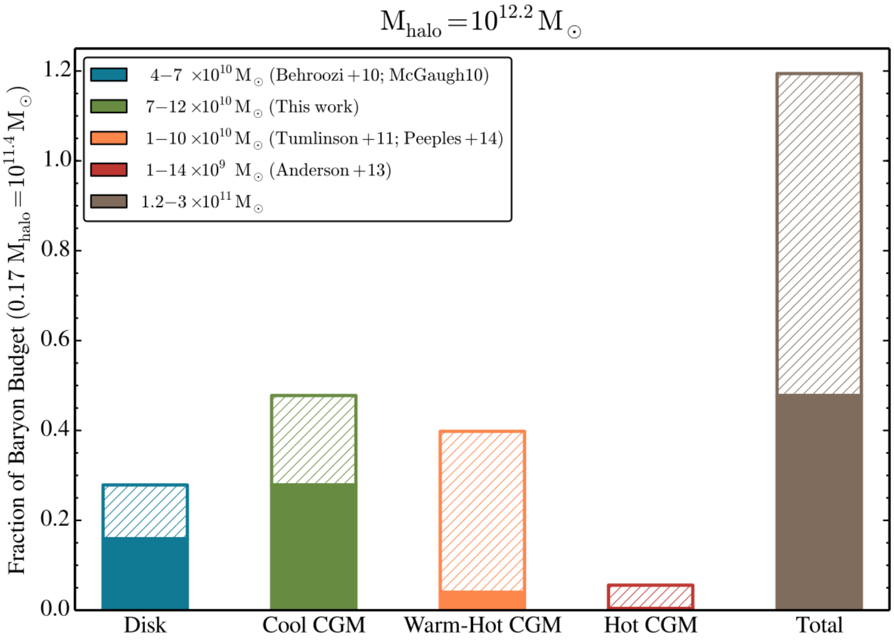

Figure 1.6 This bar chart shows the most massive baryonic components of a galaxy at L ≈ L* and how there were computed by various authors. The filled bars are the lower limits with the dashed area potential additions that are allowed by the data. Taken from (Werk et al., 2014) including the works from (Anderson et al., 2013; Behroozi et al., 2010; McGaugh et al., 2010; Peeples et al., 2014; Tumlinson et al., 2017).

1.3.2 Observations

Although the CGM plays such an important role in galaxy formation it is exceedingly hard to study observationally. Direct detection of the CGM is difficult due to the low density of the gas ($n_{\mathrm{H}} \lesssim 10^{-2}$), which is spread over great volumes. Observations that investigate emission-lines that are directly emitted by the CGM are limited to a very small sample of nearby galaxies and the Milky Way itself as the emission measure scales as n^2. The different phases of the CGM can not be detected by a single observation method as different phases exhibit different signatures that have to be detected individually. The cold gas which consists mostly of neutral hydrogen at $T < 10^4$ K and in form of high-velocity clouds can be traced via the 21-cm line (Putman et al., 2012). The warm gas at temperatures of $10^4 - 10^5$ K which resides in the galactic halo is measurable via deep Hα emission line observations and low and intermediate ion absorption lines such as Si II, Si III, C II, C III, O I using background quasars. Therefore, to study the warm phase absorption line studies have been the preferred technique. The hot $\sim 10^6$ K halo gas that traces shock-heated IGM and feedback mechanisms are also examined via absorption lines (O VII and O VIII) but also through X-ray observations (Anderson et al., 2013; Gupta et al., 2012). The hot gas with $T > 10^6$ K emits soft X-ray emission via thermal bremsstrahlung that can be directly observed.
Observations of the CGM are also crucial to solve the problem of the missing baryons as two most likely possibilities have been described to solve it: On the one hand they are supposed to exist as diffuse gas inside the circumgalactic medium and on the other hand they are suspected to remain in the so-called Warm Hot Intergalacic Medium (WHIM), also as diffuse emission. The various observation techniques to observe the CGM are described below.

1.3.3 Transverse Absorption-Line Observations

One powerful tool that is used to study the CGM are the so-called transverse absorption-line studies, where the CGM is analyzed via absorption lines using light from background quasars. A narrow path through the CGM of a galaxy is probed as the light from a background source propagates from its origin to Earth. The light interacts with the atoms and ions in the CGM, leaving an imprint of its presence on the observed spectrum, depending on the chemical abundance of the intervening gas. The quasar can then be fitted with a model spectrum and any remaining absorption will be a result of the intervening gas. Measuring the absorption strength of these lines enables to determine the relative abundance of various chemical elements within and thus the metallicity of the gas (DeFelippis et al., 2021; Mintz et al., 2020). Fig. 1.7 illustrates the basic setup of a transverse absorption line observation.

Detecting and characterizing the CGM in absorption against bright background quasars comes with some advantages over other methods: First, it provides access to a wide range of densities in contrast to emission-line measures that scale as density squared. Second, these studies are sensitive to very low column densities of $n \approx 10^{12}$ cm^{-2}. A third advantage is their invariance to detection limits like the luminosity of the host or redshift. However, these observations also have some limitations as it is usually only possible to obtain projected and pencil-beam measurements of gas surface density. Also, the limitation of present quasars usually restricts

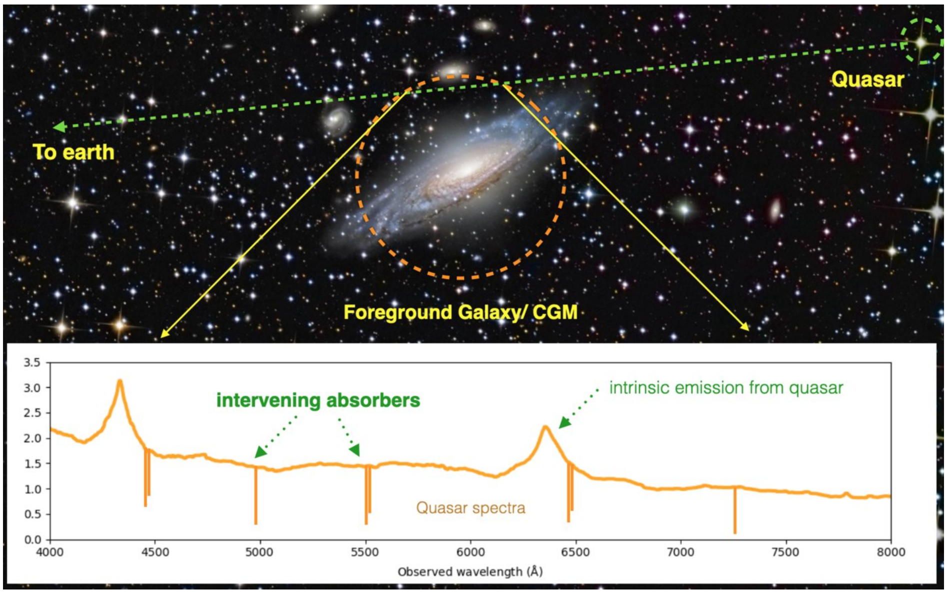

Figure 1.7 Basic setup of an absorber galaxy cross-correlation study, where the CGM is observed in absorption against a bright background quasar. The light from the backgorund quasar passes through the CGM of a foreground galaxy. The intrinsic emission from the quasar shows absorption lines that depend on the chemical abundance of the CGM gas (Anand et al., 2021).

these observations to one sight-line per galaxy and an important note is that CGM maps made from absorption-line measurements are only a statistical sampling of gas aggregated from many galaxies (Tumlinson et al., 2017). Metal absorbers detected at lower redshifts than the redshift of the background source provide direct observational constraints on gas in- and out flow due to various processes at different epochs. The warm gas at temperatures of $10^4 - 10^5$ K which resides in the galactic halo is measurable via deep Hα emission line observations and low and intermediate ion absorption lines such as Si II, Si III, C II, C III and O I (Piacitelli et al., 2022; Sandrinelli et al., 2020). The overall CGM metallicity can be calculated based on absorption studies using a likelihood function using the measured column densities and a grid of ionization properties (Pointon et al., 2019). Low ionization metal absorption due to O I has been identified as an important probe of metallicity (Keating et al., 2014).

Most absorption-line studies have been done in the UV and optical regime. For low-z targets, absorption studies have been pursued with the Cosmic Origins Spectrograph (COS) on the Hubble Space Telescope (HST) in the last decade (Stocke et al., 2014; Tumlinson et al., 2011; Werk et al., 2016). COS was specifically used to study the column density of HI (N_{HI}), also known as the Lyman limit systems (LLSs) to determine the absorption strength of absorbers. LLSs are usually quantitatively defined as system with HI column density $N_{\mathrm{HI}} > 10^{17.2}\ \mathrm{cm}^{-2}$ and they are useful tracers of in- and outflows as these are dense enough to be associated closely with galaxy halos but not dense enough to exist only in galactic disks, which are better traced by Lyα absorbers. The observation with COS shows that the gas in the studied absorbers is largely ionized. In addition, the metal ion column densities are related to those of HI yielding that N_{MgII} is strongly correlated with N_{HI} (Lehner et al., 2018).

To study the baryon content of the different gas phases and to investigate the problem of missing baryons, absorption line studies have also been carried out in X-ray spectra. These analysis lead to the assumption that the missing baryons are contained in the hot phase of the WHIM (Nicastro et al., 2018). Still, there are large uncertainties at this point about the baryon content of the different gas phases. Fig. 1.8 illustrates the outcome of the three introduced works.

In general, transverse absorption-line studies are a powerful technique for investigating the properties and interactions of the circumgalactic medium. They can reveal the effects of galactic feedback processes, such as supernovae and energetic outflows, on the CGM. These processes can significantly impact the physical and chemical properties of the CGM gas.

1.3.4 Down-the-Barrel Observations

Another method to study the CGM are so-called "down-the-barrel" spectroscopic surveys. In contrast to quasar absorption-line studies, down-the-barrel absorption lines involve looking directly at the CGM by targeting the gas associated with a specific foreground galaxy to measure the column density and velocity of outflowing gas. In particular, the outflows of star forming galaxies can be studied with this method in nearby galaxies of $z < 1$ as these measurements are direct tracers of outflows from galactic centers. The most used absorption lines lie within the optical and UV range, e.g. Ca II, Na I, Mg II, and Fe II (Heckman et al., 2015). These studies are also useful when there is no sufficient background source such as a quasar. A disadvantage is that any detected absorption could be possibly at any point along the line of sight.

However, this technique also comes with advantages: The gas that absorbs the stellar light from a galaxy is known to be located between the galaxy and the observer. This leads to the fact that redshifted absorption can be clearly associated with gas with a radial velocity component in the direction of the galaxy. In galaxy pair experiments, an outflowing absorber located behind the foreground galaxy would also appear redshifted. This introduces a generic ambiguity in the interpretation of absorption lines transverse to foreground galaxies.

Detailed analysis using down-the-barrel spectra reported detection of infalling gas in a fraction of $3 - 6\%$ galaxies with redshifts between $0.4 < z < 1.4$. As these detection used low-ionization metal absorption lines they trace relatively metal-rich gas, such as infalling dwarf galaxies on their way to merging or recycling wind gas, rather than gas accreting from the IGM for the first time, which would be expected to be metal-poor (Martin et al., 2012; Rubin et al., 2014). Other down-the-barrel studies investigated the warm outflowing phase of the CGM and generally the metal-loading factor in local star-forming galaxies using ultraviolet absorption lines and stellar continua. Results from these studies have shown that outflow metallicities are indeed larger than the observed ISM metallicities resulting in the fact that galactic outflows fundamentally shape the observed mass-metallicity relationship (Chisholm et al., 2018).

In general, down-the-barrel observations can reveal the effects of galactic feedback mechanisms such as outflows from starbursts or AGN on the CGM, as well as the accretion of fresh gas onto the galaxy. However, challenges include distinguishing between absorption features due to the CGM and those caused by intervening gas along the line of sight, accurately modeling

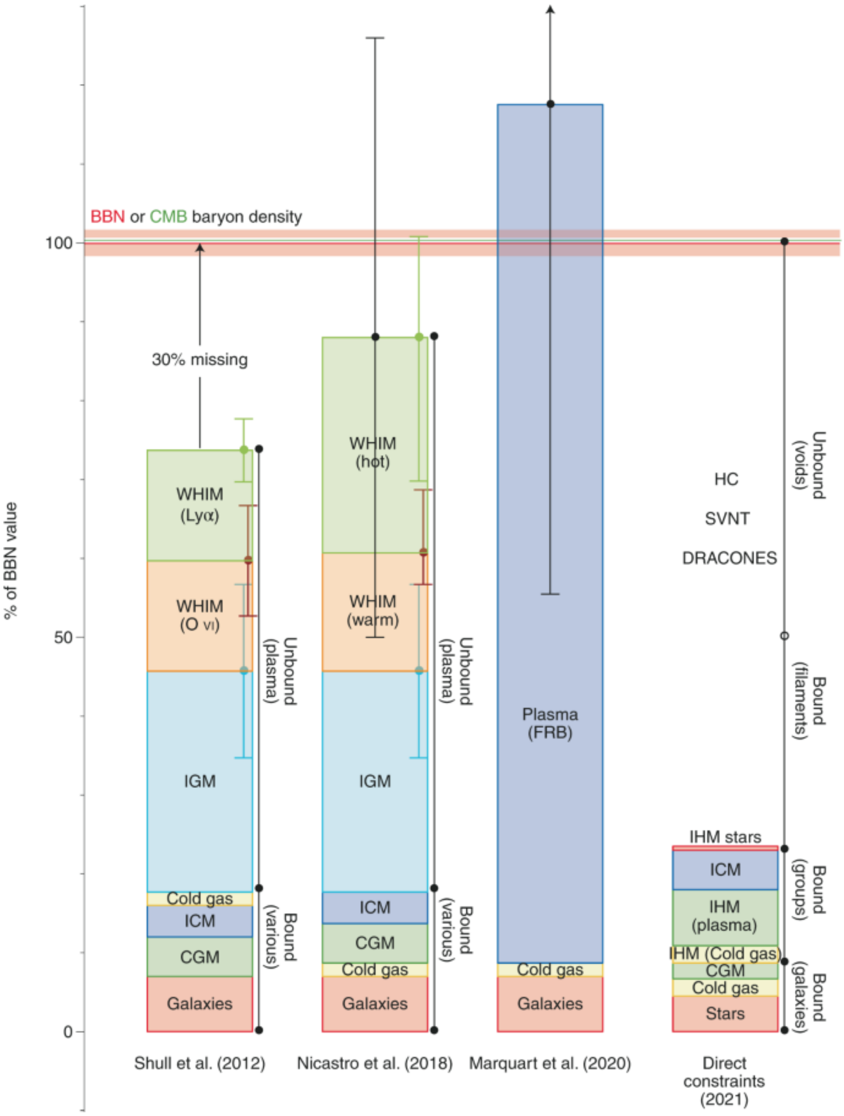

Figure 1.8 This chart shows the recent estimates of the local baryon census taken from(Driver, 2021).(Nicastro et al., 2018) and (Macquart et al., 2020) seemed to have solved the problem of missing baryons stated in (Shull et al., 2012). Still, there are large uncertainties resulting from these analysis with the error bar of (Macquart et al., 2020) even exceeding the plot. The bar on the right sums up the baryon content constrained from direct observations.

the complex physical conditions of the gas, and obtaining high-quality spectra with sufficient resolution.

1.3.5 X-ray Observations

The hot-phase ($T > 10^6$ K) gas of the CGM is traceable through its X-ray emission and of specific interest in CGM studies as it is proposed that this phase contains a significant fraction of up to 50% of the missing baryons in galaxy-scale environments around massive galaxies

(Anderson & Bregman, 2010).
However, it remains a problem that the expected X-ray luminosity is very low and hard to detect for current X-ray missions. The atmospheres around isolated galaxies are extremely difficult to image as such galaxies have very low X-ray surface brightness, and their low-energy X-ray photons are absorbed by cooler gas in our own Galaxy. Also, the X-ray emission of clusters or groups has to be taken into account when studying objects that exist within cluster/group environments. Direct observation of the hot and X-ray emitting halos have been observed around individual or small samples of galaxies in the past. This has been generally achieved for early-type massive and isolated galaxies (Anderson et al., 2013, 2016; Bregman et al., 2018; Li et al., 2017).

At the lowest luminosity levels, X-ray emitting galactic atmospheres can be detected only through stacking of many such observations of similar galaxies. Stacking is a useful approach to make diffuse emission visible that can not be detected from single targets. Therefore, several images (from a few up to millions) of sources of interest are stacked to increase the signal to make a detection possible. Stacking therefore involves combining many short exposures of many similar targets. By stacking large datasets, the noise decreases and features with weak signal can be unveiled as stacking amplifies the signal-to-noise by $\sqrt{N}$ (where N is the number of objects stacked), assuming the inherent systematic uncertainties in the underlying data are small (Davies et al., 2020).
Stacking X-ray images of 250.000 galaxies from the ROSAT survey by (Anderson et al., 2015) have shown that X-ray luminosities of the hot CGM have positive scaling relations with the galaxy's start formation rate and its mass and that star forming regions are spatially correlated with the X-ray emission.
Stacking techniques do not necessarily need thousands of targets. Also studies with only a few stacked targets exist. Stacking the X-ray observations of only six massive isolated nearby spirals using data from the CGM-MASS program by the XMM-Newton telescope has revealed that the X-ray emitting phase of the CGM only accounts for only $\sim 8\%$ of the total expected baryon budget of a galaxy (Li et al., 2018). Summing up the total baryons within the virial radius (hot gas and stellar) lead to a value of $\sim 27\%$ leaving $\sim 73\%$ still missing. Another result of this work was the prediction of a constant slope of the X-ray intensity profile. The authors proposed two possible explanations to this finding which was not suggested by simulations: On the one hand a feedback mechanism of AGN or supernovae could lead to flattening or, on the other hand a density of metallicity change as X-ray emission is proportional to both characteristics.
Recently, eROSITA observations were used to stack more than 16.000 galaxies to examine the X-ray luminosity profiles in the $0.5 - 2$ keV rest frame energy band as a function of their stellar mass and specific star formation rate Comparat et al. (2022). This stacking approach resulted in extended X-ray profiles for a quiescent galaxy sample and a faint extended emission around star-forming galaxies. However, these results should be handled with care as projection effects caused by the fact that quiescent galaxies tend to live in dense and hot environments may have affected the results. Also, this detection is not in agreement with previous work and simulations where extended X-ray profiles are usually expected and found around star-forming disc galaxies. Disc galaxies with active star formation are expected to have more prominent and complex CGMs due to their ongoing gas inflows, outflows, and interactions with the interstellar and intergalactic medium than quiescent elliptical galaxies.

1.3.6 Magnetic Fields

Magnetic fields exist throughout the universe, from galaxies and galaxy clusters to stars and even on smaller scales within planetary bodies, and also in the CGM. Magnetic fields can influence a galaxies dynamic and evolution by driving galactic-scale outflows, the expulsion of gas from galaxies and influencing their overall gas content and star formation rates. However, the evolution of magnetic fields in galaxies and the surrounding CGM over cosmic time is observationally still largely unconstrained and it is not yet fully understood how the CGM gets magnetized in the first place. Two possible scenarios are described: On the one hand the magnetic fields could be generated by small-scale dynamo effects (Pakmor et al., 2017, 2020) or, on the other hand the magnetic fields could be transported from the galaxies themselves via galactic winds and outflows (Péroux et al., 2020).

Dynamos are processes that generate and amplify magnetic fields through the motion of conducting fluids, such as ionized gas. To start a dynamo process, a weak initial seed magnetic field needs to be present. This seed field could originate from various sources, such as cosmological primordial fields or magnetic fields from external sources like the intergalactic medium. Motions and turbulence in the galaxies gas create electric currents in the ionized gas. As the ionized gas flows and rotates within the galaxy, it interacts with the existing magnetic field. According to electromagnetic induction, the motion of charged particles within the gas generates electric currents. These currents, in turn, lead to the amplification of the magnetic field, enhancing its strength. Turbulent motions in the gas cause stretching and folding of the magnetic field lines. This process increases the complexity and strength of the magnetic field, as the lines become twisted and intertwined. As the magnetic field becomes stronger, it starts to influence the motion of the ionized gas through the Lorentz force. This feedback can lead to changes in the fluid motion and turbulence, affecting the dynamics of the gas and further enhancing the amplification process. Through this process, the initially weak and disordered seed field can evolve into a more organized and coherent magnetic field structure that follows the overall motion and structure of the galaxy. Galactic dynamos are complex and nonlinear processes that depend on a variety of factors, including the properties of the interstellar medium, the rate of star formation, the presence of spiral arms, and the overall structure of the galaxy (Beattie et al., 2023).
Within the CGM, motions of ionized gas and turbulence can help to sustain and amplify existing magnetic fields. Small-scale dynamos, driven by turbulent motions, can contribute to the growth of magnetic fields in regions of the CGM with significant fluid motions. If the small-scale dynamo effect is considered as the origin of the magnetized CGM we expect turbulent magnetic fields showing no ordered fields with a common direction on the size of the CGM extent (Fletcher et al., 2011).

If we consider galactic winds and feedback to be the origin of the magnetized CGM strong azimuthal dependence of the magnetic fields is expected, as the outflows are usually found near the minor axis of galactic discs, as these outflows preferably propagate along the minor axis due to the conservation of angular momentum. This is valid for both, stellar and AGN driven feedback (Pillepich et al., 2021; Ramesh et al., 2023; Thomas et al., 2022).
Magnetic fields in nearby (distance < 50 Mpc) star-forming disc galaxies have been studied

in detail, with most studies indicating the existence of a galactic dynamo (Beck, 2015; Beck et al., 1996). For high redshift galaxies above redshift 0.1 the database is much smaller with only a few studies existing (Bernet et al., 2008; Farnes et al., 2014; Kim et al., 2016; Lan & Prochaska, 2020; Mao et al., 2017; Oren & Wolfe, 1995). Measuring the magnetic fields directly via synchrotron emission is limited to small distances to a galaxies center of approximately 15 kpc due to spectral ageing (Miskolczi et al., 2019). Therefore, the direct mapping of the magnetic field structure and strength in high-z galaxies, as it has been studied in nearby galaxies, will be a challenging task for next-generation radio telescopes like the Square Kilometre Array (SKA).
To examine the magnetic fields around galaxies up to larger distances Faraday rotation can be studied instead. Details on this method are described in Section 1.3.7.

1.3.7 Faraday Rotation Measures

Faraday rotation is a process by which the position angle of background linearly polarized light is rotated when passing through an ionized and magnetized medium. The intervening medium causes a difference in the phase velocity between the left-handed and right-handed circular polarization components of the linearly polarized synchrotron radiation emitted by the background radio source. The Faraday rotation can therefore be described by a rotation of the intrinsic polarization angle

$$\psi(\lambda^2) = \psi_0 + \phi\lambda^2. \tag{1.1}$$

The polarization angle ψ depends on the observed wavelength λ through the Faraday depth ϕ (Burn, 1966):

$$\phi = a_0 \int_0^{z_\mathrm{s}} B_{\|}(z) n_\mathrm{e}(z) \left(\frac{\mathrm{d}l}{\mathrm{d}z}\right) \mathrm{d}z. \tag{1.2}$$

Here, a_0 depends on fundamental constants and equals $8.1 \cdot 10^5$, the free electron number density n_e, the magnetic field component along the line of sight $B_{\|}$ and the comoving path increment per unit redshift $\mathrm{d}l/\mathrm{d}z$. The amount of Faraday depth measured by radio observations along a given line of sight is the sum of all contributions from the Milky Way, the emitting radio source, and any other source and large-scale structure in between hosting a magnetized plasma. The Faraday rotation of emitted light of an astrophysical source due to a magneto-ionized gas is illustrated in Fig. 1.9.
When the rotation is completely due to a foreground screen, the Faraday depth has the same value as the rotation measure (RM) $\mathrm{RM} = \frac{\partial\psi}{\partial\lambda^2}$ (Vacca et al., 2016). Therefore, the Faraday rotation measure (RM) modifies the polarization angle via

$$\psi(\lambda) = \psi_0 + \mathrm{RM}\lambda^2 \tag{1.3}$$

(Heald, 2009). Faraday rotation measures is one of the very few methods to probe extragalactic magnetic fields. The RM of the polarized light of background quasars passing through the magnetized CGM can be used as tracers for the strength and extent of magnetic fields around galaxies out to large distances of approximately 500 kpc from its center. The RM is assumed to be positive when the line-of-sight average component of the magnetic field points toward the observer, otherwise it is negative for a field with an average component pointing away from

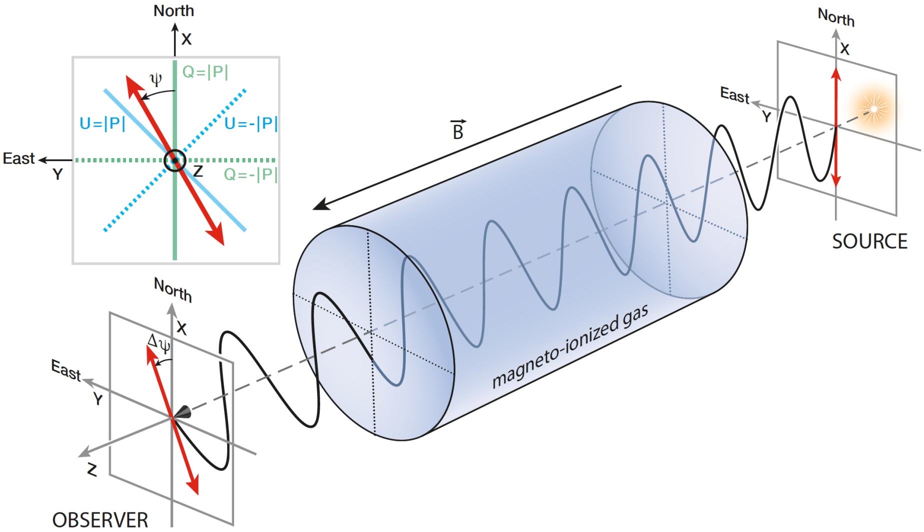

Figure 1.9 This illustration shows qualitatively how the electric field vector of a linearly polarized radio wave oscillates along the propagation direction, between the source and the observer. It also demonstrates how the polarization orientation (red double-headed arrow) undergoes Faraday rotation as the wave passes through a magneto-ionized region. Faraday rotation is right-handed towards the magnetic field $B_{\|}$. When the direction of $B_{\|}$ points towards the observer, Faraday rotation is counterclockwise in the plane of the sky which corresponds to a positive angle ψ_0 and vice versa. Taken from Ferrière et al. (2021).

the observer (Vacca et al., 2016). The RM is given by the change in observed polarization angle $\Delta\chi_0$ over a change in the observed wavelength square $\Delta\lambda_0^2$. For a polarized radio source at cosmological redshift z it is defined as

$$\mathrm{RM}(z) = \frac{\Delta\psi_0}{\Delta\lambda_0^2} = 8.1 \cdot 10^5 \int_z^0 \frac{n_e(z) B_{\|}(z)}{(1+z)^2} \frac{\mathrm{d}l}{\mathrm{d}z} \mathrm{d}z. \tag{1.4}$$

RM is in units of rad m^{-2}, the free electron number density n_e is in cm^{-3}, the magnetic field component along the line of sight $B_{\|}$ is in Gauss and the comoving path increment per unit redshift $\mathrm{d}l/\mathrm{d}z$ is in parsec. This equation assumes a uniform RM screen across the source and a spatial separation of the linearly polarized source and the Faraday rotating plasma (Bernet et al., 2012).

In general, to obtain RMs from astrophysical observations, several steps are typically followed:

1. Observe a source of polarized radio waves: To measure the rotation of the polarization angle, it is necessary to observe the same source of polarized radio waves at different wavelengths. This is typically done by using radio telescopes that are capable of observing over a wide range of frequencies.

2. Measure the relative change of polarization angle at each wavelength.

3. Determine the rotation measure: Once the change of polarization angle has been measured at multiple wavelengths, the rotation measure can be calculated using eq. 1.4.

4. Map the Faraday depth (eq. 1.2): The map of Faraday depth is obtained by fitting the rotation measure for each point of the source.
5. Interpret the results.

1.4 Galaxy Clusters

Zooming out another scale and leaving galaxies and their surroundings behind, we reach the largest building blocks in our Universe: Galaxy clusters. Matter and galaxies in general are not uniformly distributed in the Universe, rather they are concentrated in large filaments and voids of galaxies which are tangled together forming a web-like structure, the cosmic web. Within the cosmic web accumulations of galaxies, known as galaxy clusters, exist which are supposed to be the largest gravitationally bound structures that can be found in the Universe. Galaxy clusters can contain hundreds to thousands of galaxies reaching final virial masses of $10^{14} - 10^{15}$ $\mathrm{M}_\odot$ and sizes of the order of a few Mpc. Studying large-scale structures like galaxy clusters provides hints to understanding the initial conditions and fluctuations of the early Universe and the way it has evolved over time, as galaxy clusters are the result of the gravitational collapse of overdense regions that are seeded by processes in the early Universe, followed by a sequence of mergers and accretion of surrounding material. Therefore, clusters represent the latest stage of the structure formation, presently assembling through mergers of smaller groups of galaxies and gas accretion (Bond et al., 1996; Kravtsov & Borgani, 2012).
Clusters of galaxies consist of three different types of matter: Non-collisional dark matter (80%), hot diffuse baryons of the intracluster medium (ICM) (17%) and cold baryons formed to stars (3%) Lin et al. (2003). Dark matter dominates the mass of a cluster like it does for single galaxies (Moster et al., 2010). Its existence is deduced from the dynamics of galaxies, from the gravitational lens effect and from the properties of the intracluster gas. The baryonic composition of clusters is dominated by hot gas that is in quasi-hydrostatic equilibrium within the dark matter dominated gravitational potential of the cluster.

The presence of the ICM can be explained by hierarchical structure formation. Warm baryons swept towards the cluster together with collapsing dark matter and then heated to temperatures of $10^7 - 10^8$ K by accretion shocks and adiabatic compression McNamara & Nulsen (2012). Therefore, the ICM shows emission in the form of thermal bremsstrahlung and it is also a powerful source of X-ray radiation Tozzi (2007). The luminosity range in the X-ray band reaches about $L_\mathrm{X} \sim 10^{43} - 10^{45}$ erg s^{-1} and emissivity $J_\mathrm{X}(T) \propto n^2$ with n being the ICM density. The surface brightness distribution of the X-ray emission illustrates a clusters' morphology since it indicates the location of bulk baryonic matter within the cluster. With X-ray observations it is also possible to identify potential cluster mergers which usually show a disturbed distribution of thermal gas.
The main components of the ICM plasma are ionized hydrogen and helium which are mixed with heavier elements at $\approx 1/3$ of the solar metal abundance Arnaud et al. (1992). As the ICM is visible through spatially extended thermal X-ray emission it has been studied both for evaluating its physical properties and also as a tracer of the large-scale structure of the Universe. Therefore, galaxy clusters are the largest physical laboratories available for studying hydrodynamical processes such as shocks, sound waves and contact discontinuities and

in particular their X-ray emission can be studied in these terms. However, if it comes to smaller scales, other astrophysical processes that are related to the formation of galaxies become important. Effects such as the feedback from AGN change the cosmic baryons and the observational properties of the structures. Fig. 1.10 shows a composite image of the galaxy cluster MS0735.6+7421 in radio optical and X-ray wavelength from McNamara et al. (2005). We can see that the signatures of the different wavelength differ substantially. The individual galaxies are visible in the optical data. The hot X-ray emitting gas that permeates the whole galaxy cluster is shown in blue and the radio emission in form of two radio jets originating from the central AGN is shown in red. Galaxy clusters do not only emit radiation but they also leave an imprint in the cosmic microwave background (CMB) through inverse Compton scattering which is called the Sunyaev-Zel'dovich effect. This effect can be used to trace clusters independently from their redshift and is described in detail below.

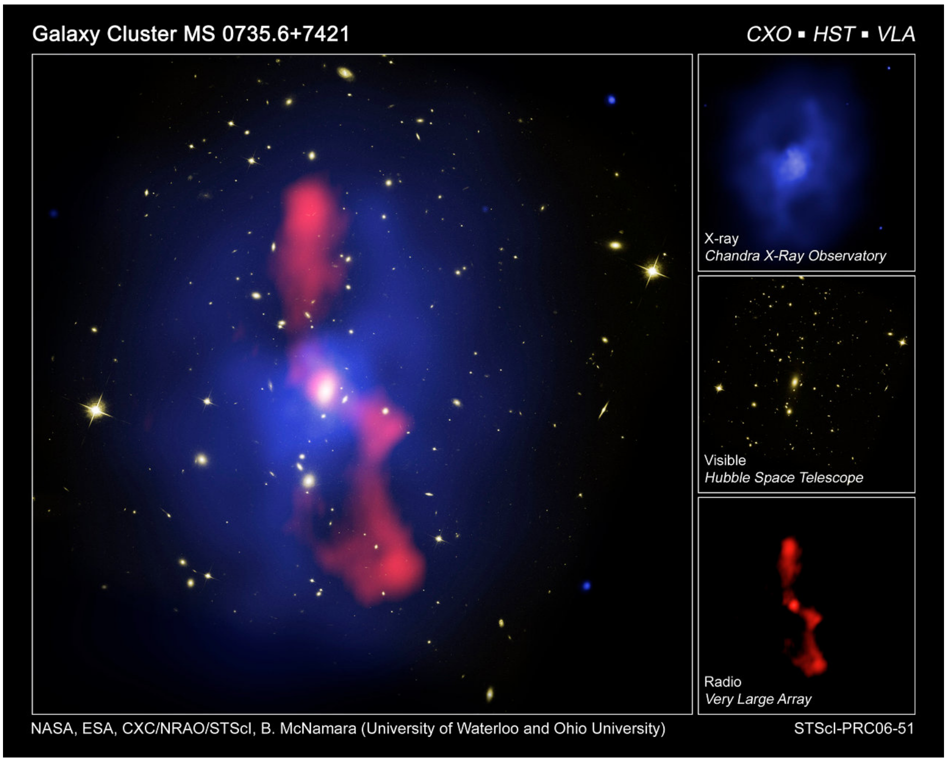

Figure 1.10 This composite image shows the galaxy cluster MS0735.6+7421. The optical view of the galaxy cluster, taken by the Hubble Space Telescope's Advanced Camera for Surveys in February 2006, shows dozens of galaxies bound together by gravity. Diffuse, hot gas permeates the space between the galaxies and emits X-rays, seen as blue in the image taken with the Chandra X-ray Observatory in November 2003. The cavities are filled with charged particles gyrating around magnetic field lines and emitting radio waves shown in the red portion of image taken with the Very Large Array telescope in New Mexico in June 1993. (X-ray: NASA/CXC/Univ. Waterloo/(McNamara et al., 2005); Optical: NASA/ESA/STScI/Univ. Waterloo/(McNamara et al., 2005); Radio: NRAO/Ohio Univ./(Birzan et al., 2004).

1.4.1 Sunyaev-Zel'dovich Effect

The Sunyaev-Zel'dovich (SZ) effect is the spectral distortion of the cosmic microwave background (CMB) through inverse Compton scattering by electrons present in the hot and ionized gas in galaxy clusters. The low-energy CMB photons receive an average energy boost during collision with the high-energy cluster electrons, see fig. 1.11 (Sunyaev & Zeldovich, 1970, 1972). In general, Compton scattering involves the transfer of energy between a photon and a free electron. In the context of the SZ effect, CMB photons passing through a region with a population of high-energy electrons experience energy changes due to scattering interactions. These interactions result in a distortion of the CMB spectrum. The resulting CMB anisotropy has a distinctive frequency dependence, which causes a deficit of photons below and an excess above $\nu_{\mathrm{null}} = 217.6\,\mathrm{GHz}$. The change in CMB temperature ΔT as a function of frequency due to the (non-relativistic) thermal Sunyaev-Zel'dovich (tSZ) effect is given by

$$\frac{\Delta T}{T_{\mathrm{CMB}}} = y\left(x\frac{e^x+1}{e^x-1} - 4\right), \tag{1.5}$$

where the dimensionless Compton-y parameter is defined as

$$y \equiv \int dl\,\sigma_T \frac{n_e k\left(T_e - T_{\mathrm{CMB}}\right)}{m_e c^2}, \tag{1.6}$$

where σ_T is the Thomson cross-section, k is the Boltzmann constant, m_e is the electron mass, c is the speed of light, n_e is the electron number density, T_e is the electron temperature, $T_{\mathrm{CMB}} = 2.725$ K is the CMB temperature used throughout this thesis, l is the line-of-sight distance over which the integral is performed, and x is the dimensionless frequency given by $x \equiv h\nu/kT_{\mathrm{CMB}} = \nu/56.81\,\mathrm{GHz}$, with Planck constant h. Importantly, the frequency shift due to this scattering process does not depend on the redshift of the source. This is due to the basic nature of Compton scattering, the relativistic invariance of the process, and the fact that the scattering interactions are local to the gas and not directly influenced by the expansion of the universe.

The SZ effect is divided into the thermal and kinematic components. The thermal component, often referred to as the tSZ effect, arises from the pressure of the hot electrons within the gas. The kinematic component, also known as the kinetic SZ effect, stems from the bulk motion of the gas, such as the peculiar velocity of a galaxy cluster relative to the CMB rest frame. For reviews on the SZ effect we also refer to e.g. Birkinshaw (1999); Carlstrom et al. (2002).

As the tSZ effect provides a possibility to directly measure the pressure of the ICM, it also offers insights into the clusters mass distribution and thermal properties. By comparing tSZ observations with X-ray measurements, the clusters mass can be independently determined making it a powerful tool for understanding the relationship between visible matter and dark matter (Battaglia et al., 2013).

By studying the thermal SZ effect, also information about the feedback processes that have influenced the gas within the cluster can be inferred. While the thermal SZ effect itself is not considered a feedback process, it can provide valuable information about the feedback processes occurring within galaxy clusters: Feedback processes, such as those involving AGN or supernova-driven galactic winds, can inject energy into the ICM of galaxy clusters. This energy heats the gas, causing it to reach high temperatures. When CMB photons pass through this hot ICM, they undergo scattering off the electrons in the gas, resulting in the thermal SZ effect.

Observing the tSZ effect therefore provides insights into the energy injection and regulation mechanisms that shape the properties of the gas within cluster environments (Battaglia et al., 2010; Dolag et al., 2016; McCarthy et al., 2014).
Observations and analysis that made use especially of the tSZ-effect have also been studied in terms of the missing baryon problem. These approaches support the assumption that the missing baryons are most likely contained in the WHIM which connects galaxy pairs (Chaves-Montero et al., 2020; de Graaff et al., 2019; Nicastro et al., 2013).

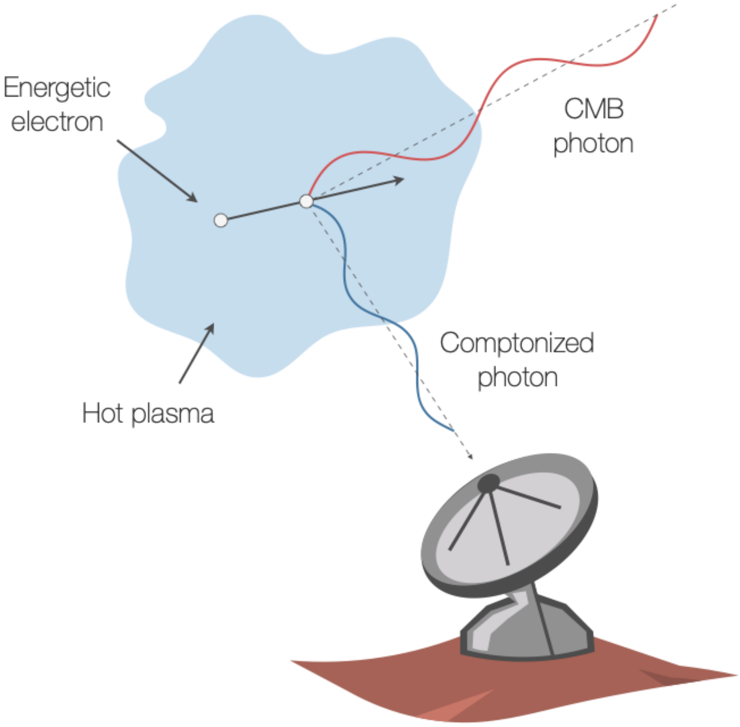

Figure 1.11 A CMB photon (red) that enters the hot ICM (light blue) from a variable angle is up-scattered to higher energy (blue) by an electron (black) on average . The largest energy is passed onto the photon when it is scattered into the direction of the incoming electron. The minimal energy is passed when deflected into the direction opposite to the incoming electron. However, on average scattering constellations with $\sim 90°$ angles between the particles are most relevant for the tSZ effect. The total momentum in the interaction is conserved, so the electron is essentially undeflected by the interaction (Mroczkowski et al., 2019a).

1.5 This Thesis

The preceding sections focused on the theoretical background and scientific context of the projects that are contained in the further course of this thesis: The different types of galaxies, the environments of galaxies and the largest blocks of the Universe, galaxy clusters. We studied different mechanisms that affect these extragalactic targets and we have gone through different feedback processes that are connecting these objects on different scales. One central subject in this work is the CGM, as it connects as well with the IGM of the galaxy itself, as with the ISM outside of the galaxies corona. This thesis aims to study different feedback processes that influence the CGM such as magnetic feedback and feedback from AGN. In this work we use a multi-wavelength approach: We use data across almost the whole electromagnetic spectrum as different processes leave imprints in different wavelengths. Each band has therefore its own unique properties and structures that can be interpreted in terms of different physical processes.

Radio data is crucial for investigating non-thermal processes in astrophysical systems as radio continuum emission often arises from synchrotron radiation produced by high-energy electrons spiraling in magnetic fields. Observations in the radio regime are therefore used to study AGN and their powerful jets as the synchrotron emission from these jets provides insights into the presence and properties of black holes and their accretion disks. Radio observations are also used to measure rotation measure (RM) to infer information about magnetic field strength in the CGM extent.
Millimeter-wave and submillimeter observations are essential for probing thermal processes, such as molecular gas and dust emission and the thermal Sunyaev-Zel'dovich effect. The tSZ effect is a technique for probing the hot gas of massive halos such as the ICM and CGM. Pressure and the integrated energy can be directly inferred from SZ measurements. SZ data therefore enables the study of feedback processes in galaxy clusters, including heating and cooling, as well as the presence of AGN-driven shocks.
Optical light is primarily emitted by stars and contains therefore information about a galaxies star-formation rate, stellar mass and redshift. It is also used to identify the optical counterpart to a radio galaxy, its host.
X-ray data is critical for studying high-energy processes in astrophysical systems. It reveals the presence of hot gas, typically with temperatures $T > 10^6$ K within galaxy clusters, but also the CGM. X-ray observations are instrumental in characterizing AGN feedback processes, including the heating and cooling of gas in the ICM and they provide insights into the energy and mass distribution within galaxy clusters.

In the following chapters we describe different projects that examine these processes in detail that I have carried out in my three years as a doctoral student.
Chapter 2 describes a research project where we measure magnetic fields in the CGM using polarization data from the radio telescope MeerKAT. The data analysis was carried out by myself, the data I used is provided by the MeerKAT consortium. The main research question that is investigated in this work is if magnetic fields are present in the expanses of the CGM and if rotation measure analysis are sufficient to measure these magnetic fields.
In chapter 3 we introduce a project where a combination of radio, optical and X-ray data is used to study feedback from central AGN in clusters with regard to their cluster surrounding. The data analysis in this project was fully carried out by myself. The X-ray data I used is provided

by the eROSITA consortium, the radio data is provided by the ASKAP consortium and the optical data is public data from the legacy survey. The main goal of this work is to investigate AGN feedback and to examine how this feedback influences the cluster environment.
The last project is described in chapter 4. In this project we use infrared and SZ data from the missions WISE, SPT and ACT to study the SZ effect around massive elliptical galaxies. The data analysis in this project was not carried out by myself, I created the galaxy catalog that was analyzed using the public data from the WISE and DES project. This project also aims to study feedback models by stacking the SZ data to investigate and distinguish radiative and radio mode of AGN feedback. Fig. 1.12 gives an overview of the different wavelengths observations and their application within this thesis.
Together, these projects offer a comprehensive view of the interplay between galaxies, their environments and the CGM, with special attention to the complex feedback mechanisms at work in extragalactic systems.

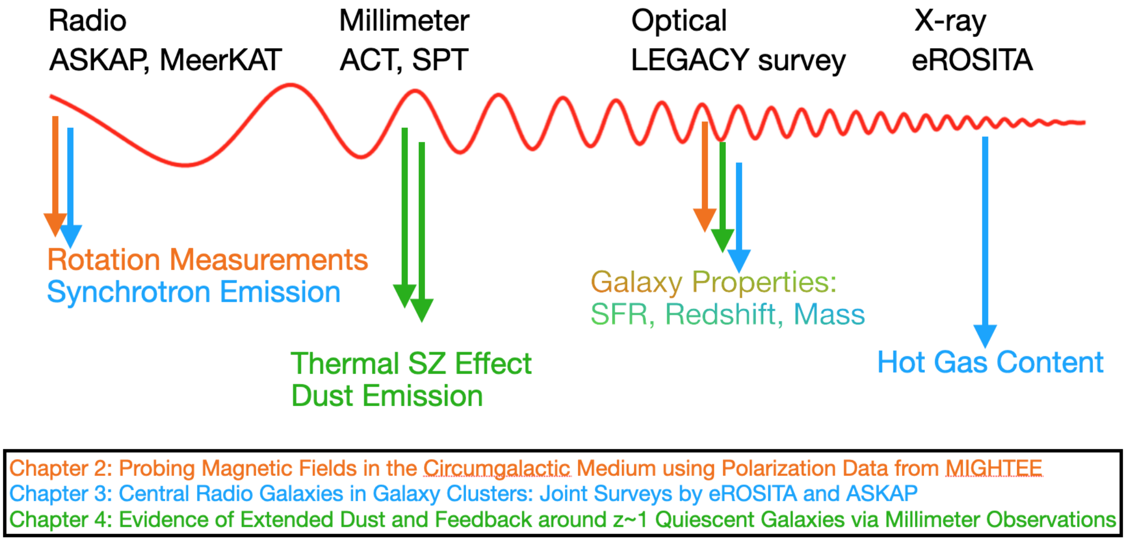

Figure 1.12 An overview of the different observations that are used within this thesis and their applications to the individual projects.

2 Measuring CGM Magnetic Fields with Background Rotation Measures

This chapter is based on the article "Probing magnetic fields in the circumgalactic medium using polarization data from MIGHTEE", K. Böckmann, M. Brüggen, V. Heesen, A. Basu, S. P. O'Sullivan, et al., 2023, A&A Volume 678, A56

2.1 Introduction

The diffuse gas embedded between the interstellar medium (ISM) and the baryon-rich intergalactic medium (IGM) of a galaxy is known as the circumgalactic medium (CGM), which typically extends up to the virial radius of galaxies ≈ 200 kpc. The existence of this extended gaseous halo is a fundamental prediction of galaxy formation theory (e.g., Tumlinson et al., 2017). Observations and simulations from across the whole electromagnetic spectrum and redshifts suggest that the CGM gas has a major impact on galaxy evolution and on the chemical history and evolution of a galaxy (e.g., Donahue & Voit, 2022b). Firstly, it receives enriched material that was expelled in the form of outflows; secondly, it also acts as a reservoir of fuel for future star formation, including the infalling IGM gas (Machado et al., 2018). One powerful tool that is used to study the tenuous multi-phase CGM are transverse absorption-line studies using background quasars, which enables one to determine the relative abundance of various elements and thus the metallicity of the gas (DeFelippis et al., 2021; Mintz et al., 2020).

Magnetic fields are an important non-thermal component in and around galaxies that affect the dynamics and structure of the CGM. In particular, they are believed to play an important role in the transport of materials to and from disks into the CGM (Arámburo-García et al., 2023) and affect how gas is accreted onto galaxies (Heesen et al., 2023). However, little is known about the dynamical importance of the magnetic fields and their evolution in galaxies and the surrounding CGM over cosmic time. Moreover, it is not yet understood how the CGM gets magnetized in the first place. Two possible scenarios have been discussed: (i) magnetic fields could be generated by small-scale dynamo effects (Pakmor et al., 2017, 2020) and (ii) magnetic fields could be generated in the disk and subsequently transported out via galactic winds and outflows (Péroux et al., 2020). In the former case, we expect the resulting magnetic fields to be turbulent with no ordered fields on the size of the CGM. However, the turbulent magnetic fields can be converted to anisotropic fields by shear flows (Fletcher et al., 2011). If galactic winds and feedback are the origin of the magnetized CGM, a strong azimuthal dependence with the galactic disk is expected because the outflows are usually along the minor axis. This is valid for both, stellar and AGN (Active Galatic Nuclei) driven feedback (Pillepich et al., 2021; Thomas et al., 2022).

Magnetic fields in nearby (distance < 50 Mpc) star-forming disk galaxies have been studied in some detail, with most studies indicating the existence of a galactic dynamo (Beck, 2015; Beck et al., 1996). For more distant galaxies at redshift $z > 0.1$, the data is scarcer with only a few studies existing (Bernet et al., 2008; Farnes et al., 2014; Kim et al., 2016; Lan & Prochaska, 2020; Mao et al., 2017; Oren & Wolfe, 1995). Measuring the magnetic fields directly via synchrotron emission is usually limited to regions close to the galactic disk due to spectral aging (Miskolczi et al., 2019). Hence, the direct mapping of the magnetic field structure and strength in galaxies at higher redshifts will be a challenging and important task for the next generation of radio telescopes, such as the Square Kilometre Array (SKA).

In this paper we use Faraday rotation to examine the magnetic fields around galaxies. Faraday rotation is a process that rotates the polarization angle of linearly polarized light when passing through an ionized and magnetized medium. The intervening medium causes a difference in the phase velocity between the left-handed and right-handed circular polarization components of the linearly polarized synchrotron radiation. Using the polarization angle ψ, the observed wavelength λ and the Faraday depth ϕ, the Faraday rotation can be described by a rotation of the intrinsic polarization angle:

$$\psi(\lambda^2) = \psi_0 + \phi\lambda^2. \tag{2.1}$$

The Faraday rotation measure (RM) modifies the polarization angle via

$$\psi(\lambda) = \psi_0 + \mathrm{RM}\lambda^2. \tag{2.2}$$

Faraday rotation of distant background radio sources has been used to probe extragalactic magnetic fields (Pomakov et al., 2022). The RM of the polarized light from background radio sources passing through the magnetized CGM can be used as a tracer of the strength and extent of magnetic fields around galaxies out to distances of hundreds of kiloparsecs. The RM is assumed to be positive when the line-of-sight average component of the magnetic field points toward the observer, otherwise it is negative for a field with an average component pointing away from the observer (Vacca et al., 2016). For a polarized radio source at redshift z, the RM is defined as

$$\frac{\mathrm{RM}}{\mathrm{rad\,m^{-2}}} = 0.81 \int\limits_{\mathrm{z}}^{0} \frac{1}{(1+z)^2} \left(\frac{n_e(z)}{\mathrm{cm^{-3}}}\right) \left(\frac{B_{\|}(z)}{\mu G}\right) \left(\frac{\mathrm{d}r(z)}{\mathrm{d}z}\right) \mathrm{d}z. \tag{2.3}$$

The RM has units of $\mathrm{rad\,m^{-2}}$, the free electron number density n_e is in $\mathrm{cm^{-3}}$, the magnetic field component along the line of sight $B_{\|}$ is in Gauss and the comoving path increment per unit redshift $\mathrm{d}l/\mathrm{d}z$ is in parsec. This equation assumes a uniform RM screen across the source and a spatial separation of the linearly polarized source and the Faraday rotating plasma (Akahori et al., 2016; Bernet et al., 2012).

Previous work has studied the Faraday rotation properties of background quasars with strong intervening Mg II lines in their spectra. Mg II absorption is usually associated with the halos of normal galaxies. The absolute values of RM are found to be correlated with the presence of intervening Mg II absorption, which is thought to arise in outflowing material from star forming galaxies (Kacprzak et al., 2008; Kim et al., 2016). Work of Bernet et al. (2010, 2008) showed that Mg II absorbers exhibit the highest |RM| at frequencies of 5 GHz and above. At lower frequencies, the effect of Faraday depolarization becomes stronger because the Faraday rotation is proportional to the square of the wavelength (eq. (2.1)). Bernet et al. (2013) examined the |RM| distribution with respect to the impact parameters of galaxies finding that all sightlines with high |RM| pass within 50 kpc of a galaxy and that the |RM| distribution for low impact parameters, $D < 50$ kpc, is significantly different than for larger impact parameters. Farnes et al. (2014) examined 1.4 GHz data of 599 optically identified non-intrinsic MgII absorption systems with polarized background radio sources finding that the excess of |RM| is still present in that frequency range but only for sources where the impact parameters between the quasar and the polarized emission are small.

Recently, Heesen et al. (2023) studied the residual rotation measures (RRMs) observed with the LOw Frequency ARray (LOFAR) around 183 nearby galaxies of the Palomar survey that were selected by apparent *b*-band magnitude (Carretti et al., 2023). Since Faraday rotation is proportional to the wavelength squared, LOFAR high-band frequencies (144 MHz in this study) afford high-precision RM measurements (O'Sullivan et al., 2023) at the cost of smaller source densities owing to depolarization. This work showed, for the first time, an RM along the minor axis of inclined galaxies for impact parameters of less than 100 kpc. These results suggest a slow decrease of the magnetic field strength with distance from the galactic disk, as expected if the CGM is magnetized by galactic winds and outflows. We note that this work focuses on nearby galaxies that are believed to have a smaller fraction of star-formation driven outflows than at higher redshifts.

Here, we measure the RM around foreground star-forming galaxies using early-release data from the MeerKAT MIGH- TEE polarization survey (MIGHTEE-POL, Taylor et al., in prep) with the aim to measure the rotation measure profile out to distances of 300–400 kpc from the star-forming galaxies. This provides information about the magnetic fields in the CGM and galactic winds. We use catalogs of star-forming and blue cloud galaxies to measure the rotation measure of MIGHTEE-POL sources as a function of the impact parameter from the foreground galaxy. We use catalogs of star-forming galaxies since RMs are expected to be higher around star-forming galaxies than around quiescent galaxies. This is due to the fact that the interstellar medium in star-forming galaxies is more turbulent and magnetized, which leads to an increase of the RM. Star formation processes, such as supernova explosions and outflows from young stars, can amplify the magnetic field and drive magnetized outflows on galactic scales (Basu et al., 2018; Wiener et al., 2017).

This paper is organized as follows: In Section 2.2 we describe the data and our sample selection and describe the methods in Section 2.3. We present the results in Section 2.4 and discuss them in Section 2.5. We close with a conclusion in Section 2.6.

2.2 Data

The MIGHTEE survey (MeerKAT International GHz Tiered Extragalactic Exploration, (Jarvis et al., 2016)) is a survey that is being conducted using the MeerKAT radio telescope in South Africa. It is one of MeerKAT's flagship Large Survey Projects, using simultaneous continuum, spectropolarimetry (Sekhar et al., 2022) and spectral line (Maddox et al., 2021) measurements to investigate the formation and evolution of galaxies over cosmic time (Heywood et al., 2022).

The MIGHTEE survey is imaging four extragalactic fields, Cosmic Evolution Survey (COSMOS; Scoville et al., 2007), *XMM* Large-Scale Structure survey (*XMM*-LSS; Pierre et al., 2004), CDFS, and ELAIS-S1. All fields are observed at L-band from 880—1680 MHz, with a central frequency of 1284 MHz in multiple pointings that are mosaicked to a final image with a thermal noise sensitivity of approximately 2 μJy beam^{-1}. In this work we make use of early-release data products from the MeerKAT MIGHTEE polarisation survey (MIGHTEE-POL) (Taylor et al. 2023, in prep). The MIGHTEE-POL survey aims to study the polarized emission from extragalactic radio sources and the properties of magnetic fields in the Cosmic Web including the large-scale structure. The survey will cover an area of about 20 square degrees of the sky, with a resolution of ≈ 5 arcseconds. The survey is expected to be completed in 2023 and the data will be made publicly available to the scientific community. In this work, we use continuum data early-release products from the MIGHTEE-POL survey of the COSMOS and *XMM*-LSS fields. The COSMOS field consists of one pointing, for the *XMM*-LSS field three pointings are mosaicked together. The MIGHTEE-POL cataloge of the *XMM*-LSS field consists of 243 sources and the catalog of the COSMOS field consists of 111 sources. For a detailed description about the method of data processing see (Taylor et al. 2023, in prep). Compared to lower frequency observations, e.g. with LOFAR, our polarised source density is higher because depolarisation is lower. The flip side is that our individual RM values are less accurate as the angle shift depends on λ^2. In our data the average error on the RM is $\mathrm{RM_{err}} =$ 2.4 rad m^{-2} .

The redshift distribution of the host sources is shown in the upper panel of Fig. 2.1. In order to identify intervening galaxies in the *XMM*-LSS field we use the "blue cloud" galaxy catalog from Basu et al. (2015). This catalog consists of 36776 blue galaxies with their spectroscopic redshifts from the PRism MUltiobject Survey (PRIMUS) up to a redshift of $z = 1.18$. A color-magnitude diagram based separation was introduced to only select blue star-forming galaxies. Furthermore, the PRIMUS team identified the AGN in their sample by fitting AGN spectral templates to remove AGN from the normal galaxy sample. In this catalog, due to the evolving main-sequence, high-z blue cloud galaxies tend to be luminous infrared galaxies (LIRGs) and ultra-luminous infrared galaxies (ULIRGs), and therefore dominated by mergers.

For the COSMOS field we use the galaxy catalog provided by Sinigaglia et al. (2022). This sample was derived from the parent sample by Weaver et al. (2022). A color–color $NUV - r/r - J$ plane selection was applied to only select star-forming galaxies. This catalog contains 9022 star-forming galaxies and their spectroscopic redshifts between $0.23 < z < 0.48$. Note that this sample is the result of the combination of several different surveys, performed with different survey strategies (Davies et al., 2018; Weaver et al., 2022).

The distribution of the locations of intervening and host galaxies across the sky for both fields is shown in Fig. 2.2. We can see that the optical survey used in the catalog creation for the *XMM*-LSS field has a smaller footprint than the MIGHTEE survey. This reduces the size of the *XMM*-LSS field.

In addition to the two spectroscopic galaxy catalogs we also make use of two photometric galaxy catalogs (one for each field) provided by Hatfield et al. (2022). These catalogs were computed with optical and near-infrared data from VISTA and HyperSuprimeCam (VISTA Deep Extragalactic Observations, VIDEO: Jarvis et al. (2013); HSC: Aihara et al. (2018)). We remove sources without redshift and magnitudes and implement a cut on the apparent

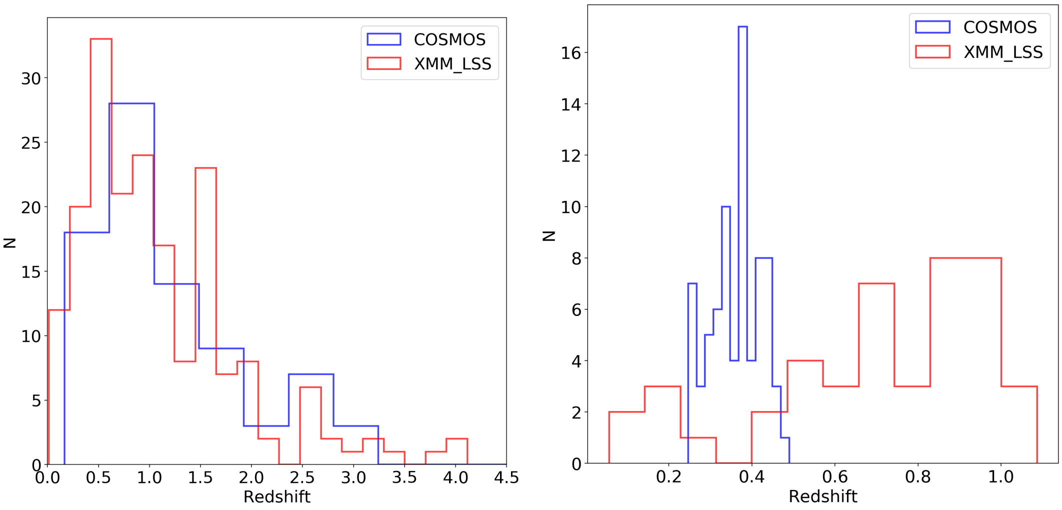

Figure 2.1 *Upper Panel:* The redshift distribution of the host sources in the COSMOS field (blue) and the *XMM*-LSS field (red).
Lower Panel: Histogram showing the redshift distribution of the 81 intervening galaxies in the COSMOS field (Sinigaglia et al., 2022) that have matched host sources within a distance of 400kpc in blue and the redshift distribution of the 44 intervening blue cloud galaxies in the *XMM*-LSS field (Basu et al., 2015) that have matched host sources within a distance of 400 kpc in red.

Ks magnitude of $m_K < 23.7$. The magnitude cut is introduced to ensure uniformity and comparability between the two catalogs, given that the initial depth of the COSMOS catalog exceeds that of the *XMM*-LSS catalog by 1 magnitude. After doing so, we are left with 125676 sources for the COSMOS field and 384354 sources for the *XMM*-LSS field. The redshift range for the COSMOS field is $0.001 < z < 5.65$ with a median g-band magnitude of $M_g = -19.1\,\mathrm{mag}$. For the *XMM*-LSS we get $0.0001 < z < 6.45$ a median g-band magnitude of $M_g = -20.3\,\mathrm{mag}$. We use these catalogs to find the total number of intervenors to each host galaxy and to test for a correlation between the mean impact parameter of all intervenors and |RM| as these catalogs are more complete than the pure spectroscopic samples. Also, these catalogs provide the mass and star-formation rate of each galaxy which we use for our analysis. We note that the photometric galaxy catalogs include subsets of the spectrocopic catalogs. However, these catalogs do not overlap completely, which is visible in Fig. 2.2. As the spectroscopic catalogs were created with certain selection criteria applied to them, resulting in a non-complete sample, we are considering a significantly more comprehensive sample by using the additional photometric catalog.

2.3 Method

2.3.1 The spectroscopic sample

In order to measure the RM induced by the CGM of the intervening galaxies, we need to associate the background sources with the intervening sources. For each background source, we search for an intervening galaxy within a projected distance of less than 400 kpc at the redshift

Table 2.1 This table lists the properties of the background radio sources and intervenors in the spectroscopic galaxy catalogs in the COSMOS and *XMM*-LSS field. N_{host} refers to the total numbers of host galaxies from the MIGHTEE sample, N_{spec} are the total numbers of galaxies in the spectroscopic catalogs, N_{matched} are the numbers of matches for the hosts, z_{spec} is the redshift range of the galaxies in the spectroscopic catalogs and reference is the reference paper.

Field	N_{host}	N_{spec}	N_{matched}	z_{spec}	Reference
COSMOS	111	9,022	81	0.25–0.49	Sinigaglia et al. (2022)
XMM-LSS	243	36,776	44	0.06–1.09	Basu et al. (2015)

of the intervening source. If more than one intervening galaxy matches a host source, we chose the one with the minimum central distance. We only select sources where $z_{\mathrm{Host}} > z_{\mathrm{Intervenor}}$ to ensure that the intervening galaxy lies in front of the host galaxies. For the *XMM*-LSS galaxy sample, we introduce a magnitude cut of $M_u > -22\,\mathrm{mag}$. The u-band magnitude is an indicator for star-forming galaxies as the UV light is primarily emitted by hot, young, massive stars (Calzetti, 2013). M_u and M_g are comparable and only differ by a value of $0.4\,\mathrm{mag}$ on average. Our magnitude cut does not impose any constraint on the initial catalog as the spectroscopic survey goes down to apparent magnitudes of $m_g = 27$ and an absolute magnitude of $M_g = -22$ converts to an apparent magnitude of $m_g = 23.1$ at redshift $z = 1$. This leads to the result that no galaxies in our magnitude range are cut from the catalog. In addition, by introducing the cut we select more massive galaxies which leads to more massive galactic halos which in turn may lead to a denser environments with a larger RM.

By matching the catalogs and after removing duplicates we are left with 81 (44) matches for the COSMOS (*XMM*-LSS) spectroscopic samples, see Table 3.2. As we have more volume to detect brighter galaxies at the higher redshift we add a bias by introducing a magnitude cut to our intervening galaxy sample due to the shape of the luminosity function. The redshift distributions of both samples of the intervening galaxies are shown in the lower panel of Fig. 2.1.

We do not correct the RM values for Galactic contamination by the Milky Way because we only look at very small patches on the sky, $1.6\,\mathrm{deg}^2$ for the COSMOS field and $3.5\,\mathrm{deg}^2$ for the *XMM*-LSS field. Hence, we expect a negligible gradient over these small sky patches and assume the contribution of the Milky Way for each field is constant over all sources and therefore not affecting our analysis. Nonetheless, we note that (Taylor et al. 2023, in prep) found the median Galactic contribution (Galactic Rotation Measure; GRM) of the *XMM*-LSS field to be $8.9 \pm 3.7\,\mathrm{rad\,m^{-2}}$ and of the COSMOS field to be $0.9 \pm 4.1\,\mathrm{rad\,m^{-2}}$. We note that we find fewer matches for the *XMM*-LSS sample, although the *XMM*-LSS field is larger than the COSMOS field. This is due to the introduced magnitude cut which reduces the numbers of matches from 168 to a number of 44 which is further discussed in Section 2.5.

For both of our samples, we calculate the impact parameter which is the separation between the background source and the center of the foreground galaxy in kpc. For our analysis we use the absolute value of the rotation measure, |RM|. Special care needs to be taken to compute the errors because the |RM| are an absolute quantity. The error on |RM| was calculated by assuming that the error on RM follows a Gaussian distribution. For each value of RM, we

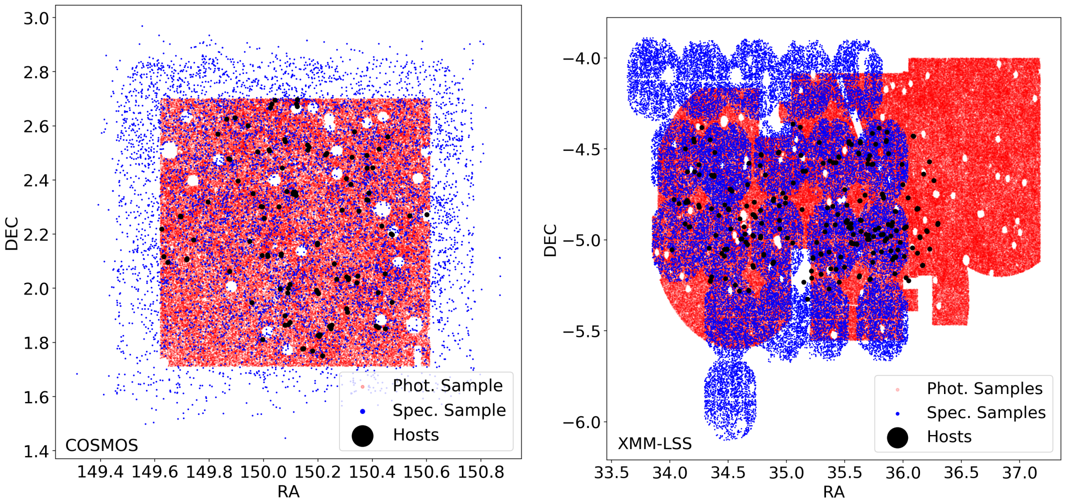

Figure 2.2 *Upper Panel:* We show the distribution of the intervening galaxies for the COSMOS field from the spectroscopic catalog by Sinigaglia et al. (2022) in blue and the distribution of the corresponding COSMOS MIGHTEE host galaxies in black. The intervening galaxies from the photometric (Hatfield et al., 2022) sample are shown in red.
Lower Panel: We show the distribution of the intervening galaxies for the *XMM*-LSS field from the spectroscopic catalog by Basu et al. (2015) in blue and the distribution of the corresponding *XMM*-LSS MIGHTEE host galaxies in black. The patchy distribution results from the pointings of the Inamori Magellan Areal Camera of the Magellan Telescope at Las Campanas Observatory. The intervening galaxies from the photometric (Hatfield et al., 2022) sample are shown in red.

generated a random sample of |RM| drawn from an underlying Gaussian distribution, with a mean value of RM and standard deviation given by the measured error on RM. We then consider the 68 percentile ($\equiv 1\,\sigma$) interval of the distribution of |RM|, centered at the median value of the distribution, as the error on each |RM|.

In order to investigate the excess of |RM| at smaller impact parameters, we bin the data points. For the typical mass of our galaxies, we expect a virial radius of ≈150–200 kpc. Thus, we compute three bins with an approximately equal number of objects, each with a width of 133 kpc in impact parameter. In each bin we calculate the median values of |RM| and follow the procedure of Arámburo-García et al. (2023) to estimate the error in each bin using:

$$|\mathrm{RM}|_{\mathrm{err,bin}} = \sqrt{\frac{\left\langle (x_i - \langle x \rangle)^2 \right\rangle}{n}}, \tag{2.4}$$

where x_i are |RM| values in each bin, $\langle x \rangle$ is their median value and n is the number of objects in each bin. We then plot the observed |RM| in $\mathrm{rad\,m^{-2}}$ versus the impact parameter in kpc for both samples. First, we show the observed |RM| in $\mathrm{rad\,m^{-2}}$ versus the impact parameter for the *XMM*-LSS without the magnitude cut of $M_u > -22$ mag of that we introduced in order to mainly select massive star-forming galaxies. As we can see in Fig. 2.3, this increases the number of matches of intervenors and hosts for the sample to 168 but we do not detect any excess if we also include faint galaxies with $M_u < -22$ mag.

2.3.2 The photometric sample

Using the spectroscopic sample, we only investigate the RM contribution from one massive, bright intervenor with the smallest impact parameter to the host. However, as the RM is an integral along the line of sight to the background radio source, we also investigate how the number of intervenors N_{int} and the mean impact parameter between a host and all its intervenors varies with the total RM of each host. The spectroscopic galaxy catalogs that we use for our analysis are incomplete in terms of magnitude and redshift and are only a subset of galaxies that lie between host and observer. In order to examine the total numbers of intervenors to each host we make use of the photometric catalogs from Hatfield et al. (2022) that contain more than 100.000 galaxies for each field to identify all intervenors to each host within a certain impact parameter.

We identify all intervening galaxies within an impact parameter of 133 kpc for each host galaxy in the two samples. We do not apply any cuts on magnitude or star-formation rate. For every host galaxy we compute the mean impact parameter to all its intervenors to investigate if there is a connection to the total |RM|. In addition, we recognize that galaxies with higher rates of star-formation are expected to exhibit stronger magnetic fields. Thus, we assume that these galaxies contribute more significantly to the total |RM| signal. We introduce a weighting scheme with respect to the impact parameter to account for the correlation between impact parameter and |RM|. The introduced weighting scheme allows us to explicitly account for the relative importance of each galaxy in the final analysis. The weighting is introduced as follows

$$\mathrm{IP}_{\mathrm{weighted,mean}} = \frac{\sum_i \mathrm{SFR}_i \, \mathrm{IP}_i}{\sum_i \mathrm{SFR}_i}, \tag{2.5}$$

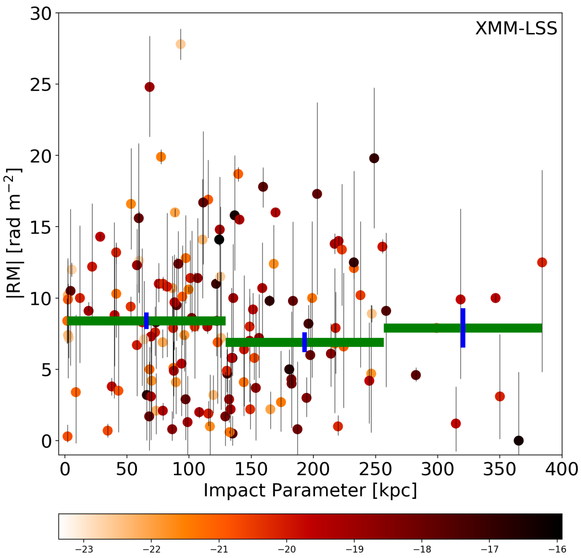

Figure 2.3 Observed |RM| in rad m^{-2} versus impact parameter in kpc for the *XMM*-LSS without the magnitude cut. The green bar indicates a bin of individual data points with the blue line being the error bar of the bin. The individual data points are color-coded with their corresponding u-band magnitude.

where SFR_i is the star-formation rate and IP_i is the impact parameter in kpc of the individual intervening galaxy. Given the fact that we obtain individual impact parameters for every intervenor to the corresponding host and we only obtain a single observable value of RM which remains the same for every host, the weighting strategy must be implemented for the impact parameters. This is necessary to ensure that each individual impact parameter is appropriately considered in the overall analysis, taking into account its unique contribution to the final result.

2.4 Results

2.4.1 The spectroscopic sample

Fig. 2.4 shows the resulting plots for the spectroscopic COSMOS and *XMM*-LSS samples after performing the magnitude cut. For the COSMOS sample we are provided with the star formation rate (SFR), we include this information in the plot and color-code the individual data points with the SFR. For the *XMM*-LSS we have the individual magnitudes and we use this information in the corresponding plot for color coding the individual data points.

We calculate the absolute RM excess *un*corrected for the intervening galaxies redshift. The total measured |RM| is a combination of GRM, extragalactic and noise components. The extragalactic |RM| consists of contributions from the invervening galaxies as well as from the foreground IGM between the source and the Milky Way as well as from contributions from the cosmic web.

For the COSMOS field that consists of a sample size of 81 we find a median |RM| of $5.9 \pm 0.9\,\mathrm{rad\,m^{-2}}$ for sources with impact parameters less than 133 kpc and $3.4 \pm 0.7\,\mathrm{rad\,m^{-2}}$ for sources with impact parameters greater than 133 kpc. This results in an excess of $2.5 \pm 1.1\,\mathrm{rad\,m^{-2}}$, which is significant at 2.3σ. For the *XMM*-LSS field that consists of a sample size of 44, the median |RM| was found to be $9.2 \pm 1.4\,\mathrm{rad\,m^{-2}}$ for sources with impact parameters less than 266 kpc and $4.2 \pm 1.8\,\mathrm{rad\,m^{-2}}$ for sources with impact parameters greater than 266 kpc. This corresponds to an excess of $5.0 \pm 2.3\,\mathrm{rad\,m^{-2}}$, which is significant at 2.2σ. The median |RM| for high impact parameters of 3.4 and $4.2\,\mathrm{rad\,m^{-2}}$ with the median of the absolute value being 0.67 of the standard deviation for a Gaussian distribution. These numbers are consistent with results for the standard deviation of extragalactic sources, corrected for the Milky Way of $\sigma_{\mathrm{RM}} = 6\,\mathrm{rad\,m^{-2}}$ found by Schnitzeler (2010).

When the samples from both fields are combined, as shown in Fig. 2.5, the median |RM| is found to be $7.3 \pm 0.8\,\mathrm{rad\,m^{-2}}$ for sources with impact parameters less than 133 kpc and $4.3 \pm 0.9\,\mathrm{rad\,m^{-2}}$ for sources with impact parameters greater than 133 kpc. This results in an excess of $3.0 \pm 1.2\,\mathrm{rad\,m^{-2}}$, which is significant at 2.5σ.

As we do not have information on the individual contributions, a redshift correction would boost all contributions although they do not all occur at the same redshift. Hence, we use the redshift uncorrected measurements to investigate the |RM| in correlation with impact parameters and only perform a redshift correction on our binned results using the mean redshift of the intervenors.

We correct the |RM| excess that we found for redshift effects to get the rest frame RM:

$$\mathrm{RM}_{\mathrm{corr}} = \mathrm{RM}(1 + z_i)^2, \tag{2.6}$$

with z_i being the redshift of the intervenor. The median redshift for the COSMOS sample is $\bar{z}_{\mathrm{COSMOS}} = 0.37$ and for the *XMM*-LSS sample it is $\bar{z}_{\mathrm{XMM-LSS}} = 0.77$. If we correct the |RM| excess for redshift we now get $4.7 \pm 2.1\,\mathrm{rad\,m^{-2}}$ for the COSMOS field and $15.7 \pm 7.2\,\mathrm{rad\,m^{-2}}$ for the *XMM*-LSS field. For the combination of both samples we find a median redshift of $\bar{z}_{\mathrm{Comb}} = 0.42$ yielding to a redshift-corrected |RM| excess of $5.6 \pm 2.3\,\mathrm{rad\,m^{-2}}$. The redshift correction of the bins is also shown in Fig. 2.5. A two-sample Kolmogorov–Smirnov test yields a p-value of 0.01, which implies a clear significance for the excess.

We also investigate a possible connection between the |RM| of the background source and the redshift of the intervening galaxy. To this end, we compute a linear fit between |RM| and redshift. Fig. 2.6 shows the |RM| vs. the redshift plot of each sample and the fit. In order to evaluate this correlation statistically, we perform a fit on the data and calculate the Pearson correlation coefficient to evaluate the linear correlation between the data and the fit. For the COSMOS data we get a positive trend with higher |RM| at higher redshifts and a correlation coefficient of 0.59 with a p-value of 0.12, suggesting that this trend is not significant. In contrast, the results for the *XMM*-LSS field indicate a negative trend with a declining |RM| towards higher redshifts. However, we note that the Pearson correlation coefficient yields 0.05 for this sample with a p-value of 0.9. So we do not detect a correlation between |RM| and redshift for the *XMM*-LSS but we see an indication for a positive correlation for the COSMOS sample.

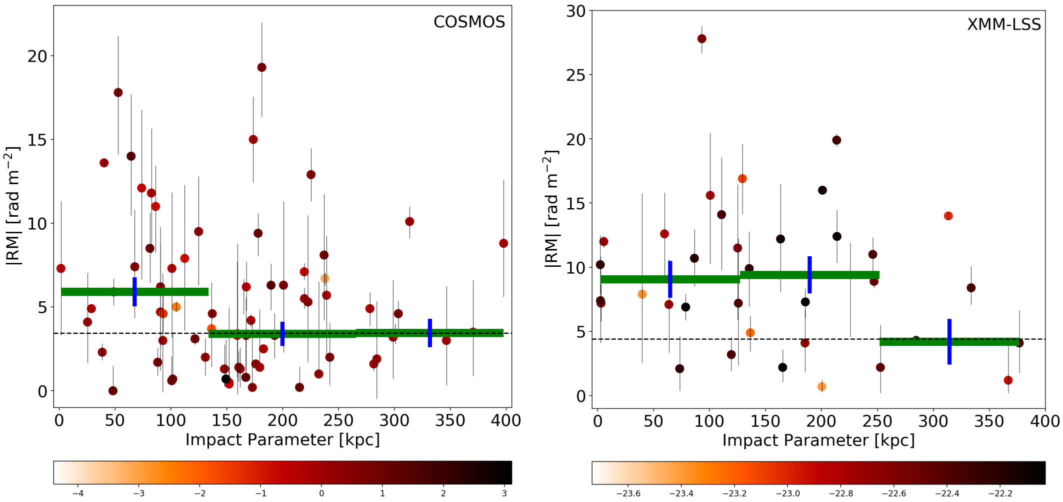

Figure 2.4 Excess |RM| as function of impact parameter for the spectroscopic samples. *Left Panel:* Observed |RM| in rad m^{-2} versus impact parameter in kpc for all 81 sources in the COSMOS field. The green bar indicates a bin of individual data points with the blue line being the error bar. The data points are color-coded with respect to the star-formation rate of each galaxy. *Right Panel:* Observed |RM| in rad m^{-2} versus impact parameter in kpc for all 44 sources in the *XMM*-LSS field. Here, the data points are color-coded with respect to the u-band magnitude of each galaxy. For both fields all error bars show the 68 percentile interval around |RM|.

2.4.2 The photometric sample

We plot the mean impact parameter of each host to all its intervenors versus the total measure |RM| treating all intervenors equally in Fig. 2.7. In addition, we color-code the individual data points with respect to the total number of intervenors N_{int} to each host to investigate a possible correlation between N_{int} and |RM|. The number of intervenors to each host within an impact parameter of 133 kpc reach from $6 < N_{\text{int}} < 66$ with the median being $\langle N_{\text{int}} \rangle = 20$ for the COSMOS field, and $6 < N_{\text{int}} < 67$ with the median being $\langle N_{\text{int}} \rangle = 18$ for the *XMM*-LSS field. The total numbers from the photometric catalog are displayed in Table 2.2. We investigate the correlation between the mean impact parameter to the total |RM| by binning the data. Again, we calculate the error of each bin as it is described in Equation (2.4). Inspecting the data in terms of N_{int} does not yield any correlation between the total number of intervenors N_{int} to the total |RM|. Binning the data does not lead to definitive results or trends for either sample. However, caution is necessary when interpreting the data, particularly in cases where the bins with larger impact parameters include only few data points. The absolute magnitudes of the intervenors are in the range of $-20.1\,\text{mag} < M_g < -12.1\,\text{mag}$ with a median of $\langle M_g \rangle = -15.5\,\text{mag}$ for the *XMM*-LSS field and of $-18.9\,\text{mag} < M_g < -13.8\,\text{mag}$ with a median of $\langle M_g \rangle = -14.8\,\text{mag}$ for the COSMOS field. This means that the galaxies in the photometric sample go down to much lower brightnesses than in the spectroscopic sample with a magnitude cut in the u-band. Even though the photometric catalogs includes most of the galaxies from the spectroscopic samples, including a large number of faint galaxies to contribute to the RM leads to a dilution of the central RM excess seen for the bright galaxies in the spectroscopic sample.

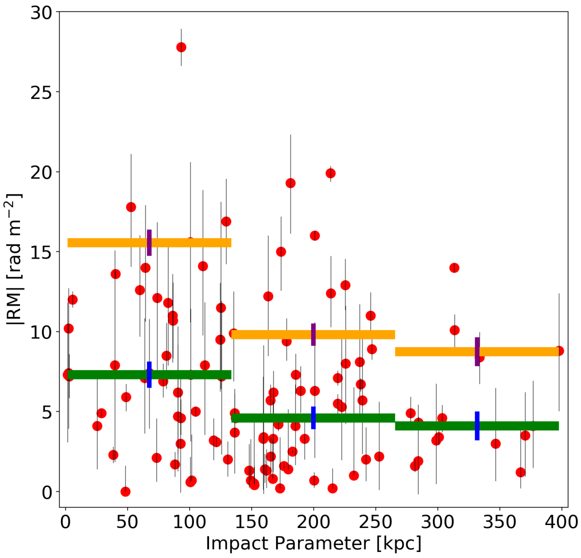

Figure 2.5 Excess |RM| as function of impact parameter for the spectroscopic sample, combined for the COSMOS and *XMM*-LSS field. Observed |RM| in rad m^{-2} versus impact parameter in kpc for the combination of the two samples. The green bar indicates a bin of individual data points with the blue line being the error bar of the bin. The orange bins are the redshift corrected |RM| including the error bar in purple. The error bars show the 68 percentile interval around |RM|.

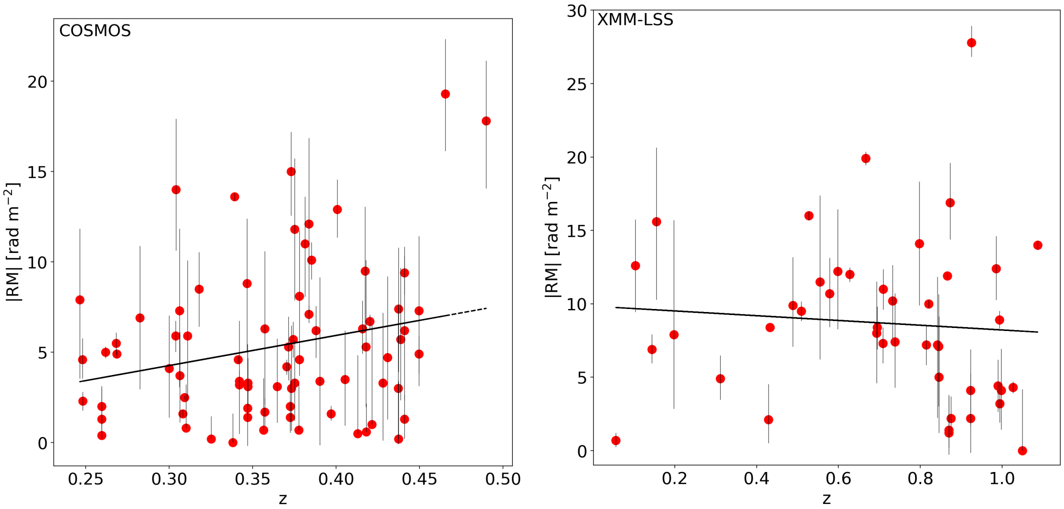

Figure 2.6 |RM| as function of redshift for the spectroscopic sample. *Upper Panel:* Observed |RM| in rad m^{-2} versus redshift for all 81 sources in the COSMOS field. The black line represents the best fit including all data points. *Lower Panel:* Observed |RM| in rad m^{-2} versus redshift for all 44 sources in the *XMM*-LSS field. Again, the black line represents the best fit. For both fields all error bars show the 68 percentile interval around |RM|.

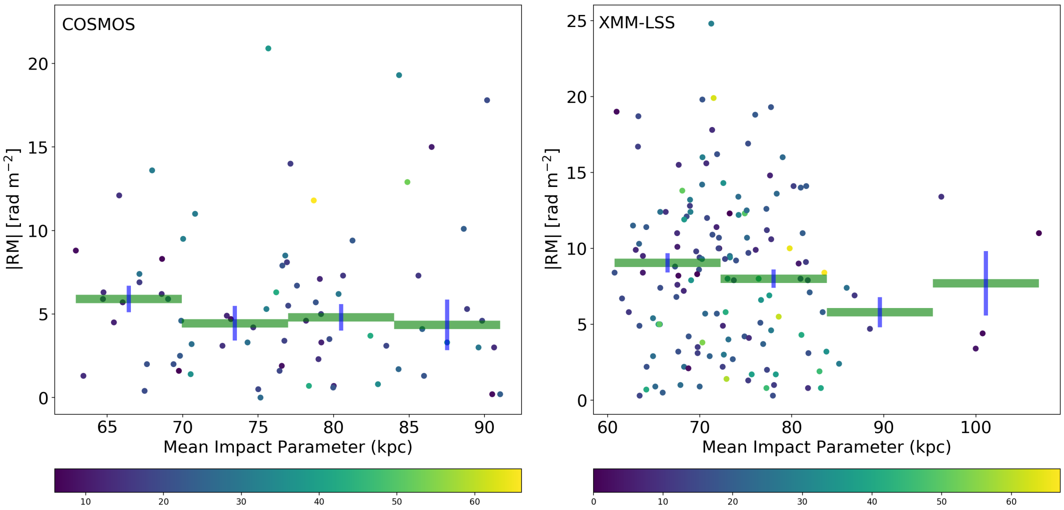

Figure 2.7 |RM| as function of mean impact parameter for the photometric sample. *Upper Panel:* We plot the observed |RM| in rad m^{-2} versus the mean impact parameter of all intervening galaxies within 133kpc around the host from the photometric catalog provided by (Hatfield et al., 2022) for the COSMOS field. The green bar indicates a bin of individual data points with the blue line being the error bar of the bin. The individual data points are color-coded with respect to the total number of intervenors to each host. *Lower Panel:* The corresponding plot for the *XMM*-LSS field.

Evidently, the photometric catalog extends to larger redshifts than the spectroscopic catalog. Since we use the redshift of each intervenor to calculate the impact parameter, we also propagate the error to the impact parameter calculation. The mean redshift of the intervenors in the two catalogs is $\langle z_{\text{int}} \rangle = 0.26$ with a mean error on the photometric redshifts of $\langle z_{\text{err}} \rangle \sim 0.08$ (Hatfield et al., 2022) which yields an impact parameter error of ±30 kpc on average.

Next, we re-compute the mean impact parameter of each host to all its intervenors versus the total |RM| applying a weighting by the star-formation rate introduced in Equation (2.5). The weighting scheme takes into account the intervenors' star-formation rate and we assume that intervenors with higher star formation rates contribute more to the |RM|. In Fig. 2.8 we show the resulting plot. Again, in both samples, we do not find any excess of |RM| at smaller impact parameters.

2.5 Discussion

2.5.1 The spectroscopic sample

We detect of an excess of |RM| for small impact parameters in both MIGHTEE fields. The COSMOS sample shows an excess at a radius below 133 kpc around the galaxy whereas the *XMM*-LSS exhibits an excess up to a radius of 266 kpc. The higher median redshift of the *XMM*-LSS sample would suggest that also the virial radius of these galaxies is larger as we are biased to more massive systems at higher redshift which is in agreement with our results. We note that we detect the excess in the *XMM*-LSS sample only if we introduce a magnitude cut

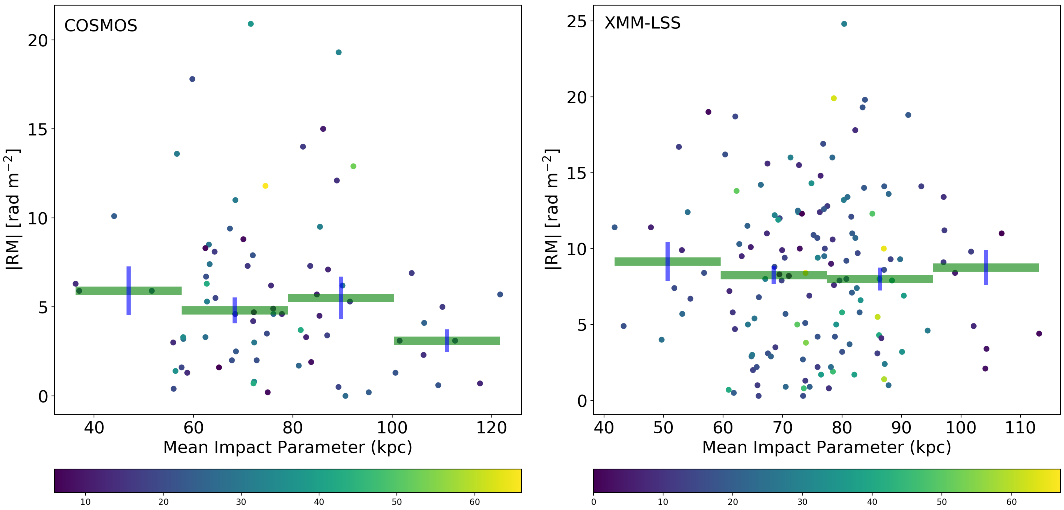

Figure 2.8 |RM| as function of weighted mean impact parameter for the photometric sample. *Upper Panel:* We plot the observed |RM| in rad m^{-2} versus the weighted median impact parameter in kpc from the photometric catalog provided by (Hatfield et al., 2022) within an impact parameter of 133 kpc around each host for the COSMOS field. The green bar indicates a bin of individual data points with the blue line being the error bar of the bin. The individual data points are color-coded with respect to the total number of intervenors to each host. *Lower Panel:* The corresponding plot for the *XMM*-LSS field.

Table 2.2 This table lists the properties of the photometric galaxy catalog from Hatfield et al. (2022) and the median properties of the intervenors we find to the host sample. N_{host} are the total numbers of host galaxies from the MIGHTEE sample, $N_{\mathrm{photometric}}$ are the total numbers of galaxies in the photometric catalog for each field, $\langle N_{\mathrm{int}} \rangle$ is the median number of intervenors for each host, $\langle z_{\mathrm{phot,int}} \rangle$ is the median redshift of the intervenors, $\langle M_{g,\mathrm{int}} \rangle$ is the median M_g magnitude of the intervenors, and $\langle m_{\mathrm{int}} \rangle$ and $\langle SFR_{\mathrm{int}} \rangle$ are the median mass and star-formation rate of all intervenors in $\log_{10}(M_\odot)$ and $\log_{10}(M_\odot/\mathrm{yr})$ respectively.

Field	N_{host}	$N_{\mathrm{photometric}}$	$\langle N_{\mathrm{int}} \rangle$	$\langle z_{\mathrm{phot,int}} \rangle$	$\langle M_{g,\mathrm{int}} \rangle$ (mag)	$\langle m_{\mathrm{int}} \rangle$ $\log_{10}(M_\odot)$	$\langle SFR_{\mathrm{int}} \rangle$ $\log_{10}(M_\odot/\mathrm{yr})$
COSMOS	111	125,676	20	0.26	-14.8	8.1	-10.1
XMM-LSS	243	384,354	18	0.22	-15.5	7.8	-12.2

for intervenors with $M_u < -22\,\mathrm{mag}$. Thus, we only select massive galaxies with a denser CGM at a fixed distance. In addition, these galaxies are assumed to have higher star formation rates and therefore higher RM since star formation can drive magnetized outflows on galactic scales (Basu et al., 2018; Wiener et al., 2017). Our results confirm this assumption. The *XMM*-LSS sample is more inhomogenous than the COSMOS sample because of the wider redshift range and hence any excess at small impact parameters may be less obvious. The redshift-corrected excess from the combined samples is $3.0 \pm 1.2\,\mathrm{rad\,m^{-2}}$, which is significant at 2.5σ.

The increase towards small impact parameters of the |RM| is consistent with previous results suggesting the presence of significant magnetic fields in and around galaxies at distances of several tens of kpc (Bernet et al., 2012, 2013, 2008). However, we find that our results are lower than found in some previous work. Farnes et al. (2014) found an excess in |RM| of $24 \pm 6\,\mathrm{rad\,m^{-2}}$ in Mg II absorbers and Bernet et al. (2008) found an excess of $140\,\mathrm{rad\,m^{-2}}$. However, more recently, Heesen et al. (2023) used LOFAR observations to investigate a sample of nearby galaxies and found an excess in |RM| of $3.7\,\mathrm{rad\,m^{-2}}$ with an uncertainty between $\pm0.9\,\mathrm{rad\,m^{-2}}$ and $\pm1.3\,\mathrm{rad\,m^{-2}}$ corresponding to a significance of 2.8σ–4.1σ which is in agreement with our results. We note that Heesen et al. (2023) detected the excess of |RM| only for galaxies along the minor axis of inclined galaxies. For our samples at much higher redshifts, we cannot test this since we have no information about the orientation or inclination. Our data leads to a significance level of 2.5σ for the combination of both fields.

From our data, we can estimate the number of detections that we would need to get to a more reliable 3σ significance detection level. As σ scales with $\sqrt{n}$ and with given $n_{2.5\sigma} = 125$ (current combined sample size) we estimate the sample size that we would need for a 3σ detection to $n_{3\sigma} = 180$.

Another possibility to increase the significance of the detection that would not need as many new detections, would be to build a cleaner sample of hosts. For example, if the background hosts consisted of AGN in clusters then these hosts would have a larger intrinsic scatter in |RM| compared to hosts in poor group or isolated environments. Ideally, the background sources would only consist of AGN with a minimal contribution to the overall |RM| scatter. Alternatively, a weighting scheme could be introduced in order to account for the different underlying populations (Rudnick, 2019).

We do not find a connection between redshift and |RM|. As the *XMM*-LSS sample has a much higher redshift range ($0.06 < z < 1.09$) than the COSMOS sample ($0.25 < z < 0.46$), the trend of the *XMM*-LSS sample provides an indication over a wider redshift range. However, the wide redshift range of the *XMM*-LSS sample and explicitly high redshift detections lead to the fact that more intervening material occurs along the line of sight and the sample becomes more scrambled. In contrast, the smaller redshift range of the COSMOS sample leads to a more homogeneous sample so the results derived from this sample has more significance compared to the more heterogenous *XMM*-LSS sample. The correlation between redshift and |RM| derived from the COSMOS field is not significant and more data are needed. We note that there are two outliers showing high |RM| and high redshift. To test if the positive correlation is only due to those outliers, we mask these two outliers and compute the correlation again. As a result, we still detect a positive trend but with a shallower slope.

Previous work found contradictory results. Work by Kronberg & Perry (1982); Welter et al. (1984) and Kronberg et al. (2008) have found an increased |RM| at higher redshifts. More recent work by Bernet et al. (2012); Hammond et al. (2012) and Pshirkov et al. (2016) did not find any significant evidence for a correlation between |RM| and redshift. We note that the studies that find a positive correlation between |RM| and redshift have been carried out before the release of the re-analyzed NRAO VLA Sky Survey (NVSS) RM catalog (Oppermann et al., 2015; Taylor et al., 2009). The more recent work that does not find a correlation between |RM| and redshift used the improved NVSS RM catalog.

In order to determine the magnitude of the magnetic field strength around galaxies, we use eq. (2.3). Assuming an electron density of $n_e \approx 10^{-4}\,\mathrm{cm}^{-3}$ and a line-of-sight length of $\approx 100\,\mathrm{kpc}$ we estimate a magnetic field strength of $B \approx 0.48\,\mu\mathrm{G}$ for the redshift corrected and combined sample. We note that this result is only a lower limit because the magnetic field strength may be amplified as magnetic field reversals can lower the RM.

The magnetic field strength in the discs of galaxies is usually found to be of order 10 - 15 μG (Pakmor et al., 2017). Observations of nearby galaxies show that the magnetic field can be described by $B = B_0 \exp(-r/r_0)$ (Beck, 2015). Assuming magnetic fields to go down following the above relation from the galactic disk to CGM, and $B_0 \approx 10\,\mu\mathrm{G}$ and $r_0 \approx 10$ kpc we derive $B = 0.45\,\mu\mathrm{G}$ at a distance of 100 kpc from the galaxies center. Simulations suggest similar values for the magnetic field strength around galaxies (Pakmor et al., 2020). Heesen et al. (2023) found a magnetic field strength of $\approx 0.50\,\mu\mathrm{G}$ for a sample of nearby galaxies. This agrees with our estimate which is derived from a sample of galaxies at higher z and with higher SFR.

2.5.2 The photometric sample

In the preceding analysis of the spectroscopic catalog, we assumed that the contribution to the RM is dominated by one massive and bright intervenor with the smallest impact parameter to the LOS to the host. However, our host are located at high redshifts, resulting in a large number of intervening galaxies. Not all galaxies contribute equally to the observed RM. We expect that those with higher masses or higher star-formation rates tend to exhibit stronger magnetic fields in the CGM. Previous studies that examined the RM around galaxies neglected the effect of multiple intervenors.

Using the photometric catalog from (Hatfield et al., 2022) allows us to assess the effect of multiple intervenors on the RM. In addition, by implementing various weighting schemes, we can investigate if galaxies with higher masses or star-formation rates have a greater influence on the RM. In this work, we introduced a weighting scheme that takes into account the star-formation rate of each galaxy. Our initial hypothesis suggests that the RM generated by intervenors is higher when they exhibit higher star-formation rates and if they are located at smaller impact parameters. While our analysis provides some preliminary evidence to support this assumption, we cannot draw any definitive conclusions due to the limitations of the available data. The spectroscopic sample indicates that an excess of |RM| is detected at smaller impact parameters, which fall within the size range of the circumgalactic medium (CGM) when considering only the most luminous galaxy. However, using the the photometric sample, we observe only a small trend between the average impact parameter and the |RM|. As a result, we infer that the most luminous galaxy is most likely the primary contributor to the overall RM.

2.6 Conclusions

Magnetic fields around galaxies are important to understand galaxy evolution as they regulate the transport of cosmic rays. Direct observations of the CGM are limited to a few nearby sources as the CGM is very tenuous. Indirect methods such as transverse absorption-line studies are therefore a powerful tool to investigate the physical conditions in the CGM such as the metallicity, temperature and gas density and also the magnetic field strength.

We used MIGHTEE-POL data to measure the RM around foreground star-forming galaxies to investigate the strength of magnetic fields in the CGM. We used catalogs of star-forming and blue cloud galaxies to measure the rotation measure of MIGHTEE-POL sources as a function of the impact parameter from the intervening galaxy and derived the magnetic field strength of the CGM. Also we investigated a possible connection between the |RM| and the redshift. In addition, we studied the impact of all intervenors along the line of sight using the photometric catalogs from (Hatfield et al., 2022) with respect to the mean impact parameter. To account for the impact of mass and star-formation rate of the individual intervenors we introduced a weighting scheme.

In summary, we can draw the following conclusions:

1. For a sample with high star-forming galaxies in the MIGHTEE-POL survey by MeerKAT in the *XMM*-LSS and COSMOS fields we find an excess of the RM for impact parameters of less than 133 kpc around bright spectroscopic galaxies with a significance of 2.5σ. We attribute this excess to coherent magnetic fields in the CGM. The excess RM is in agreement with recent work of Heesen et al. (2023) for nearby galaxies, but lower than previous work (Bernet et al., 2013; Farnes et al., 2014). We do not subtract the contribution of the Galactic RM.

2. For a complete sample including galaxies down to magnitudes of $M_g \approx -13.8$, we do not find any RM excess which suggests that only bright, star-forming galaxies with impact parameters less than 130 kpc significantly contribute to the RM of the background radio source.

3. Making rough assumptions on the electron density in the CGM, we estimate the magnetic field strength to be of the order of $B = 0.5\,\mu$G which is in agreement with observations and simulations.

4. We do not find a correlation between the RM of intervening galaxies and their redshift.

5. Using the photometric catalog we do not find a correlation between the total number of intervenors, $\mathrm{N_{int}}$, to the total |RM|. Even introducing a weighting scheme that takes into account the star-formation rate does not lead to an |RM| excess in the innermost bin.

Our results suggest that there is a correlation between the impact parameter and the rotation measure which indicates the presence of intervening magnetic fields in the CGM. We find that the |RM| becomes smaller with higher impact parameters for both our samples. Future studies with larger catalogs of background quasars and more accurate RM measurements enable extensive and more detailed studies of the magnetized CGM.

Below we summarize the main caveats of our work:

1. Selection function of foreground galaxies: The galaxy catalogs that are used are complete in terms of magnitude but not volume-limited. Even though the RM from galaxies at higher z contribute less, there may be still undetected intervening galaxies. Certainly for the *XMM*-LSS field the coverage is not uniform across the field.
2. The total RM is an integral along the line of sight and we cannot differentiate between contributions from the host, other intervenors or Galactic contributions. Advanced techniques such as rotations measure synthesis can be useful here.

In our work we make use of early-release data from MIGHTEE-POL which is characterized by a relatively high level of uncertainty. Still we could extract statistically significant signals from this early-release data. MIGHTEE serves as a pilot study for surveys with the forthcoming Square Kilometre Array (SKA). Therefore, our results can soon be tested with much larger datasets. The polarization Sky Survey of the Universe's Magnetism (POSSUM) carried out by ASKAP, for example, will map a large area of the sky and it is expected to detect millions of rotations measures. Larger catalogs will yield a more robust detection of magnetic fields in the CGM. Prospects for future work also include the study of the CGM of quiescent galaxies, where synchrotron emission due to star formation activity is absent.

3 The Life of Radio Galaxies in Clusters: Joint Surveys by eROSITA and ASKAP

This chapter is based on the published article "Central radio galaxies in galaxy clusters: Joint surveys by eROSITA and ASKAP", K. Böckmann, M. Brüggen, B. Koribalski, A. Veronica et al., 2023, A&A, Volume 677, A188

3.1 Introduction

The eROSITA telescope onboard the Spectrum-Roentgen-Gamma (SRG) mission has finished the first eROSITA All-Sky Survey (eRASS:1), and detected $\sim 10^4$ galaxy clusters in the western Galactic hemisphere. In the radio band, the ASKAP telescope finished its pilot 1 phase of the project 'Evolutionary Map of the Universe' (EMU) with 220.000 sources in a 270 deg^2 field overlapping with eRASS:1. These two surveys are used to study radio-mode AGN in clusters. In order to understand the efficiency of radio-mode feedback at the centres of galaxy clusters, we relate the radio properties of brightest cluster galaxies (BCG) to the X-ray properties of the host clusters. We identify the central radio sources in eRASS:1 clusters or calculate corresponding upper limits on the radio luminosity. Then, we derive relations between the X-ray properties of the clusters and the radio properties of the corresponding central radio source. In total we investigate a sample of 75 clusters. We find a statistically significant between the X-ray luminosity of the cluster and the 944 MHz radio luminosity of the corresponding central radio galaxy. There is also a positive trend between the radio power and the largest linear size (LLS) of the radio source. The density and the LLS do not show any correlation. We find that in high luminosity clusters with $L_{\mathrm{X}} > 10^{43}$ erg s^{-1} the kinetic luminosity of the radio jets is not longer correlated with the X-ray luminosity and discuss various reasons. We find an anti-correlation between the central cooling time t_{cool} and the radio luminosity L_{R} indicating a need for more powerful AGN in clusters with short central cooling times.

3.2 Data

3.2.1 eRASS:1 cluster catalog

The extended ROentgen Survey with an Imaging Telescope Array (eROSITA) onboard the Spectrum-Roentgen-Gamma (SRG) mission was launched in July 2019 (Predehl et al., 2021). eROSITA will perform all-sky surveys (eRASS) with a significantly improved sensitivity than the ROSAT all-sky survey. In contrast to X-ray telescopes such as XMM-Newton or Chandra

which are used for long exposure pointed observations of single targets eROSITA allows unique survey science capabilities by scanning large areas of the X-ray sky fast and efficiently. The eRASS survey is detecting a large number of previously non-detected galaxy clusters and will extend existing galaxy clusters catalogs substantially (Liu et al., 2022; Merloni et al., 2012).
eROSITA is operating in the 0.2 - 10 keV energy range onboard the Spectrum-Roentgen-Gamma (SRG) mission (Sunyaev et al., 2021) (see the instrument paper by Predehl et al. (2021)). It has an effective area of 1365cm^2 and a spectral resolution of 80 eV FWHM at 1 keV and an angular survey resolution of 26 arc seconds. eROSITAs main task is to scan the whole X-ray sky with a final depth of about 1.3ks. The sensitivity will therefore be improved by at least a factor of 20 compared to the only previous X-ray all-sky survey performed by ROSAT 30 years ago. The main task of eROSITA is the study of evolution and nature of dark energy. It is expected to detect about 10^5 galaxy clusters and more than one million AGN (Merloni et al., 2020; Merloni et al., 2012).
The first all-sky survey eRASS:1 imaged the whole X-ray sky over the course of 182 days from December 2019 to June 2020 with an average effective exposure of 150-200s. About 10^4 clusters are detected as extended sources in eRASS:1, using the source detection algorithm in eROSITA Standard Analysis Software System (eSASS, (Brunner et al., 2022)). Redshifts are determined using data from the Legacy Survey. In this work we make use of the cluster catalog resulting from the first all-sky scan (eRASS:1) which was finished in 2020 (Bulbul et al. (2023, in prep.)). We study the central radio galaxies in the cluster centers with 944 MHz radio data from the survey Evolutionary Map of the Universe (EMU) performed by the Australian Square Kilometre Array Pathfinder (ASKAP) (Norris et al., 2021). The X-ray luminosity that is used throughout this paper is is calculated in the 0.2-2.3 keV band.

3.2.2 EMU Pilot field

The Australian Square Kilometer Array Pathfinder (ASKAP) is a radio telescope in the Murchison region of Western Australia (Hotan et al., 2021; Johnston et al., 2008; Koribalski, 2022). ASKAP is a radio interferometer consisting of 36 12-meter dish antennas, spread out in two dimensions with baselines up to 6 km. Each antenna is equipped with a wide-field Phased Array Feed (PAFs) used to form 36 beams, ie. each pointing reaches a field of view of ∼30 deg^2.
The Evolutionary Map of the Universe (EMU) is a survey project using the ASKAP telescope. In July to August 2019 EMU observed a pilot field for 100 hours, to test the planned observing mode for the full EMU survey. The EMU pilot survey maps 270 deg^2 of sky with a RA from 305° to 335° and DEC from -62° to -48° centered at 944 MHz down to an RMS of about 25-30 μJy/beam at an angular resolution of 10 - 18 arcsec, see Norris et al. (2011, 2021) for further details on the survey.
As images with large fields of view such as the EMU pilot field yields a large number of detected astronomical sources an automated source detection technique which measures the properties of the sources is essential. The most common approach is to identify local peaks of emission above some threshold, and fitting two-dimensional Gaussians. As radio surveys have become deeper and wider in recent years, the number of sources in catalogs has grown enormously, such that manual source finding and identification is not feasible anymore. An ASKAP/EMU source finding challenge by Hopkins et al. (2015) that was carried out before

the start of EMU tested several approaches for an automatic source detection. Source finding and cataloging is the last step in the ASKAP data processing pipeline (ASKAPsoft, e.g., Guzman et al. (2019); Wieringa et al. (2020)) for all surveys such as continuum, HI emission / absorption and polarisation, carried out using Selavy (Whiting et al., 2017). More powerful source finders will likely be applied by each team to their specific projects.
The image data was first processed by the ASKAPsoft pipeline and the subsequent source extraction of the final calibrated image used the software tool Selavy. This tool identifies radio islands with emissions higher than five times the local RMS and fits Gaussians to peaks of emission within the islands. The peak as well as the integrated radio flux of each island is computed and stored in a FITS catalog containing a total number of ∼220.000 radio islands of which ∼180.000 are single component sources. In comparison with previous surveys, EMU explores a novel region of parameter space because of ASKAPs wide field of view combined with high angular resolution as well good sensitivity. For a summary of the EMU pilot survey specifications see Table 3.1.

Table 3.1 EMU Pilot Survey Specifications

Area of survey	270 deg^2
Synthesised beamwidth	13 arcsec ×11 arcsec FWHM
Frequency range	800 – 1088 MHz
RMS sensitivity	25–35 μJy / beam
Total integration time	10 × 10 hours
Number of sources	∼ 200,000

3.2.3 Construction of the sample

The EMU pilot field is fully covered by eRASS:1. Therefore, we create a cluster sample with all eRASS:1 detected clusters within the EMU field, resulting in a total number of 75 confirmed eRASS:1 clusters. Each cluster is visually inspected in the EMU image as well as in WISE and in legacy optical data to identify the BCG of each cluster and the corresponding radio source to the BCG.
We identify the BCG and the corresponding central radio island for each cluster. For 64 from the 75 clusters we find a central radio source within a distance of $\sim \theta$ of the BCG, where θ = 18 arcsec which is the synthesized beam of the radio observation. For the remaining 11 clusters we set an upper limit of 3σ, where σ is the rms noise of the EMU image of rms = 35 μJy. Magliocchetti & Brüggen (2007) examined radio emission of 550 X-ray selected clusters finding that only 27 % host a central radio source. However, the difference in these results can be attributed to the depth of the respective datasets as the depth of the used survey reaches only 3 mJy whereas the EMU has a depth of 35 μJy.

Visual inspection of each source is the most reliable way to minimize the number of false identifications, as at all separations some radio identifications selected by the position offset alone will be random coincidences (Condon et al., 2002; Mauch & Sadler, 2007; Sadler et al., 2002). Nonetheless, we still expect a fraction of false associations that we describe via the

P-statistics. This quantifies the probability that a radio source will have a chance coincidence within a distance θ from a certain point, here our BCG candidate. It is given by

$$P(\theta) = 1 - e^{n\pi^2}, \tag{3.1}$$

with n denoting the number density of radio sources (Scott et al., 2008). If we assume a uniform distribution of radio sources of $n = 815$ deg^{-2}, which is the average source density from an ASKAP observation, we get $P(18\text{arcsec}) = 6.6$ per cent contamination. So for the 64 clusters with a radio match we expect $\sim$3 false associations.

3.2.4 Properties of the sample

The upper panel of Fig. 3.1 shows a histogram of the redshift distribution of our cluster sample. The majority of the clusters lie within a redshift range of $0.1 < z < 0.7$ with two outliers above $z > 0.8$. We use the best available redshift provided from the eRASS:1 cluster catalog which can be spectroscopic or photometric redshifts. The lower panel of Fig. 3.1 shows the mass distribution. The mass is estimated via the $\mathrm{L_X}$ - $\mathrm{M_{500}}$ correlation by Chiu et al. (2022). The masses of most the clusters lie within 1 - 12 $\cdot$ 10^{14} $\mathrm{M_\odot}$.

The luminosity of all radio sources was calculated including the following k-correction:

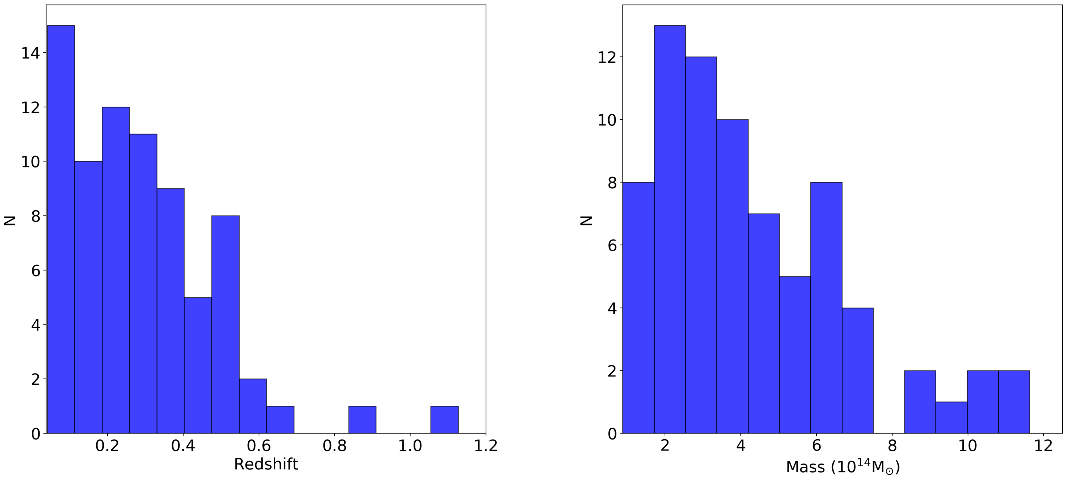

Figure 3.1 *Left Panel:* Histogram showing the redshift distribution of the sample. *Right Panel:* Mass distribution of $\mathrm{M_{500}}$ of the cluster sample. The mass was estimated via the $\mathrm{L_X}$ - $\mathrm{M_{500}}$ correlation from (Chiu et al., 2022).

$$L_{\mathrm{Radio}} = 4\pi D_{\mathrm{L}}^2 S_{\mathrm{Radio}} (1+z)^{\alpha-1}. \tag{3.2}$$

D_{L} is the luminosity distance at redshift z and α is the spectral index assumed 0.6. Fig. 3.2 shows the radio luminosity distribution at 944 MHz versus the redshift of the sample. We also plot the theoretical flux cut in Fig. 3.2.

Next, we calculate the largest linear size (LLS) for each radio source. The LLS is defined as the linear size of the major axis of a source and is displayed in Fig. 3.3. The LLS is calculated within a 3σ isophote. When the radio source is not resolved, which is the case for 6 clusters, we treat the source as an upper limit with a LLS corresponding to the beam size. The LLS varies from ~ 50 to ~ 250 kpc. We also show the offset from each BCG to the X-ray center of the corresponding cluster. The majority of BCGs are found within 200 kpc around the X-ray peak of the cluster.

In Fig. 3.4 we show the radio and X-ray luminosity distribution functions of the cluster sample at 944 MHz and 0.5 - 2.0 keV, respectively. The overall radio luminosities lie within a range of $\sim 10^{29}$ and $\sim 10^{33}$ erg s^{-1} Hz^{-1}. The X-ray luminosities exhibit values from $\sim 10^{43}$ to $\sim 10^{45}$ erg s^{-1}.

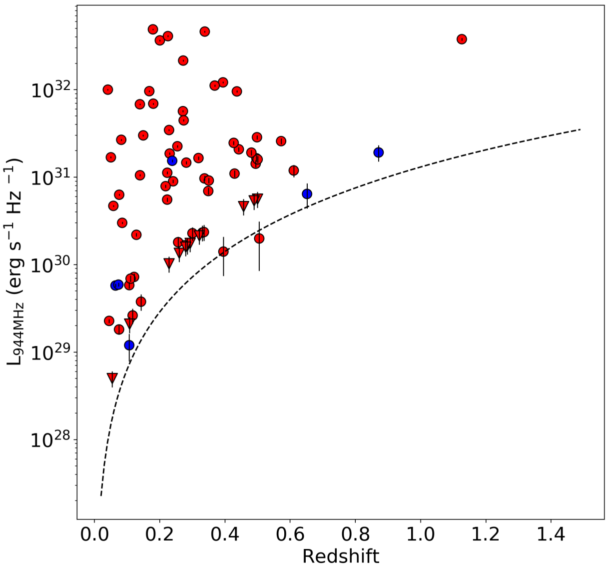

Figure 3.2 944 MHz radio luminosity versus redshift. The dashed line represents the theoretical flux limit for point sources. The circles represent the clusters with a detected central radio source whereas the triangles represent the upper limits. The red color represent resolved sources while the blue points represent point sources.

3.2.5 WISE colors

One approach to identify AGN is a mid-infrared color criterion which is deduced from the separation between the power-law AGN spectrum and the black-body stellar spectrum of galaxies which has its peak at a rest-frame of 1.6 μm (Assef et al., 2010). We apply this technique to our sample by using the Wide-field Infrared Survey Explorer (WISE) survey

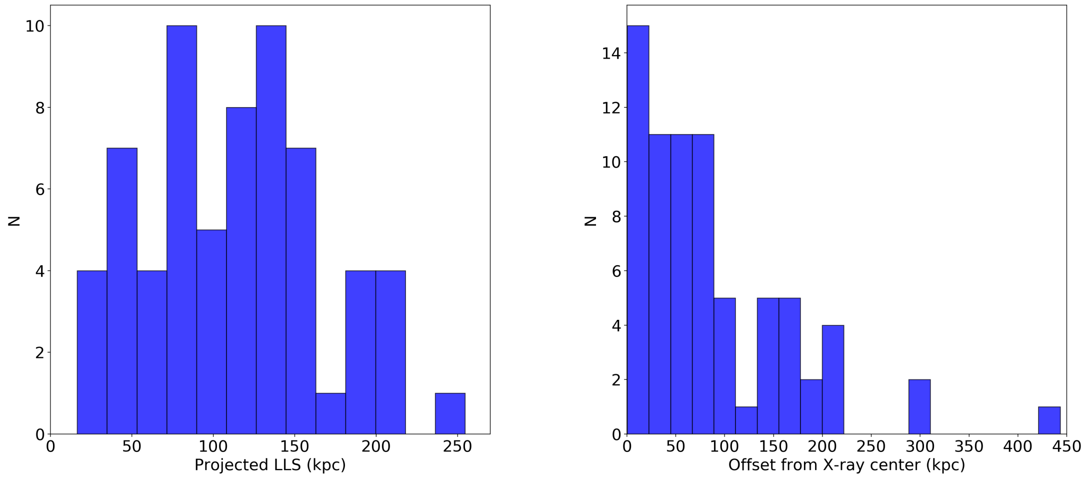

Figure 3.3 *Left Panel:* Histogram showing LLS in kpc of each extended radio source. *Right Panel:* Histogram showing the BCG offsets from the X-ray emission peak of the cluster.

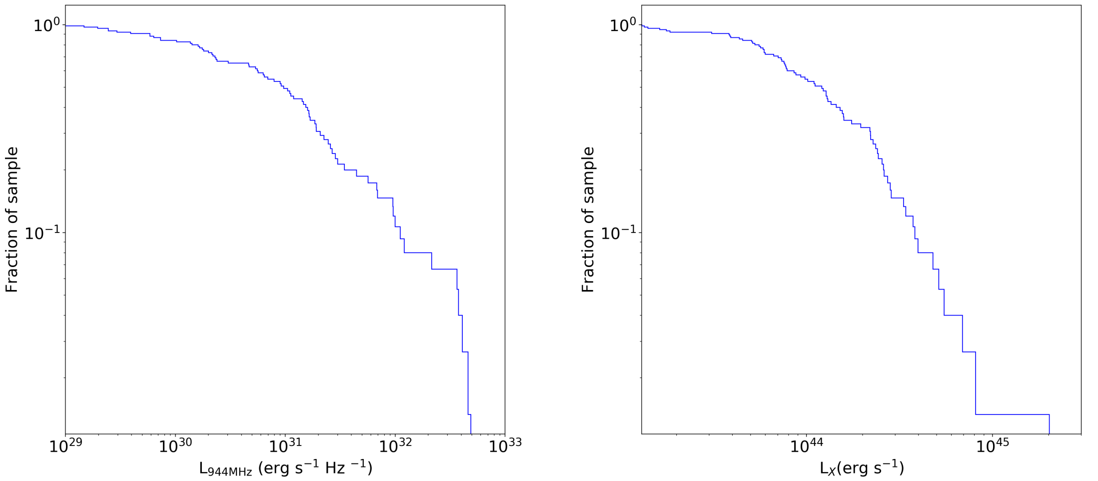

Figure 3.4 *Left Panel:* 944 MHz radio luminosity distribution for the cluster sample. *Right Panel:* X-ray luminosity distribution among the sample for the 0.5-2.0 keV band.

which mapped the whole sky in 4 different bands: 3.4, 4.6, 12 and 22 μm, referred to as W1, W2, W3 and W4 respectively (Wright et al., 2010). The color criterion used is the difference of magnitudes of W1-W2 (i.e. 3.4 - 4.6). For our sample the W1 and W2 magnitudes and the W1-W2 criterion is shown in Fig. 3.5. We can see that our median value for the color criterion is $\mu \approx 0.152$ with a corresponding interquartile range of $\sigma \approx 0.155$. This is in contrast to Stern et al. (2012) who find a value of W1-W2 ≥ 0.8 for AGN selection and Assef et al. (2018) who find a value of W1-W2 ≥ 0.77. However, current work of LaMassa et al. (2019) and Mountrichas et al. (2019) on AGN in stripe 82 show that 2/3 of X-ray detected AGN are not identified via the mid-infrared criterion. Especially AGN with luminosities between $10^{42.5} < L_X < 10^{44}$ erg s^{-1} are non-detectable by the WISE criterion and show bluer W1-W2 colors. In this population the AGN does not seem to dominate the mid-infrared emission and therefore the color criterion is not applicable to our sample where most of our objects meet this luminosity.

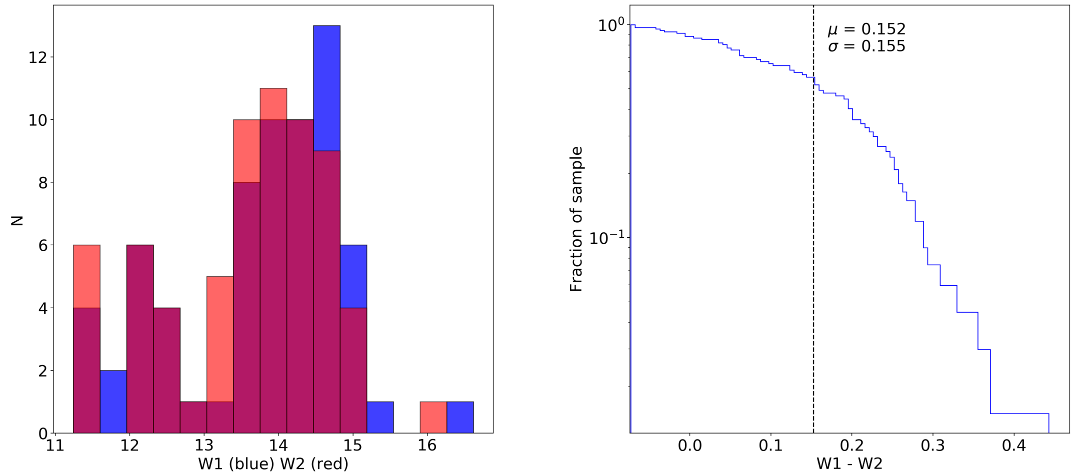

Figure 3.5 *Left Panel:* Histogram showing the magnitude distribution of WISE colors W1 (blue) and W2 (red) in Vega magnitudes. *Right Panel:* Distribution for W1 - W2.

3.3 Analysis and Discussion

3.3.1 Linear Size of the BCGs

Radio galaxies appear in a wide range of sizes and shapes such as giant radio galaxies with largest linear sizes (LLS) of more than 0.7 Mpc which were, for example, examined in Dabhade et al. (2020) and small radio galaxies (e. g. Baldi et al. (2015)). Hardcastle et al. (2019) examined the relation between radio power and the linear size of a sample of 23344 radio-loud AGN which is also referred to as the $P - D$ diagram (e.g. Turner et al. (2017)). This diagram and the location of each source on it is an indicator for its initial conditions and its evolutionary state. The tracks of a source are associated with different phases in the evolution of the source. Objects with specific properties follow tracks on the plane that are mainly defined by the physics of the object. Remnant sources with switched-off jets describe a different set of tracks (Hardcastle, 2018). However, also the environment can have an impact on the $P - D$ track. Sources in denser environments typically appear brighter than in a more dilute environments (Turner & Shabala, 2015; Yates-Jones et al., 2022).

We measure the angular sizes of the sources and then convert them to linear sizes using their redshift. The errors on the angular sizes are taken to be equal to the synthesized beam. The

$P - D$ diagram for our sample is shown in Fig. 3.6. Pasini et al. (2022) (P22, hereafter) examined a sample of 542 galaxy clusters and groups that were detected in the early performance verification phase (eFEDS) of eROSITA and compared them to the emission of the central radio galaxies detected with LOFAR. In Fig. 3.6 we compare the projected sizes of P22 to our data. To this end we re-scale the 944 MHz luminosity to a luminosity at the LOFAR HBA central frequency of 144 MHz using a spectral index $\alpha = 0.6$. We see that our sample of eRASS:1 clusters extends the $P - D$ diagram to lower LLS values with the luminosities being comparable to the luminosities $\mathrm{L}_{144\mathrm{MHz}}$ examined in P22, namely between $\sim 10^{23}$and$\sim 10^{26}$erg $\mathrm{s}^{-1}\mathrm{Hz}^{-1}$.

We see that the EMU sample reaches similar radio powers as the LOFAR data which is due to the fact that EMU reaches a depth of 25–30 μJy/beam at 944 MHz which responds to a depth of 110 μJy/beam at the LOFAR frequency of 144 MHz while the LOFAR observation of the eFEDS field reaches $\sim$ 100 μJy/beam. Also we note that the resolution of ASKAP is $\sim$ 18 arcsec in contrast to LOFAR reaching $\sim$ 6 arcsec (Shimwell et al., 2017, 2019).

Interpretation of the $P - D$ diagram should be handled with care because several facts have to be taken into account. On the one hand the environment and location within the cluster of the radio galaxy has an impact on the position and track on the diagram. Also we only observe the projected LLS and we did not account for selection effect against large, low-luminosity sources (Shabala et al., 2008; Turner & Shabala, 2015). In addition, the redshift dependence might affect the $P - D$ diagram and its slope. We do not take into account the individual redshifts which may result in a bias that distorts the true correlation between LLS and radio power. Different redshifts correspond to different cosmic epochs, where the properties and evolutionary stages of radio galaxies can vary. Without correcting for redshift, objects at different redshifts may not be directly comparable. However, we clearly see a positive correlation between the LLS and the radio luminosity, larger radio galaxies usually host larger radio luminosities.

In Fig. 3.7 we show the projected LLS of the versus 944 MHz radio power of the EMU radio galaxies. As previously observed, there is a positive correlation between LLS and luminosity, with larger radio galaxies being more powerful (Kolokythas et al., 2018; Owen et al., 2002; Pasini et al., 2022). The mean value of the LLS is 130 kpc with a standard deviation of 74 kpc. We calculate the relation between the radio power and the LLS to be $\log P_{\mathrm{R}} = (3.12 \pm 0.1) \cdot \log \mathrm{LLS} - (17.33 \pm 0.22)$. Nontheless, we note that we also expect a diagonal sensitivity limit as for a given luminosity of an extended source at a given redshift, larger sources are harder to detect as they have a lower surface brightness (Shabala et al., 2008). For our sample the theoretical cut-off limit do not play a role as it is four orders of magnitudes fainter that our measurements.

We also plot the projected LLS versus the central density of the ICM in Fig. 3.7 and we conclude that there is no correlation between these two observables. However, color-coding the individual data points by the radio luminosity reveals that sources with a low central density and small LLS tend to exibit low radio luminosities. The lower central ICM density could imply a lower pressure in the radio lobes leading to lower synchrotron emissivities, while smaller sources also favour smaller luminosities.

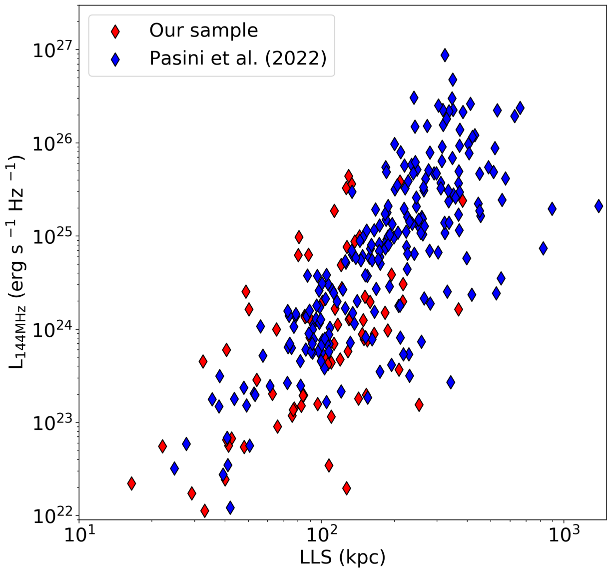

Figure 3.6 Projected LLS versus the 144 MHz luminosity from P21 and our sample. We re-scaled the luminosity from 944 MHz to 144 MHz using the spectral index $\alpha = 0.6$.

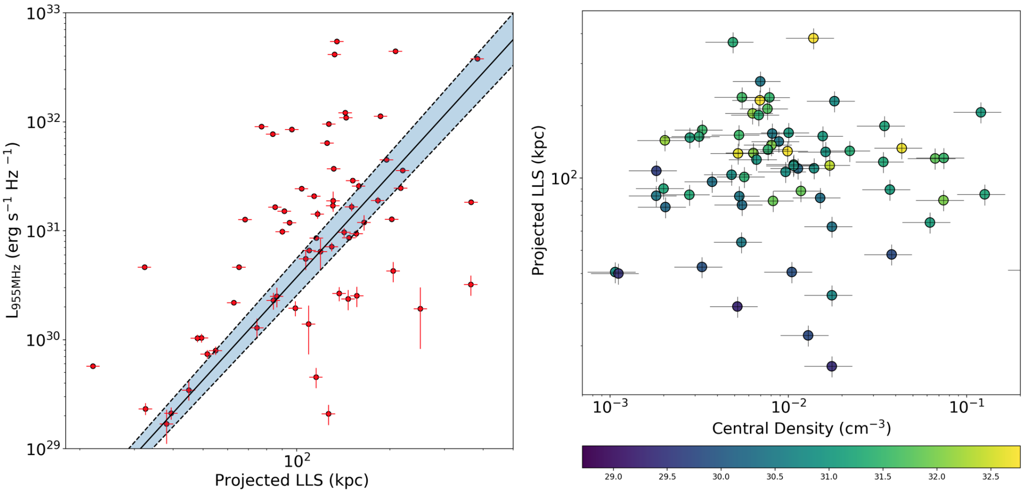

Figure 3.7 *Left Panel:* Projected LLS versus 944 MHz radio power of the EMU radio galaxies. The black line represents the best fit with the blue region inside the dashed lines being the errorband: $\log P_{\mathrm{R}} = (3.12 \pm 0.10) \cdot \log \mathrm{LLS} + (17.33 \pm 0.22)$. *Right Panel:* Projected LLS of the radio source versus the central density of the cluster. The data points are color-coded with the logarithmic radio luminosity in erg s $^{-1}$ Hz $^{-1}$.

3.3.2 BCG Offset

In order to examine the BCG offset of each cluster, we calculate the physical distance between the X-ray center given in the eRASS:1 cluster catalog and the optical identified BCG. The result is shown in the lower panel of Fig. 3.3. The majority of BCGs are found within a radius of $\sim$ 100 kpc around the cluster center which has been defined by the X-ray peak. This is consistent with the assumption of AGN feedback since the gas cooling out of the hot ICM can feed the central SMBH, while outer galaxies need to rely on more episodic triggers. Pasini et al. (2021) fulfilled a phase-space analysis by comparing the cluster-centric velocity with the cluster-centric offset of the hosted galaxies to investigate the assembly and accretion history of these objects. Their analysis suggests that powerful radio galaxies are always located close to the cluster center. The interpretation was that the cooling ICM can feed the AGN if the galaxy lies close to the cluster density peak, where the cooling is more efficient. Nonetheless, galaxies located in cluster outskirts can also host radio AGN, and triggers such as mergers or interactions might be important (Marshall et al., 2018). Small BCG offsets of less than 100 kpc are expected and found in most relaxed clusters as minor mergers can produce sloshing and displace the X-ray emission peak from the BCG (Hamer et al., 2016; Ubertosi et al., 2021). Larger offsets are usually an indication for major merger events and therefore strongly disturbed clusters (De Propris et al., 2021; Hudson et al., 2010; Ota et al., 2023; Rossetti et al., 2016; Seppi et al., 2023). In the next section, we compare the BCG offsets to the dynamical state of the clusters.

3.3.3 Morphological Parameters

X-ray observations can be used to compute a quantitative measure of the dynamical status of a cluster. Different morphological parameters to quantify the dynamical status of a cluster have been described in literature, here we focus on the concentration parameter c. The concentration parameter is the ratio of X-ray flux within a radius of 100 kpc around the cluster center over the X-ray flux within a radius of 500 kpc (Santos et al., 2008). It is defined as the ratio of the peak over the surface brightness S as

$$c \equiv \frac{S(r < 100\,\mathrm{kpc})}{S(r < 500\,\mathrm{kpc})}. \tag{3.3}$$

Clusters that have a compact core, which has not been disrupted by merger activity, have higher concentration parameters. Hence, disturbed systems yielding lower values for c. Previous work, e.g., by Bonafede et al. (2017); Cassano et al. (2010) have stated that considering the median value of $c = 0.2$ it is possible to distinguish between disturbed ($c < 0.2$) and more relaxed ($c > 0.2$) clusters. Fig. 3.8 shows the plot of the concentration parameter against the BCG offset. We clearly see that clusters that show a large offset from the BCG to the X-ray center have concentration parameters of $c < 0.2$ and can thus be classified as disturbed systems. There is clearly a link between the clusters' dynamical status to their BCG offsets, with larger offsets found in more disturbed systems.

Another commonly used morphological parameter is the power ratio P_3/P_0 Buote & Tsai (1995). However, the number of photons in the eRASS:1 data is too low to yield a reliable estimate for the parameter P_3/P_0. So we have to return to this in future work.

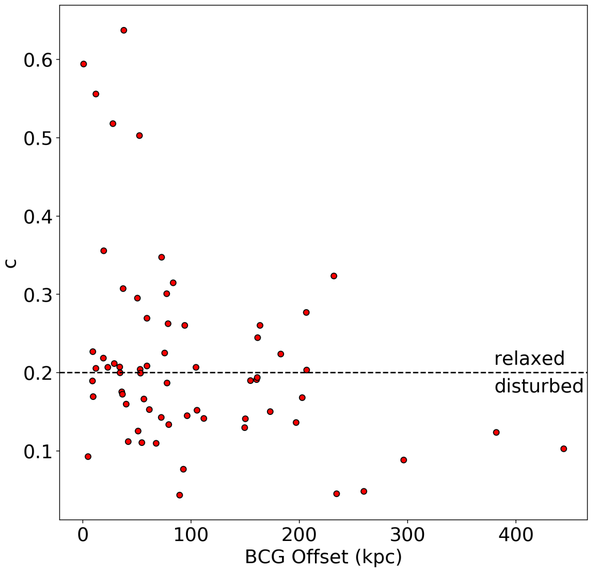

Figure 3.8 The concentration parameter plotted versus the BCG Offset. The median value of $c = 0.2$ subdivides the sample in relaxed and disturbed clusters.

3.3.4 Radio and X-ray luminosity correlation

In this subsection, we investigate how the radio luminosity of the BCG relates to the global X-ray properties of the host cluster. Fig. 3.9 shows the 944 MHz luminosity of the central radio galaxy versus the X-ray luminosity of the galaxy cluster in the 0.1-2.4 keV band with the colors displaying the redshift and the size of the points the LLS. There is a trend for more luminous radio galaxies to be hosted in more X-ray luminous clusters, albeit with significant scatter. Using the python package `hyperfit`[1] we calculate the correlation of the X-ray and radio luminosities (Robotham & Obreschkow, 2015). This package provides a method to fit a line to data allowing for both, intrinsic scatter and (potentially correlated) errors on all the input variables, here x and y for our 2D fit. We run this program on our data with a fully converged mcmc run. As a result we get: $\log L_\mathrm{R} = (0.89 \pm 0.04) \cdot \log L_\mathrm{X} - (8.52 \pm 1.44)$. The p-value of this fit equals to 0.05, therefore we consider this relation to be statistically significant.

We find that clusters that host radio sources with high radio luminosities ($> 5{\cdot}10^{31}\mathrm{ergs^{-1}Hz^{-1}}$) broaden the function and introduce a large scatter into the correlation. A similar correlation has been found by Hogan et al. (2015), even though they are not quantifying their results. Our results are also consistent with the best-fit relation found by Pasini et al. (2022) who find $\log L_\mathrm{R} = (0.84 \pm 0.09) \cdot \log L_\mathrm{X} - (6.46 \pm 4.07)$ and Pasini et al. (2020, 2021), see Table 3.2 for the corresponding relations. Although the results are in agreement we clearly see that our sample shows a lower scatter in the relation. One reason for this could be the large number of

---

[1] https://github.com/CullanHowlett/HyperFit

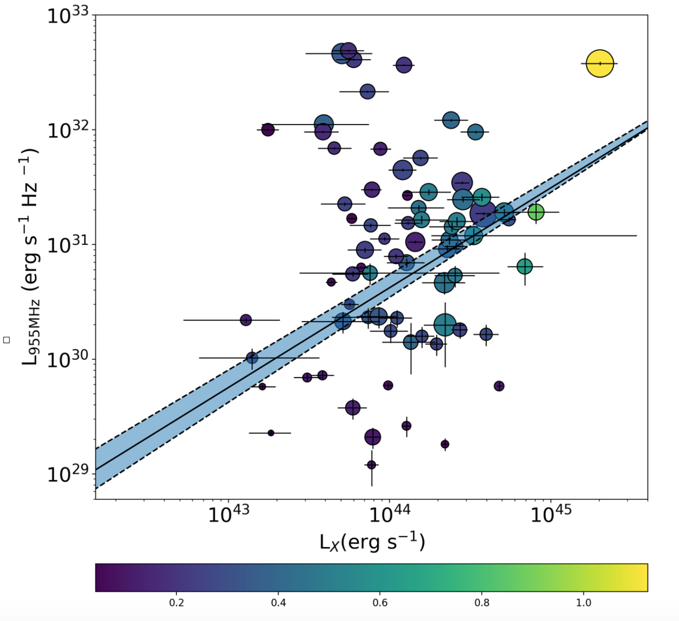

Figure 3.9 944 MHz luminosity of the central radio galaxy versus the X-ray luminosity of the galaxy cluster in the 0.1-2.4 keV band. Each point is colorized by the redshift and scaled by the LLS. The black line represents the best fit with the blue region inside the dashed lines the errorband: $\log L_{\mathrm{R}} = (0.89 \pm 0.04) \cdot \log L_{\mathrm{X}} - (8.52 \pm 1.44)$.

radio upper limits that were taken into account in former work which adds larger uncertainties. Generally, we would expect more scatter at lower frequencies as lower frequencies are emitted by electrons that are older.

Table 3.2 Overview of the X-ray/radio correlation found by other authors.

Author	#	z	Correlation
Mittal et al. (2009)	64	0.004 - 0.215	$\log L_{\mathrm{R}} = (1.38 \pm 0.16) \cdot \log L_{\mathrm{X}} - (1.52 \pm 0.3)$
Pasini et al. (2020)	247	0.08 - 1.75	$\log L_{\mathrm{R}} = (1.07 \pm 0.12) \cdot \log L_{\mathrm{X}} - (15.90 \pm 5.13)$
Pasini et al. (2021)	79	0.08 - 1.53	$\log L_{\mathrm{R}} = (0.94 \pm 0.43) \cdot \log L_{\mathrm{X}} - (9.53 \pm 18.19)$
Pasini et al. (2022)	542	0.1 - 1.3	$\log L_{\mathrm{R}} = (0.84 \pm 0.09) \cdot \log L_{\mathrm{X}} - (6.46 \pm 4.07)$
This work	75	$0.03 - 1.1$	$\log L_{\mathrm{R}} = (0.89 \pm 0.04) \cdot \log L_{\mathrm{X}} - (8.52 \pm 1.44)$

3.3.5 Jet mechanical powers

The radio lobes only radiate away a small fraction of the total power which is supplied to the lobes when the source is active. This small fraction of radiation is the radio luminosity which is only a fraction of the energy produced by the AGN through accretion of matter towards the black hole itself. A larger fraction of the power is, both, stored in the radio lobes and dissipated during the expansion of the jets into the ICM (Smolčić et al., 2017). A direct approach to calculate the mechanical power of a radio jet would be to derive it from the properties of the radio source in comparison with a radio source evolution model. In most cases this is not possible because of the unknown radio environment of the sources. Also, the luminosity evolves over the age of the sources (Hardcastle, 2018; Turner & Shabala, 2015; Yates-Jones et al., 2022). A common approach to overcome this problem is to estimate the jet mechanical energy by estimating it directly from the radio luminosity (Sabater et al., 2019).

This jet mechanical power to radio luminosity conversion is usually estimated from the cavities inflated by radio sources in the surrounding ICM as it is observed in X-ray images. The total mechanical energy is then calculated to $4pV$, with p the pressure of the surrounding medium and V the volume of the cavity. The factor of 4 arises if the enthalpy of the relativistic plasma in the radio lobes which is $3pV$ is added to the work performed to inflate the cavities which is pV. When also an estimate of the source age (e.g. via the buoyancy timescale of the cavity) is given, a lower limit of the mechanical power of the jet can be estimated, which is found to correlate with the observed radio luminosity (Bîrzan et al., 2008; Cavagnolo et al., 2010; Rafferty et al., 2006).

Another approach to relate the jet mechanical power to the radio luminosity is based on the synchrotron properties and therefore the composition of the jet plasma Willott et al. (1999). Heckman & Best (2014) found that both approaches provide consistent estimates of the jet mechanical powers and proposed a population-averaged conversion as:

$$P_{\mathrm{mech,cav}} = 2.8 \times 10^{37} \left(\frac{L_{1.4\mathrm{GHz}}}{10^{25}\mathrm{WHz}^{-1}} \right)^{0.68} \mathrm{W}.$$

Furthermore the kinetic luminosity at a rest-frame frequency of 1.4 GHz is described by

$$\log L_{\mathrm{kin,1.4GHz}} = 0.86 \log L_{1.4\mathrm{GHz}} + 14.08 + 1.5 \log f_W.$$

$L_{\mathrm{kin,1.4GHz}}$ describes the kinetic luminosity and $L_{1.4\mathrm{GHz}}$ the luminosity at 1.4 GHz. f_W is an uncertainty parameter that is estimated to be around 15 from observations (Smolčić et al., 2017). In order to determine the kinetic luminosity for our sample, we convert the radio power at 944 MHz to radio powers at a frequency of 1.4 GHz assuming a spectral index of $\alpha = 0.6$. We then compare our results to the X-ray luminosity of the host cluster. Again we make use of the package `hyperfit` to estimate our relation in log-log scale in the form:

$$Y = \alpha + \beta X + \varepsilon,$$

where α and β represent the intercept and slope and ε the intrinsic scatter. We find $\alpha = -3.81 \pm 1.01, \beta = 1.08 \pm 0.03$ and $\varepsilon = 0.91 \pm 0.61$, see Fig. 3.10. This is in rough agreement with values found by Pasini et al. (2022), who found $\alpha = -2.19 \pm 4.05, \beta = 1.07 \pm 0.11$ and $\varepsilon = 0.25 \pm 0.05$. However, for our sample we get a larger ε-factor which represents a higher uncertainty in the observed values. As the conversion from the 944 MHz luminosity to kinetic luminosity at 1.4 GHz depends on a number of assumptions we introduce large errors which result in a high scatter of the relation. Also, our sample is smaller than in P22 which also results in a higher scatter. We also note that considering a sample over a wide redshift range can introduce a bias into this estimation (Godfrey & Shabala, 2016). Previous results from P22 stating that in most clusters the heating from the central AGN balances the ICM radiative losses cannot be confirmed from our data (see also e.g.McNamara & Nulsen (2012); McNamara et al. (2016a) for a review). However, we note that P22 uses additional COSMOS data of lower-luminosity galaxy groups to the initial eFEDS data (see their Fig. 10). If the COSMOS data is removed from their data, their correlation between the kinetic luminosity at 1.4 GHz and L_{X} also becomes much less significant. It appears that the scatter in the radio luminosity increases strongly with L_X, similar to the results of Main et al. (2017). At values $L_X > 10^{43}$ erg s^{-1} the correlation disappears. The kinetic luminosity acts as a proxy for the heating rate and the X-ray luminosity acts as a proxy for the cooling rate. Hence, the central AGN appear to counterbalance radiative losses from the ICM in low-luminosity clusters and groups but this relation breaks for high-luminosity clusters. Main et al. (2017) also investigated this relation finding that a correlation between kinetic luminosity and X-ray observables is only existent in clusters with short (< 1 Gyr) central cooling times. We derive the central cooling time t_{cool} based on the X-ray temperature and color-code the individual points with respect to t_{cool} in Fig. 3.10 to examine if t_{cool} has an impact on the individual cluster position in the $L_{\mathrm{kin}} - L_{\mathrm{X}}$ diagram. From our data, we cannot confirm the results from Main et al. (2017). In high-luminosity clusters the variability among the AGN population seems to be higher resulting in a higher scatter in the $L_{\mathrm{kin}} - L_{\mathrm{X}}$ correlation. However, the measurements are only a snapshot in the lifetime of an AGN at a certain point in their duty cycle. Averaged over a longer period, AGN heating could still balance cooling but the implication is that at higher L_X the AGN are

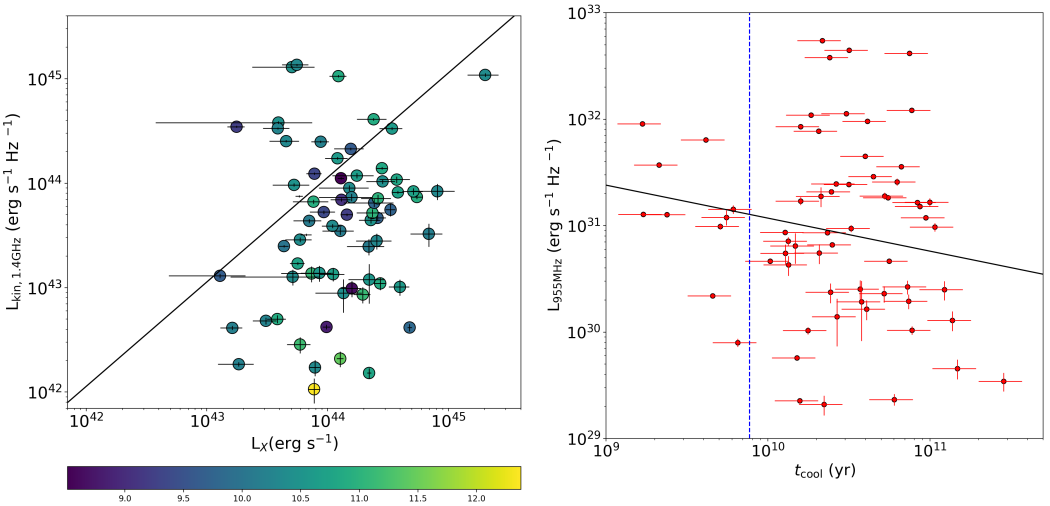

Figure 3.10 *Left Panel:*1.4 GHz kinetic luminosity extrapolated from 944MHz versus the X-ray luminosity of the corresponding cluster. The individual points are color-coded with respect to the logarithmic central cooling time. *Right Panel:* The 944 MHz radio luminosity of the central radio source versus the central cooling time of each cluster. The dashed blue vertical line indicates $t_{\mathrm{cool}} = 7.7$ Gyr and separates CC and NCC clusters. The black line indicates the fit: $\log L_{\mathrm{R}} = (-0.31 \pm 0.03) \cdot \log \mathrm{t_{cool}} + (34.17 \pm 0.31)$

3.3.6 Cooling time

As AGN feedback heats the ICM and regulates its cooling rate, studying the correlation between central cooling time and radio luminosity can be used to investigate the relation between ICM cooling and AGN heating. As the eRASS:1 cluster catalog provides the central density n_e and the temperature T_X for all clusters, the central cooling time can be approximated as (Sarazin, 1986):

$$t_{\mathrm{cool}} = 8.5 \cdot 10^{10}\mathrm{yr}\left(\frac{n_P}{10^{-3}\mathrm{cm}^{-3}}\right)^{-1}\left(\frac{T_{\mathrm{g}}}{10^{8}\mathrm{K}}\right)^{\frac{1}{2}}.$$

Here, we assume the hydrogen density $n_P = 0.83n_e$ (McDonald et al., 2018). We plot the cooling time t_{cool} versus the radio luminosity L_{R} in the right panel of Fig. 3.10. We cut out two outliers with derived central cooling times of $> 10^{12}$ yr, as these values are most likely the result of incorrect densities and temperatures in the catalog data. While the plot is messy, there seems to be a trend of an anti-correlation between the two quantities. To quantify this anti-correlation, we find $\log L_{\mathrm{R}} = (-0.31 \pm 0.03) \cdot \log \mathrm{t}_{\mathrm{cool}} + (34.17 \pm 0.31)$. We also indicate $t_{\mathrm{cool}} = 7.7$ Gyr as this value is commonly used to distinguish between cool-core (CC) and non cool-core clusters (NCC). We see that our sample contains 10 CC clusters while the rest are NCC clusters. Mittal et al. (2009) examined a sample of 64 HIFLUGCS clusters and their central radio galaxies and found a similar trend for an anti-correlation between the cooling time of the cluster and the radio luminosity of its central AGN. For their sample they find a slope of -3.16 ± 0.38 in contrast to our relation where we find a slope of -0.31 ± 0.03. We note that Mittal et al. (2009) use a central definition of 0.4% of r_{500} which is a radius that cannot be resolved by eROSITA. Hence, any comparison should be handled with care. In general this apparent anti-correlation could be indicative of a need for more powerful AGN in clusters with short central cooling times. Cool-core clusters with very short cooling times seem to need much more powerful AGN unlike NCC clusters where this trend is less obvious. Finally, the cluster mass also appears to play a role. Bharadwaj et al. (2014) investigated the same relation for galaxy groups finding no relation between the central cooling time and the radio luminosity of the central AGN. For a discussion of the difference of AGN feedback in clusters and groups we refer to Pasini et al. (2021).

3.3.7 Density profiles

In order to investigate the connection between CC and NCC clusters and their corresponding radio luminosity we plot the density profiles of all clusters of our sample and color-code them by their radio power. The resulting plot is shown in fig. 3.11. Again we cut out the density profiles of two outliers with very low central densities of $n_e < 10^{-4}$ as we assume these values are incorrect. We can see that clusters with a higher central density ($n_e > 10^{-2}\mathrm{cm}^{-3}$), subsequently CC clusters tend to host more luminous radio sources with radio luminosities of $L_{\mathrm{R}} > 10^{31}$ erg s^{-1} Hz^{-1} confirming that CC clusters are always hosting a powerful radio-mode AGN. For clusters with lower central densities ($n_e < 10^{-2}\mathrm{cm}^{-3}$), we do not find any connection and draw the conclusion that NCC clusters host low as well as high luminous radio sources. This is in overall agreement with the general findings that X-ray cavities and therefore powerful radio-mode AGN are usually found within CC clusters, e.g. (Bîrzan et al., 2020; Hlavacek-Larrondo et al., 2012; Olivares et al., 2022; O'Sullivan et al., 2011). In contrast to this strong connection of AGN activity and CC clusters, there seems to be no correlation between NCC clusters and AGN activity. Mittal et al. (2009) showed that also NCC clusters may host strong radio AGN that can be explained, e.g., by merging activities or other mechanisms.

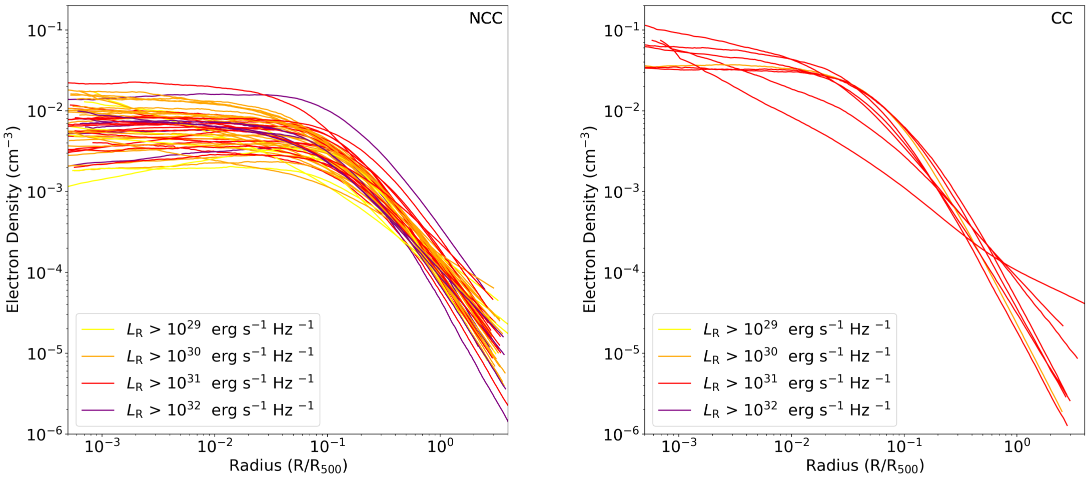

Figure 3.11 *Left Panel:* The electron density profiles of all non cool-core clusters versus the radius scaled to R$_{500}$. The colors of the profiles represent the radio luminosity of the central radio source of the corresponding cluster.*Right Panel:* The corresponding plot for the cool-core clusters.

3.3.8 Noteworthy clusters

In our cluster sample we find some interesting radio sources, four of which we present here in Fig. 3.12. The upper left panel shows galaxy cluster J201832.9-524656 (Abell S0861) at $z = 0.05$ with the white circle being R_{500}. This cluster contains two interesting radio sources that have very elongated shapes. We also show the overlay with optical data from the legacy survey DR9 where we can see that the upper radio source presumably consists of at least three galaxies exhibiting radio emission. The shape of the radio emission suggests a complex interplay between these galaxies. The southern radio source in J201832.9-524656 resembles the shape of a jellyfish galaxy. In the optical overlay we discover a bright galaxy in the upper part of the radio galaxy. This shape suggests that this galaxy is moving towards the northwest.

The upper right panel of Fig. 3.12 shows cluster J205156.7-523752 (PLCKESZ G345.4-39) at $z = 0.04$. This cluster is hosting two elongated shaped radio sources in the southern part of the cluster that seem to be connected. The optical overlay with legacy survey DR9 data reveals that the upper radio source consists of two near galaxies and the upper radio source of at least one radio galaxy. The shapes of these sources suggest that these galaxies have either undergone some merging activities in the past or will in the future. In the lower left we display the cluster J202321.7-553524 (SPT-CL J2023-5535) at $z = 0.22$. The radio image of this cluster reveals a large radio source covering large areas of the whole cluster with a strong peak in the south-east. This radio source could be an indication for a radio halo and has also been studied by HyeongHan et al. (2020). In the lower right panel we display the nearby cluster J215129.7-552019 (RXC J2151.3-5521) at $z = 0.03$, where we clearly see the radio jets originating from the central radio source in the cluster.

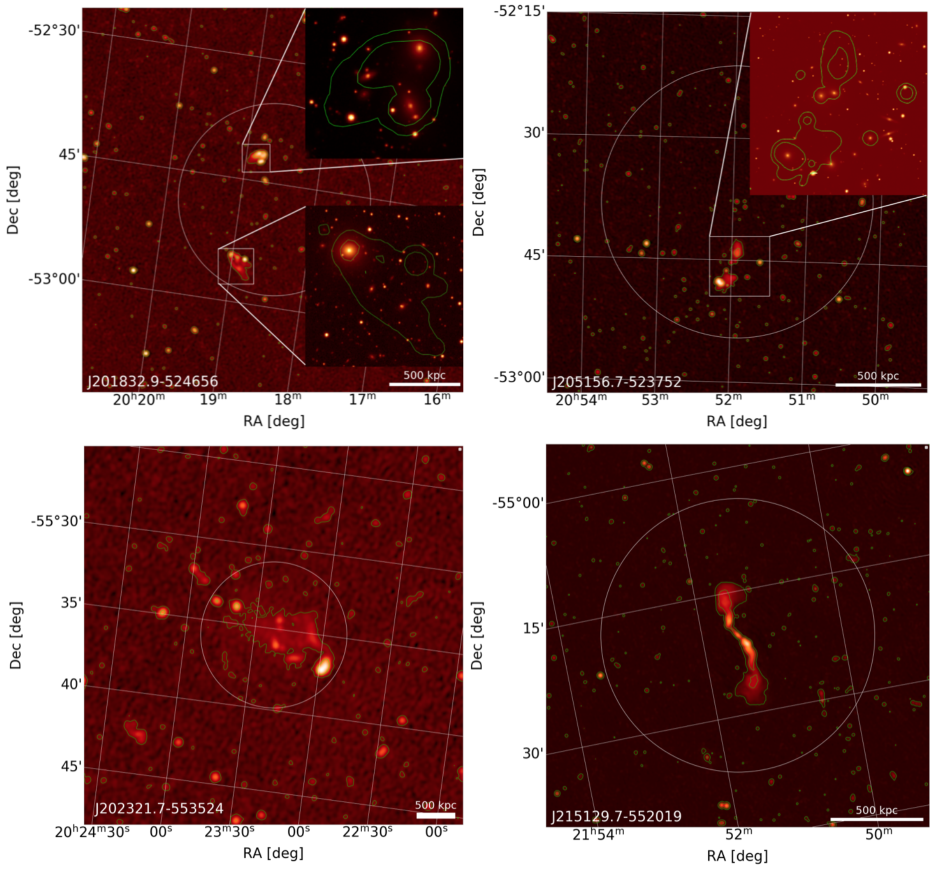

Figure 3.12 Special radio sources contained in the EMU field. *Upper left panel:* Radio cutout from the EMU image of cluster J201832.9-524656 (Abell S0861) at $z = 0.05$ showing two elongated radio sources. The optical overlay reveals a complex interplay between at least three radio galaxies on the northern radio source and an infalling radio galaxy in the southern source. *Upper right panel:* The radio cutout of J205156.7-523752 (PLCKESZ G345.4-39) at $z = 0.04$ shows two connected elongated radio sources that seem to be hosted by at least three radio galaxies. *Lower left panel:* Radio image of J202321.7-553524 (SPT-CL J2023-5535) at $z = 0.22$ revealing a large radio source. *Lower right panel:* Cutout of the nearby cluster J215129.7-552019 (RXC J2151.3-5521) at $z = 0.03$ clearly showing the radio jets that originate from the central radio source. All optical overlays made use of legacy survey DS9 data, and the white circle represents R_{500}.

3.4 Conclusions

We used the eROSITA eRASS:1 cluster catalog and the ASKAP pilot survey EMU to examine the central radio galaxies hosted in galaxy clusters covered in the EMU survey. We can draw the following conclusions:

1. Our sample consists of 75 galaxy clusters that are covered by the EMU pilot survey in a redshift range of $0.03 < z < 1.1$. 10 are cool-core clusters while the rest are non cool-core clusters. In 64 clusters we could identify a radio source corresponding to the clusters BCG. The radio luminosities of the central radio galaxies at 944 MHz range between $\sim 10^{29}$ and $\sim 10^{33}$ erg s^{-1} Hz^{-1}. The X-ray luminosities of the corresponding clusters range between $\sim 10^{43}$ and $\sim 10^{45}$ erg s^{-1}.
2. We compared the offset of the BCG from the cluster center to its concentration parameter, finding a link between the clusters dynamical state to its BCG offset with larger offsets found in more disturbed systems.
3. We find a statistically significant correlation between the radio and the X-ray luminosity as found in previous work (Mittal et al., 2009; Pasini et al., 2022; Pasini et al., 2020, 2021).
4. We investigated the correlation between the LLS of the radio source and its radio power finding that larger radio galaxies tend to be more powerful. We do not find a correlation between the central density and the LLS which suggests that the radio power is more important than ambient density in influencing the size of the radio galaxy.
5. The 944 MHz luminosities were converted to 1.4 GHz kinetic luminosities using scaling relations. We found that in high luminosity clusters with $L_{\mathrm{X}} > 10^{43}$ erg s^{-1} the kinetic luminosity of the radio jets is not longer correlated with the X-ray luminosity which is an implication for the variability in AGN population to be higher among high luminous clusters.
6. We found an anti-correlation between the central cooling time t_{cool} and the radio luminosity L_{R} indicating that more powerful AGN reside in clusters with short central cooling times.
7. The density profiles of the individual clusters show that cool-core clusters tend to host powerful radio sources in contrast to non cool-core clusters that host both, high and low luminosity radio sources.
8. A mid-infrared color criterion using WISE colors is applied to our sample and we conclude that the color criterion is not applicable for our sample which is due to the luminosity range of our sample where the WISE criterion is not applicable.

The eRASS cluster catalog is a powerful tool that will prove useful for future studies. The combination with radio surveys by the forthcoming generation of radio telescopes will vastly extend samples such as this one.

4 Evidence of Extended Dust and Feedback around z$\sim$1 Quiescent Galaxies via Millimeter Observations

This chapter is based on the published article "Evidence of Extended Dust and Feedback around z$\sim$1 Quiescent Galaxies via Millimeter Observations", J. Meinke, S. Cohen, J. Moore, K. Böckmann, P. Mauskopf, E. Scannapieco, 2023, The Astrophysical Journal, Volume 954, Issue 2, id.119, 21 pp.

4.1 Introduction

Much is still unknown about the evolution of our universe's most massive galaxies and the processes that shaped them. These elliptical galaxies are comprised of a central massive black hole, surrounded by a bulge of old, red stars. An additional mechanism is needed to explain the lack of young stars in these galaxies, (Silk & Rees, 1998; Somerville & Davé, 2015b), and the prevailing consensus is that star formation is quenched by feedback on the surrounding environment by active galactic nuclei (AGN) (Bower et al., 2006; Croton et al., 2006; Granato et al., 2004; Scannapieco & Oh, 2004). Observations of galaxy stellar mass are well explained by AGN feedback, showing a 'downsizing' or drop in star formation rate for progressively lower masses with decreasing redshift (Cowie et al., 1996; Drory & Alvarez, 2008; Treu et al., 2005), which is contrary to hierarchical models of galaxy formation with no feedback present (Rees & Ostriker, 1977; White & Frenk, 1991).

Yet, many aspects of AGN feedback remain uncertain, with two commonly proposed feedback models. In 'quasar mode' feedback, the circumgalactic medium (CGM) surrounding the galaxy is impacted by a powerful outburst when the supermassive black hole is accreting most rapidly. In this case, the CGM is heated such that the gas cooling time is much longer than the Hubble time, suppressing further star formation until today. These models are supported by observations of high-velocity flows of ionized gas associated with the black holes accreting near the Eddington rate (Greene et al., 2014; Harrison et al., 2014; Lansbury et al., 2018; Miller et al., 2020). Unfortunately, uncertainty arises in the mass and energy flux from such quasars due to uncertain estimates of the outflowing material's distance from the central source (Chamberlain et al., 2015; Chartas et al., 2007; de Kool et al., 2001; Dunn et al., 2010; Feruglio et al., 2010; Veilleux et al., 2013; Wampler et al., 1995).

Second, in 'radio mode' feedback, cooling material is more gradually prevented from forming stars by jets of relativistic particles that arise during periods of lower accretion rates. Here, the CGM is maintained at a roughly constant temperature and entropy, as low levels of gas cooling are continually balanced by energy input from the relativistic jets. Such models are supported by AGN observations of lower power jets of relativistic plasma (Fabian, 2012). These couple efficiently to the volume-filling hot atmospheres of galaxies clusters (Churazov et al., 2001; McNamara et al., 2016b, 2000), but may or may not be significant for balancing cooling in less massive gravitational potentials (Werner et al., 2019).

One of the most promising methods for distinguishing between these models is by looking at anisotropies in the cosmic microwave background (CMB) photons passing through hot, ionized gas. Sufficiently heated gas will impose observable redshift-independent fluctuations in the CMB known as the thermal Sunyaev-Zel'dovich (tSZ) effect (Sunyaev & Zeldovich, 1972). The resulting CMB anisotropy has a distinctive frequency dependence, which causes a deficit of photons below and an excess above $\nu_{\rm null} = 217.6\,{\rm GHz}$. The change in CMB temperature ΔT as a function of frequency due to the (non-relativistic) tSZ effect is given by

$$\frac{\Delta T}{T_{\rm CMB}} = y\left(x\frac{e^x+1}{e^x-1} - 4\right), \tag{4.1}$$

where the dimensionless Compton-y parameter is defined as

$$y \equiv \int dl\, \sigma_T \frac{n_e k\left(T_e - T_{\rm CMB}\right)}{m_e c^2}, \tag{4.2}$$

where σ_T is the Thomson cross-section, k is the Boltzmann constant, m_e is the electron mass, c is the speed of light, n_e is the electron number density, T_e is the electron temperature, $T_{\rm CMB} = 2.725$ K is the CMB temperature used throughout this paper, l is the line-of-sight distance over which the integral is performed, and x is the dimensionless frequency given by $x \equiv h\nu/kT_{\rm CMB} = \nu/56.81\,{\rm GHz}$, with Planck constant h.

Proportional to both n_e and T, the Compton-y parameter provides a measure of the total pressure along the line-of-sight. Therefore by integrating the tSZ signal over a patch of sky, $y(\boldsymbol{\theta})$, we can obtain the volume integral of the pressure, and calculate the total thermal energy $E_{\rm th}$ in the CGM associated with a source (e.g. Mroczkowski et al., 2019b; Scannapieco et al., 2008). Detailed in Spacek et al. (2016), this gives

$$E_{\rm th} = 2.9\times 10^{60}{\rm erg}\left(\frac{D_{\rm a}}{\rm Gpc}\right)^2 \frac{\int y(\boldsymbol{\theta})\; d\boldsymbol{\theta}}{10^{-6}\ {\rm arcmin}^2}. \tag{4.3}$$

where $D_{\rm a}$ is the angular diameter distance in Gpc and the integrated compton-y is in units of 10^{-6} arcmin^2. Throughout this work, we adopt a ΛCDM cosmological model with parameters (within limits from Planck Collaboration et al., 2020), $h = 0.68$, $\Omega_0 = 0.31$, $\Omega_\Lambda = 0.69$, and $\Omega_b = 0.049$, where h is the Hubble constant in units of 100 km s^{-1} Mpc^{-1}, and Ω_0, Ω_Λ, and Ω_b are the total matter, vacuum, and baryonic densities, respectively, in units of the critical density.

The relationship of eq. (4.3) means that improvements in the sensitivity and angular resolution of tSZ measurements translate directly to better constraints on thermal energy. Thus, cosmic structures with higher gas thermal energies, galaxy clusters, are most easily detected and indeed, have been the focus of tSZ measurements over the last decade (e.g. Hilton et al., 2018; Lokken et al., 2022; Planck Collaboration et al., 2014; Reichardt et al., 2013).

Further challenges arise when going to lower mass halos. Bright targets such as quasars with abundant amounts of outflowing gas are detectable in tSZ on an individual basis using ALMA (Brownson et al., 2019; Lacy et al., 2019). However, averaging over many objects is currently required for appreciable detection of most samples. Chatterjee et al. (2010) stacked quasars and galaxies with data from the Wilkinson Microwave Anisotropy Probe (WMAP) and Sloan Digital Sky Survey (SDSS) to find a tentative $\approx 2\sigma$ tSZ signal suggesting AGN feedback; Hand et al. (2011) used data from SDSS and the Atacama Cosmology Telescope (ACT) to see a $\approx 1\sigma - 3\sigma$ tSZ signal around galaxies; Gralla et al. (2014) found a $\approx 5\sigma$ detection for AGNs with ACT; Ruan et al. (2015) used SDSS and Planck to find $\approx$ $3.5\sigma - 5.0\sigma$ tSZ signals around both quasars and galaxies; Crichton et al. (2016) used SDSS and ACT to find a $3\sigma - 4\sigma$ SZ signal around quasars; Hojjati et al. (2016) found a $\approx 7\sigma$ tSZ detection suggestive of AGN feedback with data from Planck and the Red Cluster Sequence Lensing Survey; and (**?**) used ACT, Herschel, and the Very Large Array data to measure the tSZ effect around $\approx 100,000$ optically selected quasars, finding a 3.8σ signal that provided a joint constraint on AGN feedback and mass of the $z \gtrsim 2$ quasar host halos.

Recent measurements have also been made around massive galaxies. Greco et al. (2015) used SDSS and Planck data to compute the average tSZ signal from a range of over 100,000 'locally brightest galaxies' (LBGs) at $z \lesssim 0.5$. This sample was large enough to derive constraints on $E_{\rm th}$ as a function of galaxy stellar mass $M_\star$ for objects with $M_\star \gtrsim 2 \times 10^{11}$ $\rm M_\odot$. At redshifts $0.5 \lesssim z \lesssim 1.5$ Spacek et al. (2016, 2017) studied the tSZ signal from massive quiescent galaxies. These are prime candidates for which AGN feedback is thought to quench star formation and where a significant excess tSZ signal is expected to be produced in the CGM (e.g. Scannapieco et al., 2008). Spacek et al. (2016) performed a stacking analysis with the 150 and 220 GHz South Pole Telescope's (SPT) 2011 data release, using a 43 $\rm deg^2$ overlap with VISTA Hemisphere Survey and Blanco Cosmology Survey data to select samples of up to 3394, finding a $\approx 2 - 3\sigma$ signal hinting at non-gravitational heating. While Spacek et al. (2017) used SDSS and the Wide-Field Infrared Survey Explorer (WISE) data overlapping with 312 $\rm deg^2$ of 2008/2009 ACT data at 148 and 220 GHz, finding a marginal detection that was consistent with gravitational-only heating models. With the latest SPT release covering 2500 $\rm deg^2$, Meinke et al. (2021) stacked nearly $140,000$ quiescent galaxies selected in a similar process from the Dark Energy Survey (DES) and WISE, to obtain a combined 10.1σ detection of tSZ at $z \approx 1$. They found the signal was most consistent with moderate forms of AGN feedback models.

Other measurements with the latest *Planck* y-maps have been successfully conducted on nearby targets. Support for AGN feedback in local galaxy groups was found by Pratt & Bregman (2020). While Bregman et al. (2022) observed a 4.0σ detection of the tSZ effect in 11 local L^* spiral galaxies.

The recent ACT DR5 data release (Mallaby-Kay et al., 2021) has unlocked additional parts of the sky for detailed analysis. Schaan et al. (2021) and Amodeo et al. (2021) combined microwave maps from ACT and Planck with galaxy catalogs from the Baryon Oscillation Spectroscopic Survey (BOSS), to study the gas associated with these galaxy groups. They constrained the gas density profile through measurements of the tSZ signal at $\approx 10\sigma$ and a weaker detection of the kinetic Sunyaev-Zel'dovich effect (kSZ, Sunyaev & Zeldovich, 1980), which is caused by peculiar motions. They were able to compare these results to cosmological simulations (Battaglia et al., 2010; Springel et al., 2018) to find that the feedback employed in these models was insufficient to account for the gas heating observed at $\approx$ Mpc scales. Meanwhile Calafut et al. (2021) and Vavagiakis et al. (2021) used SDSS and ACT to detect kSZ measurements consistent with one another. Vavagiakis et al. (2021) also found up to a 12σ detection of the tSZ in their galaxy groups and clusters. A novel oriented stacking method was also used in Lokken et al. (2022) on DES clusters to identify tSZ associated with the cosmic web. These are just a first step in a new wave of tSZ and kSZ analyses as more data becomes available.

A significant difficulty in accurate tSZ detection is the presence and removal of dust. This becomes all the more important for higher redshift samples in far-infrared and millimeter bands. Many tSZ studies have sought to simply remove this contaminant source, although there have also been an increasing number of mid- and far-infrared (MIR; FIR) studies with a primary emphasis on the dust associated with galaxies (Berta et al., 2016; Gobat et al., 2018). Dust is an excellent tracer of galaxy characteristics such as star formation and gas, and is a key component in understanding galaxy dynamics (Calura et al., 2017; Donevski et al., 2020; Santini et al., 2014). Despite having a lower star formation rate, dust in quiescent galaxies is still significant. A recent study by Magdis et al. (2021) highlights a noticeable increase in dust-to-stellar mass ratio for quiescent galaxies between $z = 0$ and $z = 1$.

Here we expand upon the work of Meinke et al. (2021) by including the recent millimeter-wave data from ACT DR5 and conducting a more detailed analysis of dust. Using the same quiescent galaxy selection method with DES and WISE, we now analyze data from where the SPT and ACT telescopes overlap within $\approx 2,100\ \mathrm{deg}^2$ in the Southern Hemisphere. An ACT-only analysis is also conducted over the wider ACT field, which shares $\approx 4,600\ \mathrm{deg}^2$ with DES and WISE. We apply a two-component fit to separate the tSZ and dust components, both in bins by radial profile and stellar mass. We compare these profiles to expectations and other relevant studies, detecting signals up to 11σ tSZ and 20σ dust in the centermost radial bins. Divided into stellar mass bins, we calculate the thermal energy and dust mass versus stellar mass. We then compare our thermal energies to current simple feedback models to provide needed constraints for future simulations.

In Section 4.2 we describe all datasets used for our analysis. In Section 4.3 we outline our galaxy selection procedure, and the overall properties of the massive, moderate-redshift, quiescent galaxies we use for stacking. In Section 4.4, we detail all considerations and stacking processes used (Section 4.4.1-4.4.8), followed by our various results extracted from both the dust and tSZ associated with our samples (Section 4.4.9-4.4.13). Discussions are given in Section 4.5.

4.2 Data

Our analysis uses five public datasets: two for galaxy selection, and three to conduct our stacking analysis upon. For selection, we make use of optical and near-infrared data from DES data release 1 (Abbott et al., 2018), which are already matched to AllWISE data spanning $3 - 25\ \mu m$ (Schlafly et al., 2019). We select and carry out photometric fitting of passive galaxies at $0.5 \lesssim z \lesssim 1.5$ that requires this large span of wavelengths. Finally, the maps we stack include millimeter-wave observations from both the SPT-SZ (Bocquet et al., 2019) and ACT surveys (Naess et al., 2020), along with a Planck component-separated CMB map (Planck

Collaboration et al., 2020). The datasets are described in more detail below. Footprints of DES, SPT-SZ and ACT DR5 are shown in Fig. 4.1.

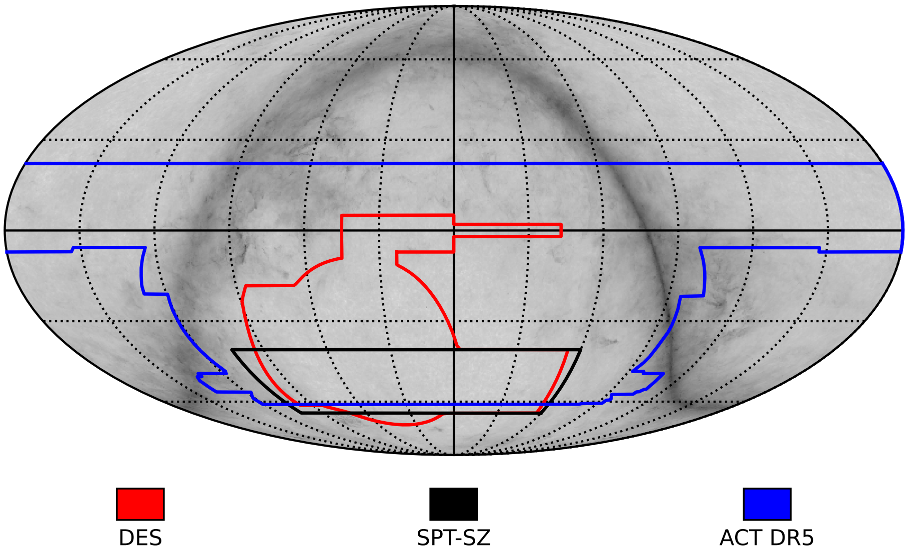

Figure 4.1 Mollweide (equatorial) projected sky footprints showing the coverage of DES (*red*), SPT-SZ (*black*), and ACT (*blue*) surveys used in this analysis. The *Planck* HFI 353 GHz is shown in the background. This was made with the help of publicly available resources at `https://lambda.gsfc.nasa.gov/toolbox/footprint/`.

4.2.1 DES

DES DR1 consists of optical and near-infrared imaging from 345 nights between August 2013 to February 2016 by the Dark Energy Camera mounted on the 4-m Blanco telescope at Cerro Tololo Inter-American Observatory in Chile. The data covers $\approx$ 5000 deg^2 of the South Galactic Cap in five photometric bands: grizY. These five bands have point-spread functions of g = 1.12, r = 0.96, i = 0.88, z = 0.84, and Y = 0.90 FWHM (Abbott et al., 2018). The survey has exposure times of 90s for griz and 45s for Y band, yielding a typical single-epoch PSF depth at S/N = 10 for g $\lesssim$ 23.57, r $\lesssim$ 23.34, i $\lesssim$ 22.78, z $\lesssim$ 22.10 and Y $\lesssim$ 20.69 mag (Abbott et al., 2018). Here and below, all magnitudes are quoted in the AB system (i.e. Oke & Gunn, 1983).

4.2.2 WISE

The AllWISE catalog is derived from data from the 40 cm diameter Wide-field Infrared Survey Explorer (WISE) NASA Earth orbit mission (Mainzer et al., 2011; Wright et al., 2010). WISE carried out an all-sky survey in 2010 of the sky in bands W1, W2, W3 and W4, centered at 3.4, 4.6, 12 and 22 μm, respectively (Schlafly et al., 2019). AllWISE uses the post-cryogenic data of the WISE mission to produce a deeper coverage in W1 and W2, which are the two bands used here.

Table 4.1 Galaxy catalogs used in this analysis with redshifts and stellar mass statistics.

Sample Name	Map Fields	N	$\widetilde{z}$	$\overline{z}$	$\log_{10}(\widetilde{M_\star}/\mathrm{M}_\odot)$	$\log_{10}(\overline{M_\star}/\mathrm{M}_\odot)$
Overlap Sample	SPT, ACT	$94,452$	1.031	1.063	11.36	11.41
Wide-Area Sample	ACT	$387,627$	1.037	1.066	11.40	11.44

Both catalogs were selected from DES and WISE as described in Section 4.3.

The added sensitivity of AllWISE extends the detection limit of luminous distant galaxies because their apparent brightness at 4.6 μm (W2) no longer declines significantly with increasing redshift. The increased sensitivity yields better detection of those galaxies for redshift $z > 1$, which are the primary focus of this analysis.

4.2.3 SPT-SZ

The SPT-SZ survey (Chown et al., 2018) covered $2,500$ deg^2 of the southern sky between 2007 to 2011 in three different frequencies: 95 GHz and 150 GHz, which lie on either side of the maximum tSZ intensity decrement ($\approx$ 128 GHz), and 220 GHz, which is very near the tSZ null frequency, $\nu_{\mathrm{null}} = 217.6$ GHz. The South Pole Telescope (SPT) is a 10 m telescope located within 1 km of the geographical South Pole and consists of a 960-element bolometer array of superconducting transition edge sensors.

The SPT maps used in this analysis are publicly available[1] combined maps of SPT and all-sky Planck satellite (with similar bands at 100, 143, and 217 GHz). Each combined map has a provided beam resolution of 1.85 FWHM, and is given in a HEALPix (Hierarchical Equal Area isoLatitude Pixelation) format with $N_{\mathrm{side}} = 8192$ (Chown et al., 2018).

4.2.4 ACT

The DR5 data release from the Atacama Cosmology Telescope (ACT) contains combined maps from observations during 2008-2018 (ACT-MBAC and ACTpol, **??**). These are publicly available[2] and cover $\approx 18,000\,\mathrm{deg}^2$, predominantly in the Southern Hemisphere. ACT uses a 6 m telescope with transition edge bolometer detectors. The provided maps include three frequency bands centered near 90, 150, and 220 GHz. For our purpose, we use the combined ACT+*Planck*, day+night, source-free frequency maps. These have provided FWHM resolutions of 2.1, 1.3, and 1.0, respectively. ACT maps differ from SPT and *Planck* by projection; instead given in CAR (Plate-Carrée), cylindrical coordinates of right ascension and declination.

4.2.5 Planck

The *Planck* Satellite was launched in 2009 by the European Space Agency and operated from 30 to 857 GHz in 9 total frequency bands. Taking measurements until 2013, *Planck* proved in-

---

[1] `https://lambda.gsfc.nasa.gov/product/spt/index.cfm`

[2] `https://lambda.gsfc.nasa.gov/product/act/actpol_prod_table.cfm`

valuable to the study of CMB anisotropies and the early Universe. Its third and ultimate data release in 2018 included full-sky frequency and component-separated maps (Planck Collaboration et al., 2020). Of importance to us are the *Planck* CMB maps generated from various component separation techniques (Planck Collaboration et al., 2020). Here we have elected to use the *Planck* SMICA (Spectral Matching Independent Component Analysis) SZ-free CMB map with SZ sources projected out, to safely remove large-scale CMB anisotropies around our sample area. This map has a resolution of 5.0 FWHM, provided in HEALPix format with $N_{\text{side}} = 2048$. All of the *Planck* products mentioned are publicly available[3].

4.3 Defining the Galaxy Sample

4.3.1 Selection

We carried out our initial galaxy selection using the DES database server at NOAO, called NOAO-Lab. In order to start with a manageable sample, we applied a cut in color-color space designed to select old galaxies with low star-formation rates at approximately $1.0 \leq z \leq 1.5$ in the initial database query, as previously shown in **?**. We used mag_auto from the DES in *grizy* bands, along with *W1* and *W2* PSF-magnitudes (converted to AB-system) from AllWISE (Mainzer et al., 2011; Wright et al., 2010) joined to the main DES table. The bands and color-selection used here are slightly different than Spacek et al. (2017) used in SDSS Stripe 82.

The NOAO Data lab allows direct queries in SQL via Jupyter notebook on their server. The lines we used to make the color selection were `((mag_auto_z_dered-(w1mpro+2.699)) <= (1.37*mag_auto_g_dered-1.37* mag_auto_z_dered-0.02))` and `((mag_auto_z_dered-(w1mpro+2.699))>=2.0)`.

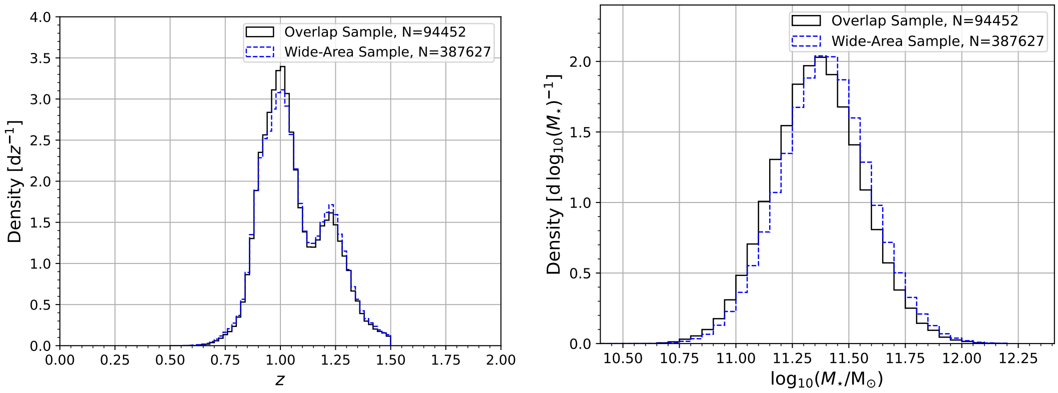

Figure 4.2 (a) Redshift and (b) $\log_{10}$ stellar mass distributions of our Overlap Sample (*black*) that overlaps with both SPT and ACT fields, and a Wide-Area Sample (*blue, dashed*) that utilizes the larger ACT field. Distributions shown are after SED selection, normalized by count N and bin-width.

---

[3] `https://irsa.ipac.caltech.edu/data/Planck/release_3/docs/`

4.3.2 Photometric Fitting

After the galaxies were selected, photometric redshifts were computed using EAZY (Brammer et al., 2008) and the seven broad bands *grizyW1W2*. In calling EAZY, we used the CWW+KIN (Coleman et al., 1980; Kinney et al., 1996) templates, and did not allow for linear combinations. Since we are looking for red galaxies and have a gap in wavelength coverage between *y*-band and *W1*, we were worried that allowing combinations of templates would yield unreliable redshifts, where e.g., a red template was fit to the IR-data and a blue one was fit to the optical data and they met in the wavelength gap.

Once the redshifts were measured, we fit the spectral energy distributions (SEDs) using our own code, following the method in Spacek et al. (2017), to which the reader is referred for more details. Briefly, a grid of BC03 (Bruzual & Charlot, 2003) models with exponentially declining star formation rates (SFRs) was fit over a range of stellar ages, SFHs (i.e., τ), and dust-extinction values ($0 < A_V < 4$). Our code uses BC03 models assuming a Salpeter initial mass function (IMF), but to facilitate comparisons with the literature, we convert all stellar masses to the value assuming a Chabrier IMF (0.24 dex offset; **?**). As in Spacek et al. (2017), we choose as our final sample all galaxies with age$>$ 1 Gyr, $SSFR < 0.01\text{Gyr}^{-1}$, $0.5 < z_{\text{phot}} < 1.5$, and reduced $\chi^2 < 5$. Final redshift and stellar mass distributions are shown in Fig. 4.2.

Table 4.1 outlines the two different final catalogs used in this study. Shared between both SPT and ACT fields is an 'Overlap Sample' consisting of 94,452 quiescent galaxies. Meanwhile, selection of galaxies in the entire ACT field produces a larger 'Wide-Area Sample' of 387,627 galaxies. Unlike Meinke et al. (2021), we do not directly remove any galaxies near source contaminants in order to limit potential radial profile biases. However both SPT and ACT maps are provided with bright sources already masked, as discussed further below.

4.4 Analysis

4.4.1 Neighboring Sources

The SPT-SZ maps contain an applied mask of all bright 150 GHz sources greater than 50 mJy. This was done in Chown et al. (2018), through the removal of all signal within 5 and apodization with a 5 Gaussian beam. For our purposes these locations result in a large hole that potentially skews measurements. We avoid them by using the SPT-SZ provided mask to remove any targets within 20 of a masked pixel. The statistics for our Overlap Sample as listed in Table 4.1 are determined after the removal process has occurred. The random catalog in the overlap field, described in Section 4.4.5, also applies this removal process.

Similarly, we have chosen to use the source-free ACT maps. They however differ from SPT-SZ, as all sources removed were done so using a finer matched filter and fitting procedure (Naess et al., 2020). We have found this source removal process has a minimal effect on our stacking results.

4.4.2 Map Processing

The SPT and ACT maps span similar frequency bands and regions of the sky, making them ideal products for tSZ and dust comparisons. However, we employ multiple steps to further process the maps into similar formats and ensure all likely systemic differences are minimized. Notably:

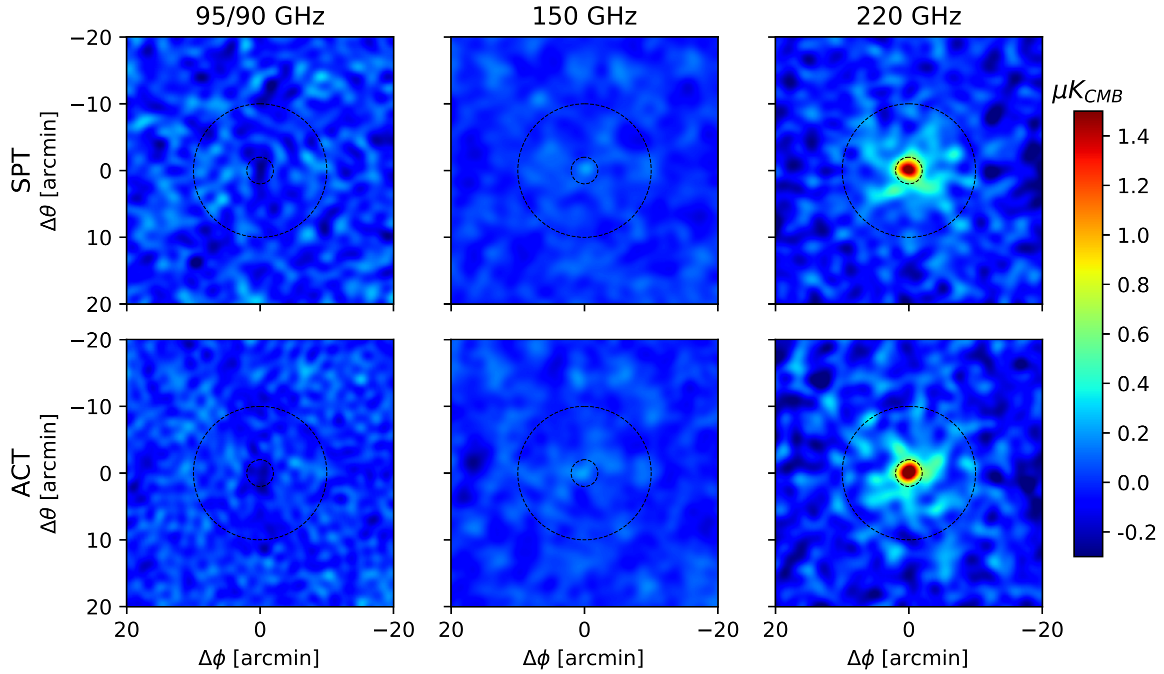

Figure 4.3 Overlap Sample galaxy stacks ($N = 94,452$) for their respective SPT and ACT frequency maps, processed according to Section 4.4.2. A gradient was also removed from each image. Dashed circles correspond to radii of 2.0 and 10.

- The maximum spherical harmonic or Legendre polynomial degree $\ell_{\max}$, differs between the provided maps of SPT ($\ell_{\max} = 10,000$) and ACT ($\ell_{\max} = 30,000$). For consistency, we elect to use the smaller limit of $\ell_{\max} = 10,000$ on each, cutting all higher-order terms within ACT. This removes ACT fluctuations at near pixel-size scales and introduces greater correlation between neighboring pixels, but otherwise does not significantly influence our results.

- Respective beam functions of all frequencies were replaced with a Gaussian beam of 2.10 FWHM. This corresponds to the lowest resolution map (ACT 90GHz). The operation was done on the spherical harmonics ($a_{\ell m}$), with the aforementioned cutoff at $\ell_{\max} = 10,000$.

- To remove any potential discrepancies due to projection differences, all ACT maps in their original Plate-Carée projection were converted into the SPT's HEALPix format with $N_{side} = 8192$. They were first transformed to spherical harmonics, beam and pixel window function corrections applied, and transformed into the final HEALPix map.

- For each frequency map, the SMICA CMB map was masked with the corresponding instrument's boundary mask and converted into spherical $a_{\ell m}$ coefficients. The pixel window function was replaced with the $N_{side} = 8192$ HEALPix pixel window function of the final map format. The CMB map was then subtracted from the desired frequency map(s). This approach is akin to a high-pass filter, removing all large-scale CMB anisotropies to help reduce overall noise at small angular scales and correlation at larger scales.

- The HEALPix projection does not lend itself to uniform stacking of individual pixels and we also seek to place our target galaxies in the direct centers of our measurements. Thus, we make cutouts centered on each target galaxy using a gnomonic-projected grid with a pixel resolution of 0.05. A HEALPix map with $N_{side} = 8192$ has pixel side lengths of roughly 0.18, so we are purposely oversampling for finer alignment. Bilinear interpolation was used to prevent any artificial beam effects from the pixel window function and allow additional precision in positioning. Final image cutouts of our Overlap Sample are shown in Fig. 4.3 in both SPT and ACT processed maps. As outlined in the following subsection, we conducted final measurements on each individual galaxy cutout and then averaged together.

4.4.3 Radial Profile

With the smoothed and CMB-subtracted frequency maps, we measure the radial profile around all galaxies in our catalog. We choose to create radial bins with uniform widths of 0.50, out to a radius of 20.0. For our mean redshift of roughly ≈ 1.1 this translates to a furthest comoving distance of 21 Mpc $\approx 14h^{-1}$ Mpc. Gnomonic projection cutouts were made around each galaxy with a pixel size of 0.05. Cutouts were mean subtracted, and radial bin averages as described above were measured on each catalog location individually. All samples of interest were then averaged with equal weight to create a final radial profile per map.

With three frequencies, we are able to fit both the tSZ and the dust that obscures it. However, any attempts to fit potential mean offsets from CMB or foreground signals would result in overfitting. For this reason we assume all profiles go to zero at large radii. We calculate the average signal in the three largest bins ($18.5 - 20.0$) and subtract it as an offset from the entire radial profile for each frequency map. This method also subtracts any large-scale extragalactic background light (EBL) that might have further biased results. We recognize this subtraction likely truncates a non-zero signal, but at 20 consider it negligible in amplitude and detection. For completeness, we test the effect by comparing different numbers of furthest bin subtractions from one ($19.5 - 20.0$) to ten ($15.0 - 20.0$), which results in a shift of $< 0.5\sigma$ for 95 and 150 GHz radial bin measurements, and $< 1.0\sigma$ for 220 GHz. The 220 GHz causes the most noticeable shift due to it containing the highest S/N at large radii as a result of extended dust emission.

Fig. 4.4 shows these described radial profiles for the $N = 94,452$ Overlap Sample galaxies as measured on the SPT maps, alongside a bootstrap resampled random catalog profile to highlight the lack of any unexpected bias. Our method for calculating uncertainty and random catalog are outlined in the Sections below.

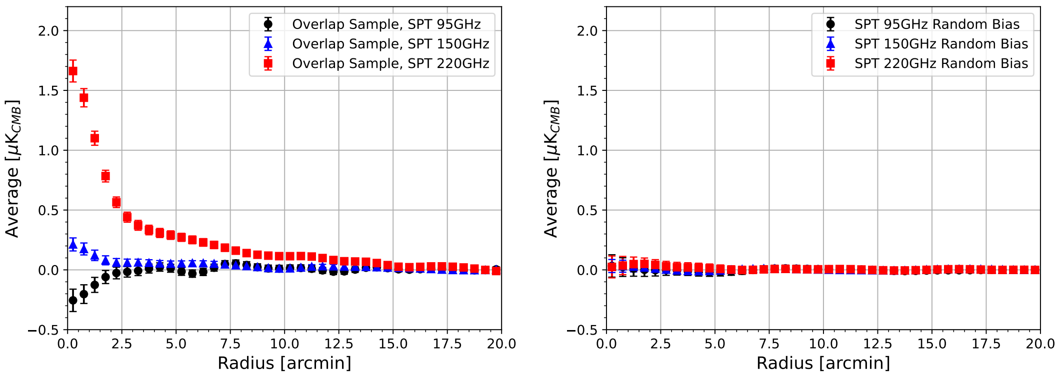

Figure 4.4 Measured radial profiles as detailed in Section 4.4.3 for: (a) all $N = 94,452$ galaxies within the overlap field as measured on the SPT frequency maps of 95, 150, and 220 GHz. (b) Profile of estimated bias in the same SPT maps and overlap field, calculated from bootstrap resampling a catalog of randomly generated positions (Section 4.4.5).

4.4.4 Uncertainties

Correct evaluation of our results requires an accurate calculation of uncertainties. This not only pertains to the error within a radial bin, but also correlation between its neighbors. We employ a bootstrap resampling procedure to construct a covariance matrix across all maps and radial average bins. This is done by resampling our galaxy catalog with replacement and with the same number of objects as the original. We repeat this process for a large number of resamples $(4,000)$ and measure the radial profile in identical fashion to Section 4.4.3. The offset correction done by subtraction of three largest radial bins' average $(18.5 - 20.0)$ likely skews these calculations and results in underestimated noise near large radii. For this reason and low overall S/N at large radii, we elect to not use any radial bins above 15.

The covariance matrix per frequency map is determined from the corresponding distribution of bootstrapped profiles. The tSZ and dust covariance matrices are also calculated via fitting each bootstrap resample to the two-component fit outlined below in Section 4.4.7.

This bootstrapped covariance estimation assumes the noise is independent between each galaxy. However for our sample, radial measurements out to a radius of 20 will on average have a few dozen catalog neighbors. A spatial overlap will thus cause correlation between these neighboring galaxies. This concern has been noted by others, such as Schaan et al. (2021), that found bootstrap resampling produced $\approx 10\%$ underestimation of error at ≥ 6 in their circular apertures.

This effect will also impact our analysis, and its importance will depend on our choice of aperture and the fact that we subtract the large-scale CMB. In our case, our radial profile S/N drops by roughly a factor of three between the center and 6, with the tSZ falling below 2σ by 8. As a result, any profile fits should be largely controlled by the inner radial bins where the effects of underestimated error are minor. To quantify this, we generated 400 mock skies with basic Gaussian noise and measured at identical locations to our samples that showed an underestimation of roughly 10% in variance (or 4.9% error). Thus, we elected to scale all our bootstrapped frequency covariances by 10%, while recognizing larger radial bins may still be slightly underestimated.

If instead we were to apply a 10% error at 6 with a linear scaling relation versus radius, the noise of reported radial profile slopes is increased by up to 50%. However, all other values reported below would remain within quoted margins of uncertainty.

4.4.5 Random Catalog Comparison

To validate our procedure outlined above, we also generate random samples of $1,000,000$ points uniformly distributed within the SPT and ACT catalog footprints. From these, we measure the radial profile (following Section 4.4.3) and bootstrap resample subsets with the same size as our desired galaxy catalog(s). The resultant bootstrap mean corresponds to the expected bias of our sample's background. Fig. 4.4b) shows our bias result of the SPT maps within the SPT-ACT overlap field. Throughout all radial bins the random bootstrap mean stays within 1σ of zero, indicating no additional bias is present.

4.4.6 Fitting Procedure

All fits reported are conducted via Bayesian estimation with the assumption that our measurements are normally distributed but not necessarily independent. The likelihood function is related to our fit residuals $(\mathbf{X}_i - \hat{\mathbf{X}}_i)$ and covariance matrix $(\mathbf{C})$ as

$$\mathcal{L}(\psi|X) = p(X|\psi) \propto \exp\left[-\frac{1}{2}(\mathbf{X}_i - \hat{\mathbf{X}}_i)^T \times \mathbf{C}^{-1} \times (\mathbf{X}_i - \hat{\mathbf{X}}_i)\right], \tag{4.4}$$

incorporating parameters with discrete predefined ranges and priors $p(\psi)$. The posterior distributions are obtained as

$$p(\psi|X) = \frac{p(X|\psi)p(\psi)}{\int p(X|\psi')p(\psi')d\psi'}, \tag{4.5}$$

where we normalize across all combinations of fit parameters (ψ'). This is calculated for the ψ-dimensional array for all possible parameter combinations and implemented via our own custom Python code. Each parameter's reported best fit is classified as the median (50th percentile) after the posterior is marginalized over all other parameter ranges. Similarly, the 1σ bounds are calculated as the 16th and 84th percentiles.

4.4.7 Two Component Fitting

From our aperture measurements, we used a two-component fitting model consisting of tSZ (y) and the dust spectral intensity at $\nu_0 = 353$ GHz in the source's rest frame $I_r(\nu_0)$ with units [W Hz^{-1}m^{-2}sr^{-1}],

$$\delta T(\nu) = y\, g(\nu)\, T_{CMB} + \frac{I_r(\nu_0)}{(1+z)^2} \frac{I_o(\nu)}{I_r(\nu_0)} \left.\frac{dT}{dB(\nu,T)}\right|_{T_{\rm CMB}}, \tag{4.6}$$

where $g(\nu) = [x\ (e^x + 1)/(e^x - 1) - 4]$ of the tSZ signal (eq. 4.1) and $B(\nu, T)$ is the Planck function. The $(1+z)^{-2}$ term arises from redshift corrections due to time dilation and energy. $I_o(\nu)$ is the specific dust intensity in the observed frequency band ν. It is converted to the rest frame band $\nu\,(1+z)$,

$$I_o(\nu) = (1+z)\ I_r\left[\nu\ (1+z)\right], \tag{4.7}$$

where we assume a gray-body dust spectrum for I_r with a dust temperature (T_d) and spectral emissivity index (β). Thus, the intensity term from eq. (4.6) can be written as

$$\frac{I_o(\nu)}{I_r(\nu_0)} = (1+z)\left[\frac{\nu\ (1+z)}{\nu_0}\right]^{\beta} \frac{B[\nu\ (1+z), T_d]}{B(\nu_0, T_d)}, \tag{4.8}$$

normalized with respect to $I_r(\nu_0)$. This normalization term helps define a reference frequency for all measurements while reducing the correlation between dust temperature and intensity amplitude when near the Rayleigh-Jeans limit. Equation 4.6 is integrated over each respective map's frequency band response. The SPT bands were extracted from **?**, as the SPT+Planck maps are dominated by the SPT response for most of our angular scales. Full ACT bandpasses were available as a function of position, detector array, and multipole ℓ. We average each ACT response across our field of observation, all detectors, and with a cut of $2,000 < \ell <= \ell_{\mathrm{max}}$. The $\ell = 2,000$ minimum was chosen to reflect our angular scales of interest and subtraction of the large-scale CMB (Section 4.4.2). The observed flux in mJy integrated within a simple circular aperture of $R = 2.0$ radius is shown in Fig. **??** for our Overlap and Wide-Area samples, respectively. This circular aperture is further used in our stellar mass binning shown in Section 4.4.12.

The two component fit described above was also applied to each set of frequency measurements per radial bin for all listed catalogs in Table 4.1. We assume priors as outlined in Table 4.2 for all fits. Uniform priors are set for the Compton-y ($0 \leq y \leq 4 \times 10^{-7}$) and dust intensity in the 220 GHz rest frame ($0 \leq I_r(\nu_0) \leq 4 \times 10^{-24}$ W Hz^{-1}m^{-2}sr^{-1}). In the event of fits near zero indicating low signal to noise, we shift these uniform priors to include slight negative values. Thus, in the absence of a signal we will then correctly produce a result centered about zero. Gaussian priors were assumed for the additional parameters of dust emissivity ($\beta = 1.75 \pm 0.25$) and dust temperature ($T_{\mathrm{d}} = 20 \pm 3$ K). These Gaussian priors were chosen to align within standard ranges (Addison et al., 2013; Draine, 2011; Magdis et al., 2021), but were not set as free uniform parameters due to our limited number of maps to fit. The resultant dust parameter fits are found to be highly constrained to within 1.5σ of the prior mean. This method allows us to include additional uncertainty associated with our lack of information about the dust in our sample(s), while still ensuring our two-component fit does not encounter problems with overfitting.

Our samples were selected with low SFRs and thus should have minimal radio sources at these frequencies. However if non-negligible radio contamination was present in the lower frequency bands, our two-component fit would then underestimate the tSZ signal. Meanwhile the dust fit would be either over- or under-estimated, dependent upon the radio source's spectrum into the higher bands.

Table 4.2 Two component fit parameters (from eq. 4.6) and given priors used on each catalog and radial bin.

Parameter	Description	Prior
y	Compton-y [unitless]	$[0^{\dagger},\ 4\times10^{-7}]$
$I_r(\nu_0)$	Dust Intensity [W $\mathrm{Hz}^{-1}\mathrm{m}^{-2}\mathrm{sr}^{-1}$]	$[0^{\dagger},\ 4\times10^{-23}]$
β	Dust Emissivity [unitless]	$G(1.75, 0.25^2)$
T_{d}	Dust Temperature [K]	$G(20, 3^2)$

Gaussian $G(\mu,\sigma^2)$ priors are assumed for dust emissivity $\beta = 1.75\pm0.25$, and temperature $T_{\mathrm{d}} = 20\pm3$ K. †A realistic lower limit of zero is used on the uniform free parameters unless the fit is poor and near zero. In which case, the lower limit is shifted negative to allow for accurate fitting around zero and avoid artificially inflated values.

4.4.8 Profile Fits

As detailed above, we obtain profiles for both the tSZ and dust responses per radial average bin from our frequency maps. The dominant source is expected to be a central point source associated with our target sample. However, we also expect an extended secondary profile term due to spatial correlations with neighboring galaxies.

A few different profile models could be considered, such as a generalized Navarro-Frenk-White (NFW) profile like that conducted by (Amodeo et al., 2021), or basic power-law models for two-point correlation clustering measurements (Coil et al., 2017). However, our 2.1 beam and $z \approx 1$ redshift would result in highly degenerate and correlated NFW parameter fits, while a power-law model cannot easily be forward-modeled with the beam since it diverges to infinity as $r \to 0$. As we are primarily interested in the power-law slope at radii away from the center, we opt for a simple pseudo-power-law approximation that can be made using a type of King or isothermal model (King, 1962):

$$f(r) = \frac{A_{\mathrm{k}}}{r_0}\left(1+\frac{r^2}{r_0^2}\right)^{-\frac{\gamma}{2}}, \tag{4.9}$$

with an amplitude A_{k}, comoving core radius r_0, and that now instead converges to A_{k}/r_0 as $r \to 0$. Converted to a function of projected angle (θ) through the line-of-sight, this gives

$$f(\theta) = A_{\mathrm{k}}\frac{\Gamma(\frac{1}{2})\Gamma(\frac{\gamma-1}{2})}{\Gamma(\frac{\gamma}{2})}\left(1+\frac{(D_{\mathrm{c}}\theta)^2}{r_0^2}\right)^{\frac{1-\gamma}{2}}, \tag{4.10}$$

where D_{c} is the comoving distance. This profile is best defined as a function of angle θ, as it must be convolved with the beam for accurate comparison to our measured values. For a combined model of a point source plus King ($\delta + f$) convolved with the beam (b) can be described as,

$$F(\theta) := \iint_{-\infty}^{\infty} \left[\delta(\boldsymbol{\theta}') + f(\boldsymbol{\theta}')\right] b(\boldsymbol{\theta}-\boldsymbol{\theta}')d\boldsymbol{\theta}'. \tag{4.11}$$

Our final beam as described in Section 4.4.2 is a Gaussian with FWHM= 2.1, but with an $\ell_{\text{max}} = 10,000$ cutoff. Compared to convolution with a perfect Gaussian beam this can produce a 10% difference for a central point source, but has a negligible effect on our broader King profile of eq. (4.10). For this reason we elect to assume a perfect Gaussian beam to simplify the King convolution, but maintain the exact beam (with ℓ_{max} cut) for the point source defined below as $b(\theta)$. These yield a profile function with one integral that we compute numerically,

$$F(\theta) = A_{\text{ps}} b(\theta) + \int_0^\infty \exp\left(-\frac{\theta^2 + \theta'^2}{2\sigma_{\text{beam}}^2}\right) J_0\left(i\frac{\theta\theta'}{\sigma_{\text{beam}}^2}\right) \frac{f(\theta')}{\sigma_{\text{beam}}^2} \theta' d\theta', \tag{4.12}$$

where J_0 is the Bessel function of the first kind and the size of our Gaussian beam as $\sigma_{\text{beam}} = 0.8918$.This eq. (4.12) allows us to set a lower bound for the profile's central point source component and examine the extended profile slope.

4.4.9 Dust

Table 4.3 Dust profile fit parameters for eq. (4.12), applied priors, and resultant fits for our Overlap and Wide-Area samples.

Parameter	Description	Prior	Overlap Sample	Wide-Area Sample
A_{ps} [10^{-23} W Hz^{-1}m^{-2}sr^{-1}]	Point Source Amplitude	[0, 4.0]	$2.14^{+0.24}_{-0.22}$	$2.32^{+0.22}_{-0.18}$
A_k [10^{-24} W Hz^{-1}m^{-2}sr^{-1}]	King Amplitude	[0, 4.0]	$1.38^{+0.24}_{-0.20}$	$1.56^{+0.22}_{-0.18}$
γ [unitless]	King Slope	[1.0, 4.0]	$2.60^{+0.16}_{-0.15}$	$2.95^{+0.16}_{-0.14}$
r_0 [Comoving Mpc]	Core Radius	3.0	–	–

The King amplitude and slope will be positively correlated. We set the core radius to a constant larger than the beam due to its inherent degeneracy with the amplitudes.

Our resultant dust from the two-component fit per radial bin is shown in Fig. 4.6. We observe up to a 16σ and 20σ detection of dust in the center bins of our Overlap and Wide-Area samples respectively. Beyond the beam's FWHM, detection in both cases monotonically decreases to roughly 5σ at 10 and down further to 2σ at 15.0 where noise begins to dominate. Of particular interest is the shape of our dust profile, which has a definitive central source similar to the beam along with a sloped extended signal.

We expect the dust profile to consist of an unresolved central source associated with our target galaxies, and a secondary extended profile tied to the two-point correlation function of neighboring galaxies. We fit the convolved point source plus King model of eqs. (4.10) and (4.12) to our dust profile up to 15 (≈ 15.2 comoving Mpc). This cutoff is meant to avoid incorporating low S/N radial bins and reduce any residual impact from the offset correction discussed in Section 4.4.4.

We assume fit parameters with priors as outlined in Table 4.3. As core radius (r_0) has inherent degeneracy with the amplitudes we instead hold r_0 as a constant larger than the beam, selecting $r_0 = 3.0$ comoving Mpc. Due to this degeneracy and inability to resolve our central source, this fit is not an attempt to fully separate the one- and two- component

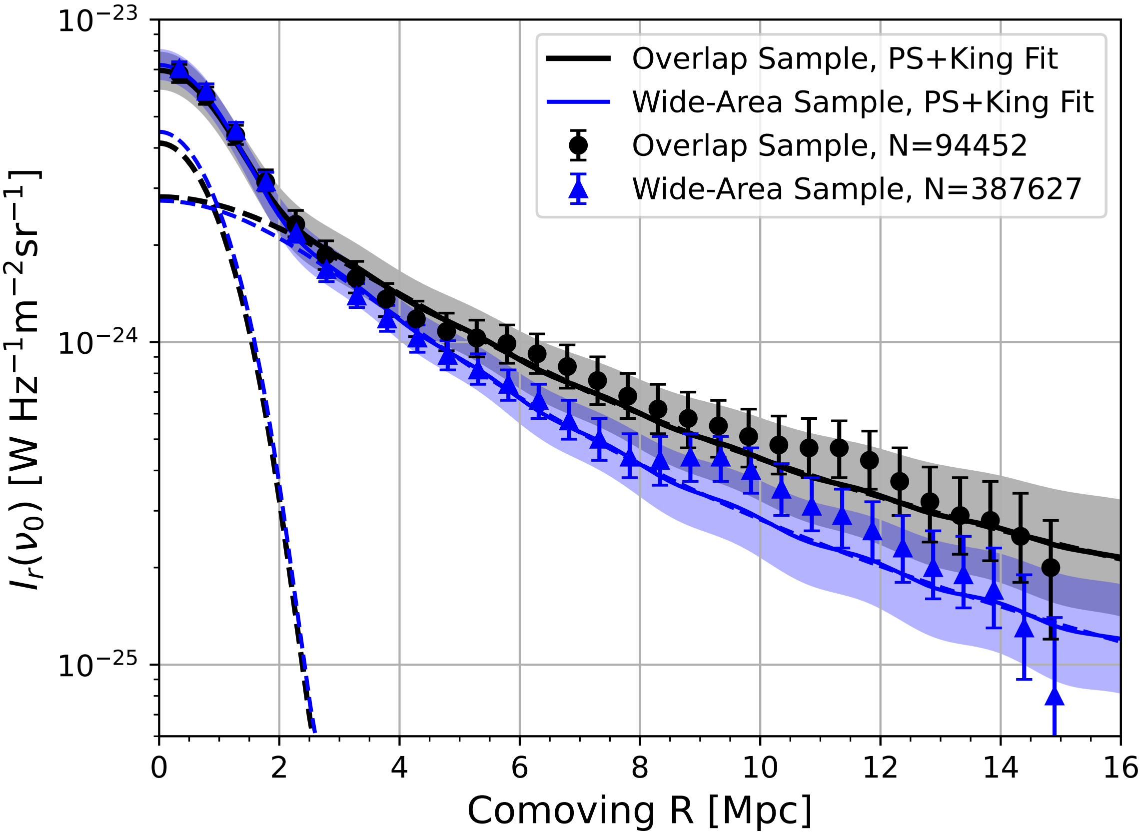

Figure 4.6 Dust radial profile and best fit point source + King model as defined in Section 4.4.9, shown here with core radius $r_0 = 3.0$ comoving Mpc for Overlap (*black*) and Wide-Area (*blue*) samples. Shaded regions represent 2σ uncertainty of the combined fit. Dashed lines correspond to the separate best fit point source and King components.

contributions within the profile. However, it provides us the opportunity to determine other characteristics such as the extended profile slope at larger radii.

The radial bin dust profile and resultant fits are shown in Fig. 4.6 for a core radius of $r_0 = 3.0$ comoving Mpc. We have separately checked the impact of different core radii. For instance, if a core radius of $r_0 = 5.0$ comoving Mpc was chosen instead, it would result in a $\approx 10\%$ increase of our dust's point source ($A_{\rm ps}$), with a $\approx 5 - 10\%$ decrease in the King ($A_{\rm k}$) amplitude. Increasing the core radius also has a noticeable effect on the King slope, due to heightened dependence on the noisier high radial bins and our limited range of 15. A core radius of $r_0 = 5.0$ comoving Mpc produces steeper dust slopes (γ) by a factor $\approx 25\%$.

Our dust profile fits are shown in Table 4.3 and Fig. 4.6 for both catalogs. The point source ($A_{\rm ps}$) and King ($A_{\rm k}$) amplitudes are fit at a $9.3 - 11.5\sigma$ and $6.2 - 7.8\sigma$ level, respectively, and are consistent (within 2σ) between galaxy samples. The best fit King slopes are $2.60^{+0.16}_{-0.15}$ and $2.95^{+0.16}_{-0.14}$ for our Overlap and Wide-Area samples. These are slightly steeper than reported power law slopes from galaxy clustering studies ($\gamma = 1.5 - 2.0$, Amvrosiadis et al., 2018; Coil et al., 2017; Eftekharzadeh et al., 2015), likely as a result of the difference between our King model and a power-law, which diverge near and below the core radius.

Since our King model is designed to level off as it nears the core radius, it would have to fit a steeper slope to be comparable with that of a power-law. Additionally, our necessary zeroing of the frequency profiles at large radii (Section 4.4.3) results in an underestimation of the dust by a small constant which would contribute to steeper slope fits. To test this, we incorporated an additional constant offset term in our profile fit and found it to be insignificant. The best fit offset was less than our measured signal at 15, within 1σ of zero, and simply increased the fit uncertainty of our other parameters while marginally decreasing the slope γ by $< 5\%$. We account for some noise underestimation from our bootstrap resampling, as discussed in Section 4.4.4, but an even further increase in noise at large radii would also primarily result in a lower signal-to-noise fit of the King slope.

Thus, we can still conclude that our extended dust has a shape consistent with that expected from the two-point correlation function of neighboring galaxies and structure. Overall, we have shown here that at our $z \approx 1$ redshifts, dust in the millimeter bands contains useful insights into intergalactic structure and can be detected at a high significance.

4.4.10 Dust Mass

Also of interest is the mean dust mass associated with our galaxy samples, which can be estimated from the rest-frame dust intensities $I_r(\nu_0)$ found from eq. (4.6). The dust mass follows,

$$M_{\rm d} = \frac{D_{\rm c}^2 \int I_r(\nu_0) d\Omega}{\kappa(\nu_0) B(\nu_0, T_{\rm d})}, \tag{4.13}$$

where $\kappa(\nu_0)$ is the dust mass opacity coefficient or absorption cross-section per unit mass [m^2 kg^{-1}] at our reference frequency of 353GHz. We take $T_d = 20 \pm 3$ K as used previously in our two-component fit. The final error is determined by standard error propagation of both $I_r(\nu_0)$ and $T_{\rm d}$.

Unfortunately $\kappa(\nu_0)$ is overall poorly constrained. Further potential uncertainty arises as $\kappa(\nu_0)$ values in literature are often derived from dust observations or models designed for the Milky Way or other local galaxies, which may slightly differ compared to our $z \approx 1$ quiescent samples. At $\nu_0 = 353$ GHz, or $\lambda_0 = 850$ μm, commonly used $\kappa(\nu_0)$ values range from $0.04 - 0.15$ m^{2}kg^{-1} (Casey, 2012; Draine, 2003; Draine & Li, 2001; Dunne et al., 2003). Thus, we take a conservative approach and assume a center value of $\kappa(\nu_0) = 0.08$ m^{2}kg^{-1}, while acknowledging this can fluctuate by a factor of two.

As evident by the previous subsection, we observe a dust profile containing both a central point source and extended neighboring structures. However, our beam introduces difficulty in accurate separation of them. As a lower bound for the expected central dust, we take the fit point source component: $\int I_r(\nu_0) d\Omega = A_{\rm ps} \int b(\theta) d\Omega$, integrated over the beam solid angle. In contrast, we also integrate within a $R = 2.0$ circular aperture instead, assuming that the central point source will dominate any extended dust structure within this radius. Our results for each catalog are shown in Table 4.4.

The lower limit to our dust mass - extracted solely from the profile's point source component ($A_{\rm ps}$) in Section 4.4.9 - indicates consistent dust masses of $8.43^{+0.10}_{-0.12}$ and $8.46^{+0.09}_{-0.12}$ $\log_{10}({\rm M}_\odot)$ for

Table 4.4 Dust mass associated with our central point source fit shown in Figure 4.6 and Table 4.3, and for all dust within $R = 2.0$. Dust-to-stellar mass ratio is also shown.

Parameter	Overlap Sample $A_{\rm ps}$	Overlap Sample $R = 2.0$	Wide-Area Sample $A_{\rm ps}$	Wide-Area Sample $R = 2.0$
$\log_{10}(M_{\rm d}/{\rm M}_\odot)$	$8.43^{+0.10}_{-0.12}$	$8.82^{+0.09}_{-0.11}$	$8.46^{+0.09}_{-0.12}$	$8.83^{+0.09}_{-0.11}$
$\log_{10}(M_{\rm d}/\overline{M_\star})$	$-2.98^{+0.10}_{-0.12}$	$-2.59^{+0.09}_{-0.11}$	$-2.98^{+0.09}_{-0.12}$	$-2.61^{+0.09}_{-0.11}$

For a $\kappa(\nu_0) = 0.08~{\rm m^2 kg^{-1}}$, which we recognize might fluctuate by a further factor of two or 0.30 dex.

Table 4.5 Compton-y profile fit parameters for eq. (4.12), given priors, and resultant fits on our Overlap and Wide-Area samples.

Parameter	Description	Prior	Overlap Sample	Wide-Area Sample
$A_{\rm ps}$ $[10^{-7}]$	Point Source Amplitude	[0, 8]	$2.0^{+1.3}_{-1.1}$	$2.2^{+0.8}_{-0.8}$
$A_{\rm k}$ $[10^{-8}]$	King Amplitude	[0, 20]	$8.2^{+5.1}_{-4.0}$	$7.4^{+2.3}_{-1.7}$
γ [unitless]	King Slope	[1.0, 10.0]	$6.6^{+2.1}_{-2.1}$	$4.1^{+0.7}_{-0.5}$
r_0 [Comoving Mpc]	Core Radius	3.0	–	–

We set the core radius to a constant larger than the beam due to its inherent degeneracy with the amplitudes.

the complete Overlap and Wide-Area samples, respectively. In comparison, an upper limit to the dust mass - simply integrating within a radius of $R = 2.0$ - produces dust masses 0.39 and 0.37 dex larger. The ratio of dust mass to stellar mass show even greater consistency between catalogs, ranging from -2.98 (lower limit using $A_{\rm ps}$) to -2.59 (upper limit using $R = 2.0$) orders of magnitude. For smaller sample sizes when profiles cannot be well-constrained, such as when binning by stellar mass, the circular $R = 2.0$ aperture is still possible. We employ this generalized method in Section 4.4.12 to analyze our dust-to-stellar mass relation.

While these dust masses are on the high side expected for galaxies with low SFRs, other studies have found similar results for massive galaxies with increasing redshift (Calura et al., 2017; Gobat et al., 2018; Santini et al., 2014). There are also indications that this increase in dust-to-stellar mass with redshift is more extreme for quiescent galaxies than dusty star-forming ones (Donevski et al., 2020; Magdis et al., 2021). The additional uncertainty from $\kappa(\nu_0)$ prevents us from drawing any strong conclusions. However, as our dust masses appear to be within an acceptable range compared to these previous studies, we can treat them as another verification of our stacking and analysis process. Determination of dust mass in this manner also highlights the potential for similar use in future sub-mm and FIR investigations.

4.4.11 Compton-y

In comparison with the dust measured above, we expect our tSZ profile to be similar but not identical in shape. Unlike dust, we expect the tSZ from our target galaxies to have a broader one-halo distribution associated with hot ionized gas, which spans throughout the CGM out to $\approx 0.5 - 1.0$ comoving Mpc. With our 2.1 FWHM beam, most of this central component will still be unresolved. We also expect a steeper profile slope, as the extended tSZ is a tracer for hot gas that is less prevalent in lower-mass neighbors.

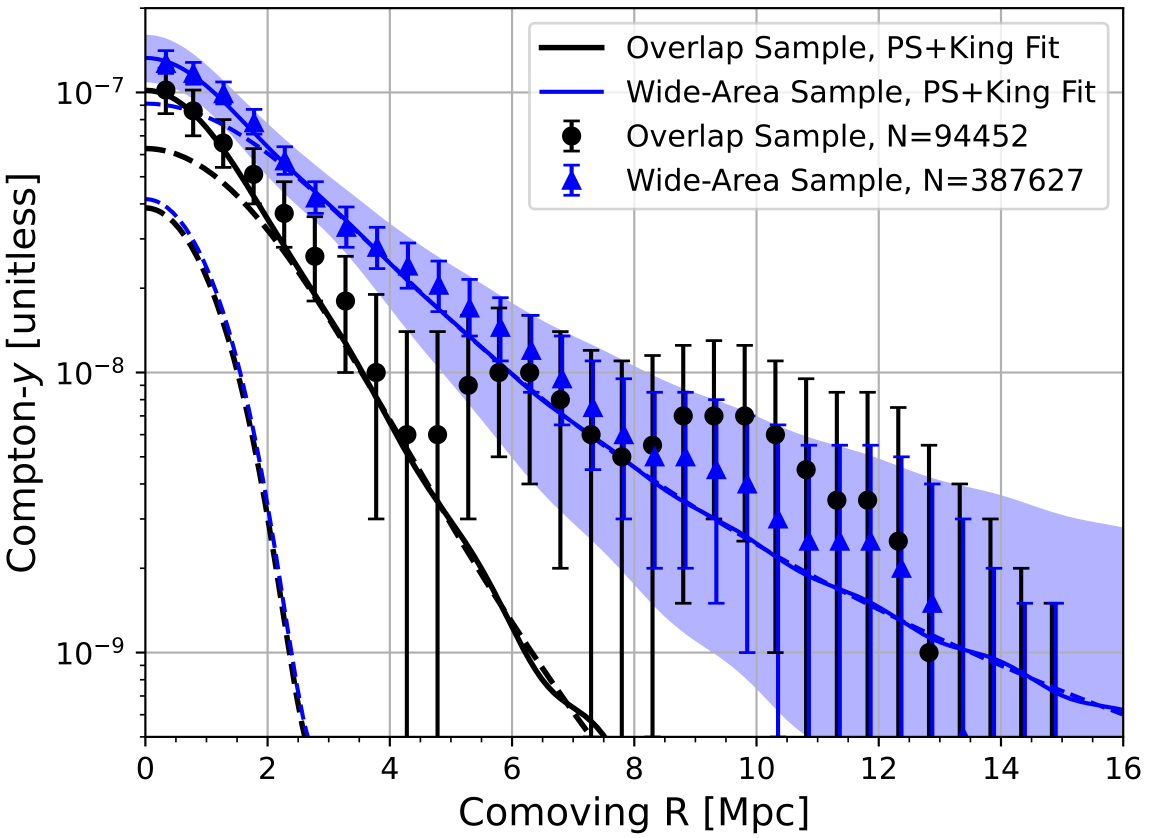

Figure 4.7 Compton-y radial profile for our quiescent galaxy catalogs; Overlap (*black, triangles*) and Wide-Area (*blue, circles*). Alongside their best fit (*solid*), shaded 2σ bounds, and individual point source and King components (*dashed*).

The Compton-y component from our two-component fit of eq. (4.6) per radial bin is shown in Fig. 4.7 for each complete catalog. Here the difference in sample size is apparent, as the centermost radial bins for Overlap Sample ($N = 94,452$) detect the tSZ at up to 5.4σ, while the Wide-Area Sample ($N = 387,627$) is up to 11σ. Of equal importance is the distance at which the S/N drops below 2σ. This occurs at a radius of 4.0 (4.0 comoving Mpc) for the Overlap Sample, versus 8.0 (8.1 comoving Mpc) for the Wide-Area Sample. So while we do observe extended tSZ larger than the beam, noise begins to dominate much quicker than observed with dust, especially for the Overlap Sample. Therefore we elect to only fit our profiles up to 10 (10.1 comoving Mpc).

We assume tSZ profile fit priors given in Table 4.5. Due to degeneracy between the central point source and King model, we assume a core radius again of $r_0 = 3.0$ comoving Mpc. It should be noted that just as with the dust, this profile fit does not fully isolate the one- and two- component contributions due to our inherent central degeneracy between the King and point source models as a result of the beam. Our main goal in applying this fit is to demonstrate the presence of extended tSZ, and compare the resultant King slope to that found for dust. We again checked the effect of using different core radii and see similar trends as with the dust; increasing core radius to $r_0 = 5.0$ comoving Mpc yields a $\approx 25\%$ increase in tSZ point source amplitude ($A_{\rm ps}$), $\leq 5\%$ decrease in King amplitude ($A_{\rm k}$), and $\approx 40\%$ increase in slope (γ). The change in slope with core radius here is larger than observed with dust, due to the faster rate at which our tSZ profile S/N drops.

Our fit results are shown in Table 4.5 and plotted alongside our measurements in Fig. 4.7. Indicative of the quick S/N drop-off, the King model for the Overlap Sample is poorly constrained. Point source amplitudes ($A_{\rm ps}$) are detected with 1.7σ and 2.8σ significance for Overlap and Wide-Area samples, respectively. They are also within 1σ of each other, showing overall consistency. The King slopes of $\gamma = 6.6^{+2.1}_{-2.1}$ and $4.1^{+0.7}_{-0.5}$ indicate a sharper decline in tSZ two-point correlation than that of dust, as possible from a nonlinear relationship between ionized gas and lower mass neighbors. An uneven presence of radio contamination in the profile's outer vs inner radius, could also increase our reported slope via tSZ fit underestimation.

4.4.12 Stellar Mass Binning

We also wish to measure the dust mass and thermal energy from our galaxies as a function of stellar mass, similar to previous studies (Greco et al., 2015; Meinke et al., 2021; Planck Collaboration: et al., 2014). Hence we no longer are concerned with a profile fit, but rather the total integrated signal over a solid angle expected to be dominated by the primary central source.

A circular top-hat aperture with radius of $R = 2.0$ is selected to integrate within, on all frequency maps per stellar mass bin. The two-component fit of eq. (4.6) is then applied to each sample and bin. Errors are calculated via bootstrap resampling from the same resample catalogs as Section 4.4.4.

We separate our catalogs into stellar mass bins with widths of 0.1 in $\log_{10}(M_\star/{\rm M}_\odot)$, over a range from $10.9 - 12.0$ and $10.8 - 12.1$ dex for our Overlap and Wide-Area samples, respectively. Additional bins were possible in the latter due to its larger number of total galaxies. The impact of bin size was checked and found to be negligible, as wider 0.2 dex-wide bins produced similar results, but created fewer points of measurement for the subsequent stellar mass uncertainty correction to be applied in Section 4.4.12.

Integrated Compton-y values are converted to thermal energies via eq. (4.3) and are shown versus stellar mass in Fig. 4.8. These align closely to the previous investigation in Meinke et al. (2021), showing a clear trend of increasing thermal energy versus stellar mass. For our mass range we expect the relation between thermal energy ($E_{\rm th}$) and stellar mass to be sufficiently described by a simple power-law model. As our analysis is conducted in terms of $\mu = \log_{10}(M_\star/{\rm M}_\odot)$, we write this energy-mass relation as a log-log model,

$$\mathcal{E}(\mu) = \log_{10}(E_{\rm th})(\mu) = \log_{10}(E_{\rm pk}) + \alpha\,(\mu - \mu_{pk})\,, \tag{4.14}$$

where α is the slope, $\mu_{pk} = \log_{10}(M_{\star,{\rm pk}}/{\rm M}_\odot)$ is the $\log_{10}$ peak stellar mass, and $E_{\rm pk}$ is the thermal energy at the peak stellar mass.

We conduct a similar analysis using the two-component fit's dust result to determine our dust mass (via Section 4.4.10) as a function of stellar mass. These are shown in Fig. 4.9. Here we again assume a log-log power-law relation,

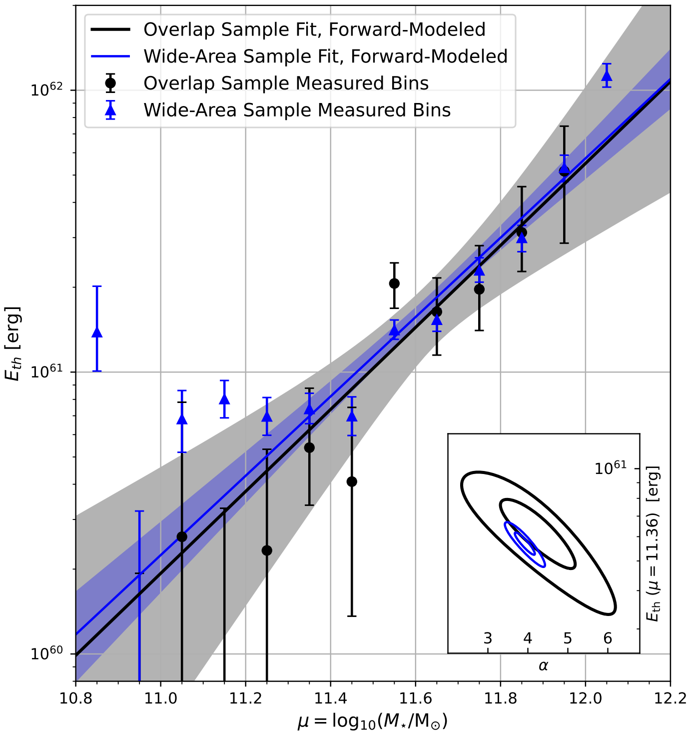

Figure 4.8 Overlap (*black, circles*) and Wide-Area (*blue, triangles*) galaxies' energy in 0.1 dex stellar mass bins with associated energy-mass fit as described in 4.6 after forward-modeling our stellar mass uncertainty (Section 4.4.12). The shaded fit regions correspond to forward-modeled 2σ levels. Inset: 1- and 2-σ bounds of the (non-forward-modeled) fit parameters $E_{\mathrm{th}}(\mu = 11.36\ \mathrm{dex})$, and slope α. We show $E_{\mathrm{th}}(\mu = 11.36\ \mathrm{dex})$ instead of E_{pk} here as the samples contain different peak masses.

$$\mathcal{M}_d(\mu) = \log_{10}(M_{\mathrm{d}})(\mu) = \log_{10}(M_{\mathrm{d,pk}}) + \alpha_{\mathrm{d}}\,(\mu - \mu_{\mathrm{pk}})\,, \tag{4.15}$$

where α_{d} is the slope, and $M_{\mathrm{d,pk}}$ is the dust mass at the peak stellar mass. Both power-law equations of eqs. (4.14) & (4.15) describe the expected relation versus stellar mass prior to any contributions that may arise from stellar mass uncertainty, discussed below.

Stellar Mass Uncertainty

The main caveat in the stellar mass bin approach is our catalogs' inherent stellar mass uncertainty. We find our SED fitting in Section 4.3 has a stellar mass uncertainty of $\sigma_{\mathrm{SED}} = 0.16$ dex, due in part from our high redshift and use of only photometric data (Meinke et al., 2021). Thus, to accurately fit measured stellar mass bins with the energy and dust mass vs stellar mass functions of eqs. (4.14) & (4.15), we must correctly incorporate our stellar mass uncertainty. Luckily our quiescent galaxy mass distributions are well fit by Gaussians of the form $G(\mu_{\mathrm{pk}}, \sigma_q^2)$, with $\sigma_q = 0.20$ dex for both and μ_{pk} listed in Table 4.6. Applying uncertainty, the average $\log_{10}$ thermal energy within a stellar mass bin centered on $\log_{10}$ mass μ_i becomes,

Table 4.6 Forward-modeled energy and dust mass versus stellar mass fits.

Catalog	μ_{pk} [$\log_{10}(M_\star/\mathrm{M}_\odot)$]	E_{pk} [10^{60}erg]	α [unitless]	$M_{\mathrm{d,pk}}$ [$10^8\mathrm{M}_\odot$]	α_{d} [unitless]
Overlap Sample	11.36	$6.45^{+1.67}_{-1.52}$	$4.04^{+0.94}_{-0.92}$	$6.23^{+0.67}_{-0.67}$	$2.59^{+0.46}_{-0.44}$
Wide-Area Sample	11.40	$8.20^{+0.52}_{-0.52}$	$3.91^{+0.25}_{-0.25}$	$6.76^{+0.56}_{-0.56}$	$2.22^{+0.35}_{-0.34}$
Meinke et al. 2021†	11.36	$5.98^{+1.02}_{-1.00}$	$3.77^{+0.60}_{-0.74}$	–	–

Our methods differ slightly from those in Meinke et al. (2021) due to changes in beam, map processing, and $S/N < 1\sigma$ cut. Dust mass was calculated from eq. (4.13) for a $\kappa(\nu_0) = 0.08\ \mathrm{m}^2\mathrm{kg}^{-1}$, which we recognize might fluctuate by a further factor of two or 0.30 dex.

$$\overline{\mathcal{E}}(E_{\mathrm{pk}}, \alpha, \mu_i) = \frac{\int_8^{15} \mathcal{E}(\mu)\ w(\mu, \mu_i)\ d\mu}{\int_8^{15} w(\mu, \mu_i)\ d\mu} \tag{4.16}$$

and similarly for average $\log_{10}$ dust mass,

$$\overline{\mathcal{M}}_d(M_{\mathrm{d,pk}}, \alpha_{\mathrm{d}}, \mu_i) = \frac{\int_8^{15} \mathcal{M}_d(\mu)\ w(\mu, \mu_i)\ d\mu}{\int_8^{15} w(\mu, \mu_i)\ d\mu}, \tag{4.17}$$

where $w(\mu, \mu_i)$ is the effective weight of a galaxy with $\log_{10}$ stellar mass μ to appear within the mass bin defined from $\mu_{i-1/2}$ to $\mu_{i+1/2}$,

$$w(\mu, \mu_i) = G(\mu - \mu_{\mathrm{pk}}, \sigma_\mu^2) \int_{\mu_{i-1/2}}^{\mu_{i+1/2}} G(\mu' - \mu, \sigma_{\mathrm{SED}}^2)\ d\mu', \tag{4.18}$$

with $\sigma_\mu^2 = \sigma_q^2 - \sigma_{\mathrm{SED}}^2$, corresponding to the standard deviation of our expected true mass distribution if no stellar mass uncertainty was present. The first Gaussian term is the weight of a galaxy selected with the true mass μ, while the integral and second Gaussian term is the chance that said galaxy actually appears in the mass bin between $\mu_{i-1/2}$ and $\mu_{i+1/2}$ due to our stellar mass uncertainty.

Equations (4.16) & (4.17) take the ideal generalized power-law functions of eqs. (4.14) & (4.15) and forward-model them into expected observations within a stellar mass bin. To clarify, this method is synonymous with the past energy-mass approach in **?**, which was not described in as much detail.

Equation (4.16) was fit to the energy-mass bins found for each catalog. We refrain from fitting any bins with $S/N < 1\sigma$ to avoid introducing spurious bias. The forward-modeled best fits and 2σ uncertainties are shown in Fig. 4.8. The inset plot shows the posterior distributions of α and $E_{\mathrm{th}}(\mu = 11.36\ \mathrm{dex})$. We display $E_{\mathrm{th}}(\mu = 11.36\ \mathrm{dex})$ instead of E_{pk} in order to compare catalogs, as they have different peak masses (μ_{pk}). Best fit values for E_{pk} and α are shown in Table 4.6, compared to previous SPT results (Meinke et al., 2021). All three catalogs show agreeing slopes (α) within 1σ, $4.04^{+0.94}_{-0.92}$ for the Overlap and $3.91^{+0.25}_{-0.25}$ for the Wide-Area Sample. These slopes uphold a strong trend of observations that indicate only CGM in the most massive galaxies and clusters produce significant levels of thermal energy (Greco et al., 2015). Some plateauing at lower stellar mass may be present as well, evident by the low mass

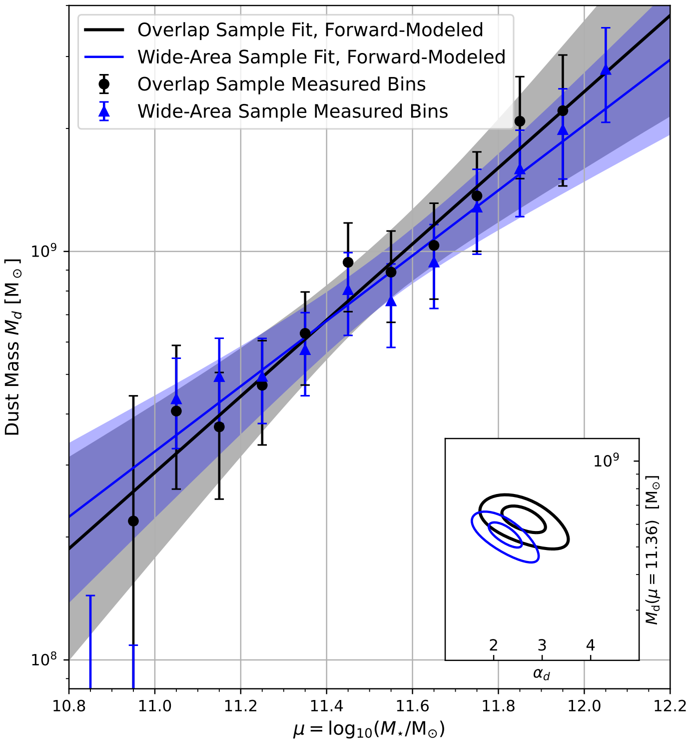

Figure 4.9 Overlap (*black, circles*) and Wide-Area (*blue, triangles*) galaxies' dust mass in 0.1 dex stellar mass bins with associated dust-stellar mass fit as in 4.6 after forward-modeling our stellar mass uncertainty (Section 4.4.12). The shaded fit regions correspond to forward-modeled 2σ levels. Inset: 1- and 2-σ bounds of the non-forward-modeled fit parameters $M_\mathrm{d}(\mu = 11.36 \text{ dex})$, α_d. We show $M_\mathrm{d}(\mu = 11.36 \text{ dex})$ instead of $M_\mathrm{d,pk}$ here as the samples contain different peak stellar masses.

bin outliers in our Wide-Area measurements. Energies at peak mass (E_pk) are also significant, at a level of 4σ for our Overlap Sample and 16σ for the Wide-Area.

In similar fashion, eq. (4.17) was fit to the measured dust versus stellar mass bins found for each catalog. We again refrain from fitting any bins with $S/N < 1\sigma$ to avoid introducing spurious bias. The forward-modeled best fits and 2σ uncertainties are shown in Fig. 4.9. The inset plot shows the posterior distributions of α_d and $M_\mathrm{d}(\mu = 11.36 \text{ dex})$. Fits for $M_\mathrm{d,pk}$ and α_d are shown in Table 4.6.

Dust mass at the peak stellar masses were detected at a 9.3σ level for the Overlap and 12σ for the Wide-Area Sample. Both catalogs show agreeing slopes (α_d) within 1σ, $2.59^{+0.46}_{-0.44}$ for Overlap and $2.22^{+0.35}_{-0.34}$ for Wide-Area. As these slopes are greater than 1, they highlight a non-linear relationship between dust and stellar mass that indicates increasingly massive quiescent galaxies have a higher dust-to-stellar mass ratio. However, this trend may only be present in the high stellar mass regime due to our narrow galaxy mass distribution.

We also consider the potential of neighboring two-halo contributions that may falsely inflate these measurements. Discussed in more detail in Meinke et al. (2021) with the same $R = 2.0$ aperture corresponding to a radius of ≈ 2.0 comoving Mpc, a central halo will be expected to dominate the tSZ signal for thermal energies exceeding $\approx 3 \times 10^{60}$ erg or halo masses larger than $\approx 10^{13} \mathrm{M}_{\odot}$. This is determined under the assumption that the gas in all neighboring halos is heated to virial temperature T_{vir}. As all our reported thermal energies with $S/N > 1\sigma$ in Fig. 4.8 reside above 3×10^{60} erg, we conclude the two-halo contribution within them are negligible compared to their respective measured uncertainties.

We also consider our dust mass measurements in Fig. 4.9 to be the expected upper limit. As discussed in Section 4.4.10, the $R = 2.0$ aperture produces a result roughly 0.30 dex greater than a separate conservative estimate via evaluation of the dust profile in Section 4.4.9. As the assumed dust mass opacity coefficient $\kappa(\nu_0) = 0.08 \ \mathrm{m}^2 \mathrm{kg}^{-1}$ contains a further factor of two or 0.30 dex uncertainty, any contributions from neighbors are likely within this uncertainty. Hence, we refrain from drawing any large conclusions aside from the relation indicated by our dust-to-stellar mass slope fit, as we expect $\kappa(\nu_0)$ to not vary significantly between our stellar mass bins.

4.4.13 Implications for AGN Feedback

Our constraints on E_{th} allow us to glean information about AGN feedback, though detailed comparisons with AGN models are best carried out alongside full numerical simulations. First, comparisons with previous work in Meinke et al. (2021) show strong similarities in their energy-mass fit. This is as expected, due to an overlap of target galaxy samples and use of SPT data. However, as before we also see significant similarities with the lower redshift ($z \approx 0.1$) results from Greco et al. (2015), even though they used locally bright galaxies as opposed to our age > 1 Gyr, $SSFR < 0.01$ Gyr^{-1}, quiescent galaxies. There are a variety of theoretical models that suggest a good match between the most massive quiescent galaxies at moderate redshifts and the central galaxies of massive halos in the nearby universe (e.g, Moster et al., 2013; Pillepich et al., 2018; Schaye et al., 2015).

Such lack of thermal energy evolution in the CGM around massive galaxies since $z \approx 1$ mirrors what occurs for the luminosity function of these galaxies (e.g. Muzzin et al., 2013; van Dokkum et al., 2010). This trend could be more indicative of radio-mode AGN feedback, where gas accretion contributes to CGM heating and radiative losses to CGM cooling. Whenever cooling surpasses heating, jets will arise that quickly push the gas up to a constant temperature and entropy at which cooling is inefficient. On the other hand, quasar models instead produce an energy input from feedback which occurs once at high redshift, heating the gas such that cooling is extremely inefficient up until today. As a result, gravitational heating will increase E_{th} without any significant mechanism to oppose it. However, specifics of this evolution are highly dependent on the history of galaxy and halo mergers between $0 < z \lesssim 1$. Hence, it is possible that some types of quasar dominated models may be compatible with our measurements.

A second major inference is the overall level of feedback. To estimate the magnitude of gravitational heating, we can assume that the gas collapses and virializes along with an encompassing spherical dark matter halo, and is heated to the virial temperature T_{vir}. This gives

$$E_{\mathrm{th,halo}}(M_{13}, z) = 1.5 \times 10^{60} \ \mathrm{erg} \ M_{13}^{5/3} \ (1+z), \tag{4.19}$$

where M_{13} is the mass of the halo in units of $10^{13} \mathrm{M}_{\odot}$ (Spacek et al., 2016). We can convert from halo mass to galaxy stellar mass using the observed relation between black hole mass and halo circular velocity for massive quiescent galaxies (Ferrarese, 2002), and the relation between black hole mass and bulge dynamical (Marconi & Hunt, 2003). As shown in Spacek et al. (2016), this gives

$$E_{\rm th,gravity}(M_\star, z) \approx 5 \times 10^{60}\ {\rm erg}\ \frac{M_\star}{10^{11}{\rm M}_\odot}\ (1+z)^{-3/2}, \tag{4.20}$$

representing the expected total thermal energy around a galaxy of stellar mass $M_\star$ ignoring both radiative cooling and feedback. For a mean redshift of $z \approx 1.1$ this yields $\approx 3.8 \times 10^{60}$ erg and $\approx 4.1 \times 10^{60}$ erg for our $M_{\star,\rm pk} = 2.29 \times 10^{11}{\rm M}_\odot$ (Overlap) and $2.51 \times 10^{11}{\rm M}_\odot$ (Wide-Area), respectively. Unfortunately this estimate has an uncertainty of about a factor of two, which is significantly larger than the uncertainty in our measurements. Regardless, these are lower than the $E_{\rm pk} = 6.45^{+1.67}_{-1.52} \times 10^{60}$ erg and $8.20^{+0.52}_{-0.52} \times 10^{60}$ erg respectively, that we found in Section 4.4.12. These suggest the presence of additional non-gravitational heating, particularly as cooling losses are not included in eq. (4.20).

To estimate quasar-mode feedback heating we use a simple model described in Scannapieco & Oh (2004), given as

$$E_{\rm th,feedback}(M_\star, z) \approx 4 \times 10^{60}\ {\rm erg}\ \epsilon_{k,0.05}\ \frac{M_\star}{10^{11}{\rm M}_\odot}\ (1+z)^{-3/2}, \tag{4.21}$$

where $\epsilon_{k,0.05}$ is the fraction of bolometric luminosity from the quasar associated with an outburst, normalized by a fiducial value of 5%, which is typical of quasar models (e.g. Costa et al., 2014; Scannapieco & Oh, 2004; Thacker et al., 2006). Taking $\epsilon_{k,0.05} = 1$ for our samples' mean redshifts and peak masses, this gives $\approx 3.0 \times 10^{60}$ erg (Overlap) and $\approx 3.3 \times 10^{60}$ erg (Wide-Area). Adding these to the contributions from $E_{\rm th,gravity}$ above gives a total energy of $\approx 6.8 \times 10^{60}$ erg and $\approx 7.4 \times 10^{60}$ erg, respectively. Including this additional energy from quasar-mode AGN feedback better matches our results of $E_{\rm pk} = 6.45^{+1.67}_{-1.52} \times 10^{60}$ erg and $8.20^{+0.52}_{-0.52} \times 10^{60}$ erg than heating from gravity alone. It also does not account for any energy losses.

Meanwhile, radio mode models are expected to fall somewhere between these two limits, with jets supplying power to roughly balance cooling processes, but never adding a large burst of additional energy near that of eq. (4.21). This would suggest values slightly below our measurements, but again with too much theoretical uncertainty to draw any definite conclusions.

A third major inference from our measurements comes from the slope of eq. (4.14), which is significantly steeper than in our simple models. This is most likely due to uncertainties in the halo-mass stellar mass relation, which are particularly large for massive $z \approx 1$ galaxies (Behroozi et al., 2019, 2010; Kravtsov et al., 2018; Lu et al., 2015; Moster et al., 2018; Wang et al., 2013). Recent studies alongside our own (Amodeo et al., 2021; Meinke et al., 2021; Schaan et al., 2021; Vavagiakis et al., 2021) make it clear that observations are now fast outpacing theoretical estimates, a major change from several years ago when only galaxy cluster sized halos were capable of being moderately detected. Future comparisons between measurements and full simulations will yield key new insights into the processes behind AGN feedback.

4.5 Discussion

Many galaxies from $z \approx 1$ to present day, starting with the most massive, undergo a process that quenches new star formation. The proposed likely culprit is feedback from accretion onto supermassive black holes, which would have a noticeable impact on the surrounding CGM. By probing the CGM for signs of heating via the redshift-independent tSZ effect, we can begin to differentiate between various AGN accretion models and provide much needed constraints for theoretical simulations.

Here we have selected $N = 387,627$ old quiescent galaxies with low SFR at $0.5 \leq z \leq 1.5$ from DES and WISE within the ACT millimeter telescope field (Wide-Area Sample). A subset of $N = 94,452$ galaxies are further used to incorporate data from SPT for an analysis across multiple instruments (Overlap Sample). These quiescent galaxies are ideal candidates to show strong heating via feedback. A detailed set of map processing (Section 4.4.2) is conducted to mitigate any systematic differences between SPT and ACT, applying a uniform 2.1 FWHM Gaussian beam across all maps that reside near 95/150/220 GHz. We then subtract a 5.0 resolution *Planck* SMICA SZ-Free CMB map to remove large-scale CMB fluctuations uncorrelated with our target galaxies.

When stacked, we observe separable dust and tSZ profiles from both galaxy catalogs. Further split into stellar mass bins, we show a clear thermal energy versus stellar mass relation influenced by our photometric uncertainty in stellar mass. Often simply discarded in tSZ analysis, we also use the dust to estimate the associated dust mass for our samples.

This work builds off of previous $z \approx 1$ quiescent galaxy stacking conducted by Meinke et al. (2021); Spacek et al. (2017). Our analysis here is enhanced from the prior via use of the recent ACT data release (Mallaby-Kay et al., 2021; Naess et al., 2020), improved map processing, and a heightened focus on the radial profile and dust mass of our target galaxies. Others have also begun a more concerted effort to analyze the galactic structure of the tSZ and kSZ (Amodeo et al., 2021; Calafut et al., 2021; Lokken et al., 2022; Schaan et al., 2021; Vavagiakis et al., 2021).

Firstly, the dust profile of our Overlap and Wide-Area galaxies produce up to 16σ and 20σ detection respectively, for radial bins with widths of 0.5. Profile detection with $S/N \geq 2\sigma$ is found out to 15 (15.2 comoving Mpc). We observe a dust profile shape for each sample indicative of a central point source associated with our galaxies and an extended profile that traces the two-point correlation function of neighboring galaxies and structure. To obtain a slope for the extended dust, we fit a point source plus King model as described in Section 4.4.8, finding slopes of $\gamma = 2.60^{+0.16}_{-0.15}$ and $2.95^{+0.16}_{-0.14}$. These are $20 - 90\%$ greater than power-law fits conducted in galaxy cluster studies ($\gamma \approx 1.5 - 2.0$, Coil et al., 2017; Eftekharzadeh et al., 2015). We attribute most of this discrepancy to a divergence between the King and power-law models when near or below our core radius of $r_0 = 3.0$ comoving Mpc.

Such dust profile analysis might also provide a novel method to constrain a catalog's intergalactic medium (IGM) and central halo mass, wherein a similar catalog of known halo mass or bias factor is used to compare two-point correlation terms traced by the observed extended dust. However a correct comparison requires careful consideration of all systematic differences in catalog selection and accurate removal of dust associated with the central source(s).

Secondly, the high S/N detection of dust allows us to convert our dust intensity fit in the $\nu_0 = 353$ GHz rest frame to a dust mass as shown in eq. (4.13). The primary difficulty in this approach is an existing uncertainty in the dust mass opacity or absorption cross-section coefficient, where we take an intermediate value of $\kappa(\nu_0) = 0.08$ m^{2}kg^{-1} while acknowledging this may vary by a factor of two (Casey, 2012; Draine, 2003; Dunne et al., 2003). We then consider reasonable lower and upper limits to isolate the dust solely associated with our central galaxies: the lower limit from the point source fit of our aforementioned profile fit, which has noted degeneracy with the King model at small radii; and an upper limit through integration within a circular aperture of $R = 2.0$ radius.

These result in a $\log_{10}$ dust mass range from $8.43^{+0.10}_{-0.12}$ to $8.82^{+0.09}_{-0.11}$ $\log_{10}(\mathrm{M}_\odot)$ for the Overlap Sample and $8.46^{+0.09}_{-0.12}$ to $8.83^{+0.09}_{-0.11}$ $\log_{10}(\mathrm{M}_\odot)$ for the Wide-Area Sample. As a dust-to-stellar mass ratio, these become $-2.98^{+0.10}_{-0.12}$ to $-2.59^{+0.09}_{-0.11}$ $\log_{10}(M_\mathrm{d}/\mathrm{M}_\star)$ and $-2.98^{+0.09}_{-0.12}$ to $-2.61^{+0.09}_{-0.11}$ $\log_{10}(M_\mathrm{d}/\mathrm{M}_\star)$, respectively. Other studies involving massive or quiescent galaxies at $z \approx 1$ have found $\log_{10}(M_\mathrm{d}/\mathrm{M}_\star) \approx -3.5$ to -2.7 (Gobat et al., 2018; Magdis et al., 2021). As our dust mass contains an additional 0.30 dex uncertainty from $\kappa(\nu_0)$, we conclude our values are in agreement, but do not draw any larger inferences. This consistency is notable however, as it echoes reports of higher dust-to-stellar mass ratios for massive galaxies at $z \approx 1$ than those at nearby lower redshifts (Magdis et al., 2021; Santini et al., 2014).

Thirdly, we inspect our tSZ radial profile and obtain a clear central detection, up to 5.4σ in our Overlap Sample and 11σ in the Wide-Area Sample. However our detection falls off much more rapidly than for dust, dropping below 2σ at 4.0 (4.0 comoving Mpc) and 8.0 (8.1 comoving Mpc), respectively. As a result compared to dust, we find steeper King slopes of $\gamma = 6.6^{+2.1}_{-2.1}$ and $4.1^{+0.7}_{-0.5}$, which indicate a sharper decline in the tSZ two-point correlation or two-halo term. This is within expectations, since the neighboring lower mass galaxies should contain reduced or cooler levels of ionized gas at a nonlinear relationship to stellar mass (Hill et al., 2018). We also note that radio contamination would produce an underestimated fit of the tSZ, while an uneven relation of radio contaminants versus radii could affect fit slopes as well. This effect is likely marginal for our redshift and frequency bands.

We also fit the tSZ point source amplitudes at 1.7σ significance for the Overlap Sample and 2.8σ for the Wide-Area Sample. These profiles and fits as shown in Fig. 4.7 indicate an extended tSZ signal. However, also evident is the inherent degeneracy between our combined point source plus King model brought about by the map resolution. This results in an inability to accurately separate the central one-halo tSZ from its two-halo counterpart and limit further detailed analysis.

Fourthly, we focused on measurements split into 0.1 dex stellar mass bins. In a more generalized approach than our profiles above, we separated the tSZ and dust integrated within a $R = 2.0$ radius circular aperture. These signals were then converted into thermal energy (eq. 4.3) and dust mass (eq. 4.13), respectively. Power-law relations were defined for both thermal energy and dust mass versus stellar mass (eqs. 4.14 & 4.15), scaled with respect to peak mass ($M_{\star,\mathrm{pk}}$) of 2.29×10^{11} $\mathrm{M}_\odot$ for Overlap and 2.51×10^{11} $\mathrm{M}_\odot$ for Wide-Area Sample. However, to accurately fit our measurements we also incorporated and forward-modeled a stellar mass uncertainty of 0.16 dex that arises from our SED fitting of photometric data.

Our thermal energy to stellar mass power-law fit produces energies of $E_\mathrm{pk} = 6.45^{+1.67}_{-1.52} \times 10^{60}$ erg for Overlap and $8.20^{+0.52}_{-0.52} \times 10^{60}$ erg for Wide-Area, at their peak mass. These values only appear inconsistent due to their different peak masses. The power-law slopes are found to be within 1σ of each other, with $\alpha = 4.04^{+0.94}_{-0.92}$ and $3.91^{+0.25}_{-0.25}$, respectively. These slopes are significantly steeper than our simple feedback models in Section 4.4.13. This can likely be attributed to model uncertainties in the halo-to-stellar mass relation for massive $z \approx 1$ galaxies (Behroozi et al., 2019; Moster et al., 2018; Wang et al., 2013). Our fits, shown in Fig. 4.8, are also consistent with the previous investigation of Meinke et al. (2021) and lower redshift measurements by Greco et al. (2015).

Meanwhile, our dust to stellar mass power-law fit produces dust masses of $M_{\mathrm{d,pk}} = 6.23^{+0.67}_{-0.67} \times 10^8$ $\mathrm{M}_\odot$ for the Overlap Sample and $6.76^{+0.56}_{-0.56} \times 10^8$ $\mathrm{M}_\odot$ for the Wide-Area Sample, at peak stellar mass. With power-law slopes of $\alpha_{\mathrm{d}} = 2.59^{+0.46}_{-0.44}$ and $2.22^{+0.35}_{-0.34}$ for the Overlap and Wide-Area samples, respectively. Our slope fits are more trustworthy than the aforementioned dust masses due to the uncertainties in dust mass opacity $\kappa(\nu_0)$ that would only scale our measurements and not affect the fit slope α_{d}. As our slopes indicate a greater than linear relation ($\alpha_{\mathrm{d}} > 1$), we conclude that massive $z \approx 1$ quiescent galaxies have an increasing dust-to-stellar mass ratio for our sample. Notably this may only be valid for our high and narrow stellar mass range.

Finally, we compare the stellar mass binned energy fit to those predicted by simple theoretical feedback models in Section 4.4.13. Our values more closely align with heating due to quasar-mode feedback rather than from gravity alone. However, both theoretical models have uncertainties of roughly a factor of two that result in the models overlapping in the same regime that our energy fit is found. Additionally, a third option of radio-mode feedback would also be situated in-between. Hence, we conclude our values are strong indicators that some form of AGN feedback is present, but the exact process and amount is unable to be determined when compared to theory. This highlights the need for improved theoretical and simulation models to keep pace with observations.

With the development of better instruments in both noise, resolution, and sky coverage, observations will continue to improve the characterization of galactic structures. We have demonstrated here that such detailed analysis at $z \approx 1$ is currently possible and will greatly benefit from improved resolution for future analysis. The latest generation of telescopes includes SPT-3G (Benson et al., 2014; Sobrin & SPT-3G Team, 2022) and TolTEC (Bryan et al., 2018; Wilson et al., 2020) which are more than capable of improving upon this work. TolTEC in particular, currently being deployed on the 50 m Large Millimeter Telescope, will grant a $\geq 5\times$ better resolution. This will enable the ability to resolve the tSZ mainly associated with the CGM and separate it from the potentially still unresolved dust which comes primarily from the underlying galaxy.

5 Conclusions

In our Universe, structures like galaxies and galaxy clusters grow hierarchically through accretion. This growth is subject to dynamic feedback processes such as stellar feedback and galactic winds on the smaller scale and magnetic and AGN feedback on the larger scale. In this doctoral thesis, we have explored various aspects of feedback processes, focusing on magnetic fields in the CGM, AGN feedback using X-ray and radio data, and AGN feedback implications through stacking Sunyaev-Zel'dovich data around galaxies. All of our studies are based on survey data, not on individual observations of specific targets. Surveys serve as fundamental tools in astrophysics in general as they supply large datasets and catalogs of celestial objects, such as stars, galaxies, clusters or quasars. On the one hand, using large datasets improve the statistics when proxies are used to determine specific properties. In this thesis we used RMs for example as a proxy to infer the magnetic field strength in the CGM (Böckmann et al., 2023a). On the other hand, large catalogs also come with the possibility to select a specified subset of targets based on specific properties. In this work we created a subset of the X-ray eRASS:1 cluster catalog to cover all clusters that are contained and also covered by the radio survey EMU (Böckmann et al., 2023b). Additionally, survey data enables the application of stacking techniques. Stacking is used to measure observables that are otherwise to weak in individual target measurements due to insufficient signal strength. In this thesis, we used survey data from the Atacama Cosmology Telescope (ACT) to perform a stacking analysis centered on massive galaxies. This approach enabled to measure the thermal Sunyaev-Zel'dovich effect around these specific galaxies (Meinke et al., 2023).

In the first presented paper Böckmann et al. (2023a), we examined the role of magnetic fields in regulating cosmic ray transport within galaxies. Given the challenges of directly observing the CGM, we employed indirect methods to investigate the physical conditions within the CGM, including magnetic field strength. Using MIGHTEE-POL data, we measured the rotation measure (RM) around foreground star-forming galaxies to derive the magnetic field strength of the CGM. We also explored correlations between the RM with redshift and the impact of the intervening galaxies along the line of sight. Our findings suggest the presence of intervening magnetic fields in the CGM, with magnetic field strengths estimated around 0.5 μG. For the first time, we statistically examined if the total numbers of intervening galaxies is related to the RM using a photometric catalog of galaxies. Our measurements suggests that only the most massive galaxy contributes to the RM and not the total number of intervenors.
RM measurements are an important tool for probing magnetic fields in the CGM of galaxies, but they come with certain challenges and should be carefully interpreted. For example, RM measurements can be influenced by the multi-phase and turbulent nature of the CGM, as it exhibits a range of physical conditions and turbulence levels, making it challenging to differentiate between the contributions of different components to the observed RM signal. Another fact that has to be taken into account is that RM measurements provide information about

the line-of-sight component of the magnetic field integrated along the entire path from the source to the observer. This leads to the fact that all magnetic fields along the line-of-sight contribute to the total measured RM, not only the magnetic field in the CGM of the studied galaxies. Also, this integration makes it difficult to infer the three-dimensional structure of the magnetic field in the CGM accurately. Despite these challenges, RM measurements are still the most important tool for studying magnetic fields in the CGM, primarily because there are currently no better alternatives. Other methods, such as direct magnetic field measurements using synchrotron emission, are generally limited to specific environments (e.g., dense interstellar medium) and are challenging to apply to the diffuse and low-density CGM. Therefore, RM measurements remain one of the most accessible and informative ways to probe magnetic fields in the CGM of galaxies of moderate to high redshifts.

An important step in RM studies is to compare observations to simulations: Advanced numerical simulations of galaxy formation and evolution can provide synthetic RM data, allowing to compare and interpret observed RMs with simulated expectations. Recently, Ramesh et al. (2023) used the TNG50 cosmological magnetohydrodynamical simulation of the IllustrisTNG project to study magnetic fields in the CGM as a follow-up work to the observational studies presented in Heesen et al. (2023) and Böckmann et al. (2023a). In this work the simulations were used to create mock observations of RM sightlines through the simulated volume and compared to observations, specifically focusing on RM as a function of azimuthal angle which is subject in Heesen et al. (2023). The authors find that the relative anisotropy, the difference between RM values along the minor and major axes, predicted by the simulation is consistent with the observations. This azimuthal anisotropy is driven by galactic feedback processes that launch strong outflows into the halo, preferentially along the minor axes of galaxies. The absolute excess that was studied in turn is smaller in the simulation compared to the observations presented in Böckmann et al. (2023a).

Also, when the effect of the cosmological IGM is included in the simulation, or when external contributions (e.g., from the host environment of the polarized source) are considered, the trend in RM vanishes within these non-local signals in their simulation. In summary, the main results regarding simulated RM in comparison to observations indicate that the simulated RM values tend to be lower than those observed in the works of Heesen et al. (2023) and Böckmann et al. (2023a). On the one hand this discrepancy could arise from the implemented mechanisms that are used to compute the RMs in the simulations or on the other hand the measured RM values in the observational works could be due to additional mechanisms that are not yet understood. Additionally, Ramesh et al. (2023) studied the difference of star-forming and quiescent galaxies in terms of magnetic fields finding higher RM values in higher SFR galaxies. This difference is interpreted as higher SFR galaxies launching stronger galactic-scale outflows which drives more magnetized gas into the CGM. The difference of RM in star-forming and quiescent also shows that magnetic fields in the CGM include information about galactic feedback processes. Future large surveys such as POSSUM (with the ASKAP teleskcope), and SKA in combination with high resolution simulations will enable studies focusing especially on this topic. Future radio telescopes and instruments will provide large-scale radio surveys leading to more RM data. An increase in measurements will improve the statistics of properties and distribution of magnetic fields in different environments.

In the second paper Böckmann et al. (2023b), we investigated AGN feedback mechanisms by analyzing the properties of central radio galaxies hosted in galaxy clusters. A central subject of this work was the cluster catalog based on the first sky-scan from the X-ray telescope eROSITA. During the time of my phD I was also an active member of the eROSITA cluster working group and contributed to the catalog creation by detecting for example false cluster candidates during my analysis. Therefore I am also a co-author on the paper that accompanies the release of the eRASS:1 catalog Bulbul et al., in prep..

Using the eROSITA eRASS:1 cluster catalog and the ASKAP pilot survey EMU, we examined the relationships between X-ray luminosities of a cluster to the radio luminosities of the corresponding BCG, BCG offset from the cluster center, radio source size, and other cluster characteristics. Our study revealed several significant correlations, such as the link between BCG offset and cluster dynamical state, as well as the association between radio and X-ray luminosities. We find a statistically significant correlation between the radio and the X-ray luminosity, as in previous works. We also observed an anti-correlation between the central cooling time and radio luminosity, indicating that more powerful AGN are present in clusters with shorter cooling times. Additionally, we highlighted the role of cluster types, distinguishing between cool-core and non-cool-core clusters, in hosting powerful radio sources. We find that cool-core clusters tend to host more luminous radio sources. This confirms that cool-core clusters always host a powerful radio-mode AGN.

In this work we investigated ~ 70 targets. The relatively small number and the inhomogenous sample introduce a high scatter in all correlations we derived. However, this study is based on introductory observations of eROSITA and ASKAP: eRASS1 and the EMU pilot field 1. eROSITA, for instance, has subsequently fulfilled 4 whole-sky scans resulting in the forthcoming eRASS:4 survey, which enables a more in-depth exploration of the X-ray sky. Also, the EMU pilot field 2 has already been finished, coming with a larger field of view and enhanced depth. Unfortunately, the German sky of the eROSITA mission does not include the area of the EMU pilot field 2 due to its location in the northern celestial hemisphere, with German eROSITA only accessible to the southern sky. Nevertheless, forthcoming radio surveys covering larger fields also in the southern celestial hemisphere will yield data of more radio galaxies within eRASS clusters. Also, deeper data will enable to detect fainter radio galaxies which, on the one hand results in more detections but also a larger variety in radio magnitudes which will result in reduced scatter and more significant statistics.

In the third paper Meinke et al. (2023), we explored the impact of AGN feedback on the CGM by stacking SZ data around massive, quiescent galaxies at moderate redshifts ($0.5 \leq z \leq 1.5$) using data from the Atacama Cosmology Telescope among other surveys. We detected significant dust and thermal Sunyaev-Zel'dovich signal around these quiescent galaxies. The dust signal is detected with high signal-to-noise ratios (up to 20σ) and exhibits a unique profile, suggesting the presence of central point sources and extended emission correlated with neighboring galaxies. Using the dust signal, we estimated the dust mass associated with these galaxies, which falls within a range consistent with previous studies. This indicates that quiescent galaxies at moderate redshifts possess a noticeable amount of dust, despite their low star formation rates.

The tSZ signal is obtained by stacking ACT data around 387.627 quiescent galaxies. We use stacking due to the low halo mass of galaxies in contrast to clusters where the tSZ signal can be detected in individual halos. In the case of galaxy clusters, stacking is therefore not required because clusters are more massive structures containing large amounts of hot gas. The cumulative tSZ effect from the entire cluster is much stronger and detectable without stacking. Observations of clusters benefit from their high mass and gas content, making the tSZ signal relatively bright and allowing for direct detection without the need for stacking.

Another reason to use stacking is the noise: When observing the tSZ signal around individual galaxies, the signal is relatively weak compared to the noise inherent in astronomical observations. This low SNR makes it challenging to detect the tSZ signal directly for each galaxy. Stacking allows to boost the SNR by averaging the tSZ signals of multiple galaxies that are expected to have a similar tSZ effect. By stacking these signals, the noise decreases and the tSZ signal becomes more prominent, making it easier to detect.

Nonetheless, stacking also induces problems. On the one hand stacking relies on the assumption that the properties of the objects being stacked are consistent so special attention needs to be drawn to creating a catalogs with targets that are stacked. Any systematic differences or biases between the objects in the stack can lead to erroneous results. On the other hand stacking can be susceptible to contamination from foreground objects or sources, especially in crowded regions of the sky. These foreground sources can add noise to the stacked signal or affect the interpretation of the stacked signal. In addition, stacking may inadvertently include unrelated sources or contaminants in the stacked signal, which can distort the interpretation of the results.

In the present work, the tSZ signal that we detected by stacking exhibits a steeper radial profile compared to the dust signal. This suggests a rapid decline in the tSZ two-point correlation, likely due to the reduced or cooler ionized gas in the neighboring lower mass galaxies. This observation is consistent with the influence of AGN feedback on the CGM. We also discuss the implications of our findings for AGN feedback models. The lack of thermal energy evolution in the CGM of massive galaxies since $z \approx 1$ supports the idea that radio-mode AGN feedback, where gas accretion contributes to CGM heating, may be at play. Quasar-dominated models are less consistent with our measurements. At last we estimate the magnitude of gravitational heating and quasar-mode AGN feedback heating and find that the latter better matches our observations, indicating the presence of additional non-gravitational heating processes in the CGM of these galaxies. However, precise determination of the feedback process and magnitude remained challenging due to uncertainties and theoretical model limitations.

This thesis covered diverse topics regarding feedback processes in galaxies to clusters. We examined thermal as well as non-thermal emission, the interplay between magnetic fields and the CGM, the influence of AGN feedback in galaxy clusters and the implications of this feedback on structure growth. Throughout all project carried out in this thesis we find discrepancies of our observational data with simulation data. This collectively emphasizes the need for continued advancements in observational techniques, theoretical modeling in terms of numerical simulations and larger datasets to improve our understanding of these complex feedback processes that shape the growth of structure in the Universe.

6 Acknowledgements

Since I was a little child I was fascinated by Physics and especially Astronomy and therefore it was always my dream to become a scientist (after I realized becoming an astronaut was a bit unrealistic). I want to thank all the people that accompanied me along the way to become a "real" astrophysicist with a doctoral degree.

First of all I want to thank my supervisor Marcus who gave me the opportunity to write not only my Bachelor and Master Thesis at the extragalactic group at the observatory but also sent me to Arizona for an internship at ASU and eventually hired me to work on my phD thesis under his supervision. I also want to thank all my other colleges, especially Jörg and Volker among all others from the observatory that I got to know during the last 6 years. I really enjoyed being part of the observatory family and all the activities we did.

I also want to thank my other second family, my friends that I met during my physics studies: Andras, Ali, Thomas and Henrik with the last one even being my college up until today, which we both enjoyed very much. It was really nice to have one of my best friends also as a working buddy. You all really helped me to keep up also when I struggled and I enjoyed our -sometimes- late night random discussions about quantum mechanics and astrophysics among different topics. Also I want to thank of course my boyfriend Ulf who was always very supportive, now I finally caught up on you with my degree.

Last but not least I want to thank my actual family and especially my parents who even supported me when I changed my study plans from mechanical engineering to physics. I am deeply sad that the person who has probably influenced me the most, my father, misses my big achievement as he already passed away. I want to dedicate this thesis to him.

7 Bibliography

Abbott, T. M. C., Abdalla, F. B., Allam, S., et al. 2018, The Astrophysical Journal Supplement Series, 239, 18

Addison, G. E., Dunkley, J., & Bond, J. R. 2013, Monthly Notices of the Royal Astronomical Society, 436, 1896

Aihara, H., Arimoto, N., Armstrong, R., et al. 2018, , 70, S4

Akahori, T., Ryu, D., & Gaensler, B. M. 2016, , 824, 105

Amodeo, S., Battaglia, N., Schaan, E., et al. 2021, , 103, 063514

Amvrosiadis, A., Eales, S. A., Negrello, M., et al. 2018, , 475, 4939

Anand, A., Nelson, D., & Kauffmann, G. 2021, , 504, 65

Anderson, M. E. & Bregman, J. N. 2010, , 714, 320

Anderson, M. E., Bregman, J. N., & Dai, X. 2013, , 762, 106

Anderson, M. E., Churazov, E., & Bregman, J. N. 2016, , 455, 227

Anderson, M. E., Gaspari, M., White, S. D. M., Wang, W., & Dai, X. 2015, Monthly Notices of the Royal Astronomical Society, 449, 3806–3826

Arámburo-García, A., Bondarenko, K., Boyarsky, A., et al. 2023, , 519, 4030

Arnaud, M., Rothenflug, R., Boulade, O., Vigroux, L., & Vangioni-Flam, E. 1992, , 254, 49

Assef, R. J., Kochanek, C. S., Brodwin, M., et al. 2010, The Astrophysical Journal, 713, 970–985

Assef, R. J., Stern, D., Noirot, G., et al. 2018, The Astrophysical Journal Supplement Series, 234, 23

Aumer, M., White, S. D. M., Naab, T., & Scannapieco, C. 2013, , 434, 3142

Baldi, R. D., Capetti, A., & Giovannini, G. 2015, Astronomy Astrophysics, 576, A38

Basu, A., Mao, S. A., Fletcher, A., et al. 2018, , 477, 2528

Basu, A., Wadadekar, Y., Beelen, A., et al. 2015, , 803, 51

Battaglia, N., Bond, J. R., Pfrommer, C., & Sievers, J. L. 2013, , 777, 123

Battaglia, N., Bond, J. R., Pfrommer, C., Sievers, J. L., & Sijacki, D. 2010, , 725, 91

Beattie, J. R., Federrath, C., Kriel, N., Mocz, P., & Seta, A. 2023, , 524, 3201

Beck, R. 2015, , 24, 4

Beck, R., Brandenburg, A., Moss, D., Shukurov, A., & Sokoloff, D. 1996, , 34, 155

Behroozi, P., Wechsler, R. H., Hearin, A. P., & Conroy, C. 2019, , 488, 3143

Behroozi, P. S., Conroy, C., & Wechsler, R. H. 2010, , 717, 379

Benson, B. A., Ade, P. A. R., Ahmed, Z., et al. 2014, 9153, 91531P

Bernet, M. L., Miniati, F., & Lilly, S. J. 2010, , 711, 380

Bernet, M. L., Miniati, F., & Lilly, S. J. 2012, , 761, 144

Bernet, M. L., Miniati, F., & Lilly, S. J. 2013, , 772, L28

Bernet, M. L., Miniati, F., Lilly, S. J., Kronberg, P. P., & Dessauges-Zavadsky, M. 2008, , 454, 302

Berta, S., Lutz, D., Genzel, R., Förster-Schreiber, N. M., & Tacconi, L. J. 2016, , 587, A73

Best, P. N., von der Linden, A., Kauffmann, G., Heckman, T. M., & Kaiser, C. R. 2007, , 379, 894

Bharadwaj, V., Reiprich, T. H., Schellenberger, G., et al. 2014, , 572, A46

Birkinshaw, M. 1999, , 310, 97

Bîrzan, L., McNamara, B. R., Nulsen, P. E. J., Carilli, C. L., & Wise, M. W. 2008, , 686, 859

Bîrzan, L., Rafferty, D. A., Brüggen, M., et al. 2020, , 496, 2613

Birzan, L., Rafferty, D. A., McNamara, B. R., Wise, M. W., & Nulsen, P. E. J. 2004, The Astrophysical Journal, 607, 800–809

Blanton, M. R. & Moustakas, J. 2009, , 47, 159

Böckmann, K., Brüggen, M., Heesen, V., et al. 2023a, arXiv e-prints, arXiv:2308.11391

Böckmann, K., Brüggen, M., Koribalski, B., et al. 2023b, arXiv e-prints, arXiv:2307.13672

Bocquet, S., Dietrich, J. P., Schrabback, T., et al. 2019, The Astrophysical Journal, 878, 55

Bonafede, A., Cassano, R., Brüggen, M., et al. 2017, Monthly Notices of the Royal Astronomical Society, 470, 3465–3475

Bond, J. R., Kofman, L., & Pogosyan, D. 1996, Nature, 380, 603–606

Bower, R. G., Benson, A. J., Malbon, R., et al. 2006, , 370, 645

Brammer, G. B., van Dokkum, P. G., & Coppi, P. 2008, , 686, 1503

Bregman, J. N., Anderson, M. E., Miller, M. J., et al. 2018, The Astrophysical Journal, 862, 3

Bregman, J. N., Hodges-Kluck, E., Qu, Z., et al. 2022, , 928, 14

Brownson, S., Maiolino, R., Tazzari, M., Carniani, S., & Henden, N. 2019, , 490, 5134

Brunner, H., Liu, T., Lamer, G., et al. 2022, , 661, A1

Bruzual, G. & Charlot, S. 2003, , 344, 1000

Bryan, S., Austermann, J., Ferrusca, D., et al. 2018, 10708, 107080J

Buote, D. A. & Tsai, J. C. 1995, , 452, 522

Burn, B. J. 1966, , 133, 67

Butsky, I. S., Fielding, D. B., Hayward, C. C., et al. 2020, , 903, 77

Calafut, V., Gallardo, P. A., Vavagiakis, E. M., et al. 2021, , 104, 043502

Calura, F., Pozzi, F., Cresci, G., et al. 2017, , 465, 54

Calzetti, D. 2013, 419

Carlstrom, J. E., Holder, G. P., & Reese, E. D. 2002, , 40, 643

Carretti, E., O'Sullivan, S. P., Vacca, V., et al. 2023, , 518, 2273

Casey, C. M. 2012, , 425, 3094

Cassano, R., Ettori, S., Giacintucci, S., et al. 2010, The Astrophysical Journal, 721, L82–L85

Cattaneo, A., Faber, S. M., Binney, J., et al. 2009, , 460, 213

Cavagnolo, K. W., McNamara, B. R., Nulsen, P. E. J., et al. 2010, The Astrophysical Journal, 720, 1066–1072

Chamberlain, C., Arav, N., & Benn, C. 2015, , 450, 1085

Chartas, G., Brandt, W. N., Gallagher, S. C., & Proga, D. 2007, , 133, 1849

Chatterjee, S., Ho, S., Newman, J. A., & Kosowsky, A. 2010, , 720, 299

Chaves-Montero, J., Hernández-Monteagudo, C., Angulo, R. E., & Emberson, J. D. 2020, Monthly Notices of the Royal Astronomical Society, 503, 1798–1814

Chisholm, J., Tremonti, C., & Leitherer, C. 2018, , 481, 1690

Chiu, I. N., Ghirardini, V., Liu, A., et al. 2022, , 661, A11

Chown, R., Omori, Y., Aylor, K., et al. 2018, The Astrophysical Journal Supplement Series, 239, 10

Churazov, E., Brüggen, M., Kaiser, C. R., Böhringer, H., & Forman, W. 2001, , 554, 261

Coil, A. L., Mendez, A. J., Eisenstein, D. J., & Moustakas, J. 2017, , 838, 87

Coleman, G. D., Wu, C. C., & Weedman, D. W. 1980, , 43, 393

Comparat, J., Truong, N., Merloni, A., et al. 2022, arXiv e-prints, arXiv:2201.05169

Condon, J. J., Cotton, W. D., & Broderick, J. J. 2002, , 124, 675

Costa, T., Sijacki, D., & Haehnelt, M. G. 2014, , 444, 2355

Cowie, L. L., Songaila, A., Hu, E. M., & Cohen, J. G. 1996, , 112, 839

Crichton, D., Gralla, M. B., Hall, K., et al. 2016, , 458, 1478

Croton, D. J., Springel, V., White, S. D. M., et al. 2006, , 365, 11

Dabhade, P., Röttgering, H. J. A., Bagchi, J., et al. 2020, Astronomy Astrophysics, 635, A5

Danforth, C. W. & Shull, J. M. 2008, , 679, 194

Davies, J. J., Crain, R. A., Oppenheimer, B. D., & Schaye, J. 2020, , 491, 4462

Davies, L. J. M., Robotham, A. S. G., Driver, S. P., et al. 2018, , 480, 768

de Gouveia Dal Pino, E. M., Clavijo-Bohórquez, W., & Melioli, C. 2020, in Perseus in Sicily: From Black Hole to Cluster Outskirts, ed. K. Asada, E. de Gouveia Dal Pino, M. Giroletti, H. Nagai, & R. Nemmen, Vol. 342, 229–233

de Graaff, A., Cai, Y.-C., Heymans, C., & Peacock, J. A. 2019, Astronomy Astrophysics, 624, A48

de Kool, M., Arav, N., Becker, R. H., et al. 2001, , 548, 609

De Propris, R., West, M. J., Andrade-Santos, F., et al. 2021, , 500, 310

DeFelippis, D., Bouché, N. F., Genel, S., et al. 2021, The Astrophysical Journal, 923, 56

Dodelson, S. & Efstathiou, G. 2004, Physics Today, 57, 60

Dolag, K., Komatsu, E., & Sunyaev, R. 2016, , 463, 1797

Donahue, M. & Voit, G. M. 2022a, arXiv e-prints, arXiv:2204.08099

Donahue, M. & Voit, G. M. 2022b, , 973, 1

Donevski, D., Lapi, A., Małek, K., et al. 2020, , 644, A144

Draine, B. T. 2003, , 41, 241

Draine, B. T. 2011, Physics of the Interstellar and Intergalactic Medium

Draine, B. T. & Li, A. 2001, , 551, 807

Driver, S. 2021, Nature Astronomy, 5, 852

Drory, N. & Alvarez, M. 2008, , 680, 41

Dunn, J. P., Bautista, M., Arav, N., et al. 2010, , 709, 611

Dunne, L., Eales, S., Ivison, R., Morgan, H., & Edmunds, M. 2003, , 424, 285

Dutton, A. A. & van den Bosch, F. C. 2012, , 421, 608

Eftekharzadeh, S., Myers, A. D., White, M., et al. 2015, , 453, 2779

Fabian, A. 2012, Annual Review of Astronomy and Astrophysics, 50, 455–489

Fabian, A. C. 2012, , 50, 455

Farnes, J. S., O'Sullivan, S. P., Corrigan, M. E., & Gaensler, B. M. 2014, , 795, 63

Ferrarese, L. 2002, , 578, 90

Ferrière, K., West, J. L., & Jaffe, T. R. 2021, , 507, 4968

Feruglio, C., Maiolino, R., Piconcelli, E., et al. 2010, , 518, L155

Fielding, D., Quataert, E., & Martizzi, D. 2018, , 481, 3325

Fielding, D. B., Tonnesen, S., DeFelippis, D., et al. 2020, , 903, 32

Fletcher, A., Beck, R., Shukurov, A., Berkhuijsen, E. M., & Horellou, C. 2011, , 412, 2396

Gaspari, M., Tombesi, F., & Cappi, M. 2020, Nature Astronomy, 4, 10

Gatto, A., Walch, S., Low, M. M. M., et al. 2015, , 449, 1057

Gatto, A., Walch, S., Naab, T., et al. 2017, , 466, 1903

Gibson, B. K., Pilkington, K., Brook, C. B., Stinson, G. S., & Bailin, J. 2013, , 554, A47

Gitti, M., Brighenti, F., & McNamara, B. R. 2012, Advances in Astronomy, 2012, 1–24

Gobat, R., Daddi, E., Magdis, G., et al. 2018, Nature Astronomy, 2, 239

Godfrey, L. E. H. & Shabala, S. S. 2016, , 456, 1172

Gralla, M. B., Crichton, D., Marriage, T. A., et al. 2014, , 445, 460

Granato, G. L., De Zotti, G., Silva, L., Bressan, A., & Danese, L. 2004, , 600, 580

Greco, J. P., Colin Hill, J., Spergel, D. N., & Battaglia, N. 2015, The Astrophysical Journal, 808, 151

Greco, J. P., Hill, J. C., Spergel, D. N., & Battaglia, N. 2015, , 808, 151

Greene, J. E., Pooley, D., Zakamska, N. L., Comerford, J. M., & Sun, A.-L. 2014, , 788, 54

Gupta, A., Mathur, S., Krongold, Y., Nicastro, F., & Galeazzi, M. 2012, , 756, L8

Guzman, J., Whiting, M., Voronkov, M., et al. 2019, ascl:1912.003

Hafen, Z., Faucher-Giguère, C.-A., Anglés-Alcázar, D., et al. 2019, Monthly Notices of the Royal Astronomical Society, 488, 1248

Hamer, S. L., Edge, A. C., Swinbank, A. M., et al. 2016, , 460, 1758

Hammond, A. M., Robishaw, T., & Gaensler, B. M. 2012, arXiv e-prints, arXiv:1209.1438

Hand, N., Appel, J. W., Battaglia, N., et al. 2011, , 736, 39

Hardcastle, M. J. 2018, Monthly Notices of the Royal Astronomical Society, 475, 2768

Hardcastle, M. J., Williams, W. L., Best, P. N., et al. 2019, Astronomy Astrophysics, 622, A12

Harrison, C. M., Alexander, D. M., Mullaney, J. R., & Swinbank, A. M. 2014, , 441, 3306

Hatfield, P. W., Jarvis, M. J., Adams, N., et al. 2022, , 513, 3719

Heald, G. 2009, 259, 591

Heckman, T. M., Alexandroff, R. M., Borthakur, S., Overzier, R., & Leitherer, C. 2015, , 809, 147

Heckman, T. M. & Best, P. N. 2014, Annual Review of Astronomy and Astrophysics, 52, 589–660

Heesen, V., O'Sullivan, S. P., Brüggen, M., et al. 2023, , 670, L23

Heywood, I., Jarvis, M. J., Hale, C. L., et al. 2022, , 509, 2150

Hill, J. C., Baxter, E. J., Lidz, A., Greco, J. P., & Jain, B. 2018, , 97, 083501

Hilton, M., Hasselfield, M., Sifón, C., et al. 2018, , 235, 20

Hlavacek-Larrondo, J., Fabian, A. C., Edge, A. C., et al. 2012, , 421, 1360

Hogan, M. T., Edge, A. C., Hlavacek-Larrondo, J., et al. 2015, , 453, 1201

Hojjati, A., Tröster, T., Harnois-Déraps, J., et al. 2016, ArXiv e-prints [[arXiv]1608.07581]

Hopkins, A. M., Whiting, M. T., Seymour, N., et al. 2015, Publications of the Astronomical Society of Australia, 32

Hopkins, P. F. 2014, in American Astronomical Society Meeting Abstracts, Vol. 224, American Astronomical Society Meeting Abstracts #224, 215.06

Hotan, A. W., Bunton, J. D., Chippendale, A. P., et al. 2021, , 38, e009

Hu, C.-Y. 2019, , 483, 3363

Hudson, D. S., Mittal, R., Reiprich, T. H., et al. 2010, , 513, A37

Hummels, C. B., Bryan, G. L., Smith, B. D., & Turk, M. J. 2013, , 430, 1548

Hummels, C. B., Smith, B. D., Hopkins, P. F., et al. 2019, , 882, 156

HyeongHan, K., Jee, M. J., Rudnick, L., et al. 2020, , 900, 127

Jarvis, M., Taylor, R., Agudo, I., et al. 2016, in MeerKAT Science: On the Pathway to the SKA, 6

Jarvis, M. J., Häußler, B., & McAlpine, K. 2013, The Messenger, 154, 26

Johnston, S., Taylor, R., Bailes, M., et al. 2008, Experimental Astronomy, 22, 151

Kacprzak, G. G., Churchill, C. W., Steidel, C. C., & Murphy, M. T. 2008, , 135, 922

Keating, L. C., Haehnelt, M. G., Becker, G. D., & Bolton, J. S. 2014, , 438, 1820

Kim, C.-G. & Ostriker, E. C. 2018, , 853, 173

Kim, K. S., Lilly, S. J., Miniati, F., et al. 2016, , 829, 133

King, I. 1962, , 67, 471

Kinney, A. L., Calzetti, D., Bohlin, R. C., et al. 1996, , 467, 38

Kolokythas, K., O'Sullivan, E., Raychaudhury, S., et al. 2018, , 481, 1550

Koribalski, B. S. 2022, in 2022 3rd URSI Atlantic and Asia Pacific Radio Science Meeting (AT-AP-RASC), 1–4

Kormendy, J. 2016, in Astrophysics and Space Science Library, Vol. 418, Galactic Bulges, ed. E. Laurikainen, R. Peletier, & D. Gadotti, 431

Kravtsov, A. V. & Borgani, S. 2012, , 50, 353

Kravtsov, A. V., Vikhlinin, A. A., & Meshcheryakov, A. V. 2018, Astronomy Letters, 44, 8

Kronberg, P. P., Bernet, M. L., Miniati, F., et al. 2008, , 676, 70

Kronberg, P. P. & Perry, J. J. 1982, , 263, 518

Krumholz, M. R. 2015, arXiv e-prints, arXiv:1511.03457

Kudritzki, R.-P. & Puls, J. 2000, , 38, 613

Labbé, I., van Dokkum, P., Nelson, E., et al. 2023, , 616, 266

Lacy, M., Mason, B., Sarazin, C., et al. 2019, , 483, L22

LaMassa, S. M., Georgakakis, A., Vivek, M., et al. 2019, The Astrophysical Journal, 876, 50

Lan, T.-W. & Prochaska, J. X. 2020, , 496, 3142

Lansbury, G. B., Jarvis, M. E., Harrison, C. M., et al. 2018, , 856, L1

Lehner, N., Wotta, C. B., Howk, J. C., et al. 2018, , 866, 33

Li, J.-T., Bregman, J. N., Wang, Q. D., Crain, R. A., & Anderson, M. E. 2018, , 855, L24

Li, J.-T., Bregman, J. N., Wang, Q. D., et al. 2017, , 233, 20

Li, M. & Bryan, G. L. 2020, , 890, L30

Lin, Y.-T. & Mohr, J. J. 2004, , 617, 879

Lin, Y.-T., Mohr, J. J., & Stanford, S. A. 2003, , 591, 749

Liu, A., Bulbul, E., Ghirardini, V., et al. 2022, , 661, A2

Lochhaas, C., Bryan, G. L., Li, Y., Li, M., & Fielding, D. 2020, , 493, 1461

Lokken, M., Hložek, R., van Engelen, A., et al. 2022, , 933, 134

Lu, Z., Mo, H. J., Lu, Y., et al. 2015, , 450, 1604

Machado, R. E. G., Tissera, P. B., Lima Neto, G. B., & Sodré, L. 2018, , 609, A66

Macquart, J. P., Prochaska, J. X., McQuinn, M., et al. 2020, , 581, 391

Maddox, N., Frank, B. S., Ponomareva, A. A., et al. 2021, , 646, A35

Magdis, G. E., Gobat, R., Valentino, F., et al. 2021, , 647, A33

Magliocchetti, M. & Brüggen, M. 2007, , 379, 260

Main, R. A., McNamara, B. R., Nulsen, P. E. J., Russell, H. R., & Vantyghem, A. N. 2017, , 464, 4360

Mainzer, A., Bauer, J., Grav, T., et al. 2011, , 731, 53

Mallaby-Kay, M., Atkins, Z., Aiola, S., et al. 2021, , 255, 11

Mao, S. A., Carilli, C., Gaensler, B. M., et al. 2017, Nature Astronomy, 1, 621

Marconi, A. & Hunt, L. K. 2003, , 589, L21

Marconi, A., Risaliti, G., Gilli, R., et al. 2004, , 351, 169

Marshall, M. A., Shabala, S. S., Krause, M. G. H., et al. 2018, , 474, 3615

Martin, C. L., Shapley, A. E., Coil, A. L., et al. 2012, , 760, 127

Mauch, T. & Sadler, E. M. 2007, , 375, 931

McCarthy, I. G., Le Brun, A. M. C., Schaye, J., & Holder, G. P. 2014, , 440, 3645

McConnell, N. J. & Ma, C.-P. 2013, , 764, 184

McDonald, M., Gaspari, M., McNamara, B. R., & Tremblay, G. R. 2018, , 858, 45

McGaugh, S. S., Schombert, J. M., de Blok, W. J. G., & Zagursky, M. J. 2010, , 708, L14

McNamara, B. R. & Nulsen, P. E. J. 2012, New Journal of Physics, 14, 055023

McNamara, B. R., Nulsen, P. E. J., Wise, M. W., et al. 2005, , 433, 45

McNamara, B. R., Russell, H. R., Nulsen, P. E. J., et al. 2016a, , 830, 79

McNamara, B. R., Russell, H. R., Nulsen, P. E. J., et al. 2016b, , 830, 79

McNamara, B. R., Wise, M., Nulsen, P. E. J., et al. 2000, , 534, L135

Meinke, J., Böckmann, K., Cohen, S., et al. 2021, The Astrophysical Journal, 913, 88

Meinke, J., Cohen, S., Moore, J., et al. 2023, , 954, 119

Merloni, A., Nandra, K., & Predehl, P. 2020, Nature Astronomy, 4, 634

Merloni, A., Predehl, P., Becker, W., et al. 2012 [[arXiv]1209.3114]

Miller, T. R., Arav, N., Xu, X., & Kriss, G. A. 2020, , 499, 1522

Mintz, A., Jorgenson, R., & Rafelski, M. 2020, 235, 205.06

Miskolczi, A., Heesen, V., Horellou, C., et al. 2019, , 622, A9

Mittal, R., Hudson, D. S., Reiprich, T. H., & Clarke, T. 2009, , 501, 835

Mo, H., van den Bosch, F. C., & White, S. 2010, Galaxy Formation and Evolution

Morganti, R. 2017, Nature Astronomy, 1, 596

Moster, B. P., Naab, T., & White, S. D. M. 2013, , 428, 3121

Moster, B. P., Naab, T., & White, S. D. M. 2018, , 477, 1822

Moster, B. P., Somerville, R. S., Maulbetsch, C., et al. 2010, , 710, 903

Mountrichas, G., Georgantopoulos, I., Ruiz, A., & Kampylis, G. 2019, Monthly Notices of the Royal Astronomical Society, 491, 1727–1735

Mroczkowski, T., Nagai, D., Basu, K., et al. 2019a, , 215, 17

Mroczkowski, T., Nagai, D., Basu, K., et al. 2019b, , 215, 17

Muzzin, A., Marchesini, D., Stefanon, M., et al. 2013, , 777, 18

Naab, T. & Ostriker, J. P. 2017, , 55, 59

Naess, S., Aiola, S., Austermann, J. E., et al. 2020, , 2020, 046

Nelson, D., Byrohl, C., Peroux, C., Rubin, K. H. R., & Burchett, J. N. 2021, , 507, 4445

Nelson, D., Sharma, P., Pillepich, A., et al. 2020, , 498, 2391

Nicastro, F., Elvis, M., Krongold, Y., et al. 2013, , 769, 90

Nicastro, F., Kaastra, J., Krongold, Y., et al. 2018, , 558, 406

Norris, R. P., Hopkins, A. M., Afonso, J., et al. 2011, , 28, 215

Norris, R. P., Marvil, J., Collier, J. D., et al. 2021, , 38, e046

Oke, J. B. & Gunn, J. E. 1983, , 266, 713

Olivares, V., Su, Y., Nulsen, P., et al. 2022, , 516, L101

Oppenheimer, B. D., Crain, R. A., Schaye, J., et al. 2016, , 460, 2157

Oppenheimer, B. D., Schaye, J., Crain, R. A., Werk, J. K., & Richings, A. J. 2018, , 481, 835

Oppermann, N., Junklewitz, H., Greiner, M., et al. 2015, , 575, A118

Oren, A. L. & Wolfe, A. M. 1995, , 445, 624

Orr, M. E., Fielding, D. B., Hayward, C. C., & Burkhart, B. 2021, arXiv e-prints, arXiv:2109.14656

O'Sullivan, E., Giacintucci, S., David, L. P., et al. 2011, , 735, 11

O'Sullivan, S. P., Shimwell, T. W., Hardcastle, M. J., et al. 2023, , 519, 5723

Ota, N., Nguyen-Dang, N. T., Mitsuishi, I., et al. 2023, , 669, A110

Owen, F., Ledlow, M., & Eilek, J. 2002, Highlights of Astronomy, 12, 522

Pakmor, R., Gómez, F. A., Grand, R. J. J., et al. 2017, , 469, 3185

Pakmor, R., van de Voort, F., Bieri, R., et al. 2020, , 498, 3125

Pasini, T., Brüggen, M., Hoang, D. N., et al. 2022, , 661, A13

Pasini, T., Brüggen, M., de Gasperin, F., et al. 2020, Monthly Notices of the Royal Astronomical Society, 497, 2163–2174

Pasini, T., Finoguenov, A., Brüggen, M., et al. 2021, Monthly Notices of the Royal Astronomical Society, 505, 2628–2637

Peeples, M. S., Corlies, L., Tumlinson, J., et al. 2019, , 873, 129

Peeples, M. S., Werk, J. K., Tumlinson, J., et al. 2014, , 786, 54

Péroux, C., Nelson, D., van de Voort, F., et al. 2020, , 499, 2462

Piacitelli, D. R., Solhaug, E., Faerman, Y., & McQuinn, M. 2022

Pierre, M., Valtchanov, I., Altieri, B., et al. 2004, , 2004, 011

Pillepich, A., Nelson, D., Truong, N., et al. 2021, , 508, 4667

Pillepich, A., Springel, V., Nelson, D., et al. 2018, , 473, 4077

Pitrou, C., Coc, A., Uzan, J.-P., & Vangioni, E. 2018, , 754, 1

Planck Collaboration:, Ade, P. A. R., Aghanim, N., et al. 2014, A&A, 564, A45

Planck Collaboration, Aghanim, N., Akrami, Y., et al. 2020, , 641, A6

Planck Collaboration, Ade, P. A. R., Aghanim, N., Alves, M. I. R., et al. 2014, Astronomy Astrophysics, 571, A1

PlanckCollaboration, Aghanim, N., Akrami, Y., et al. 2018 [1807.06209]

Pointon, S. K., Kacprzak, G. G., Nielsen, N. M., et al. 2019, , 883, 78

Pomakov, V. P., O'Sullivan, S. P., Brüggen, M., et al. 2022, , 515, 256

Pratt, C. T. & Bregman, J. N. 2020, The Astrophysical Journal, 890, 156

Predehl, P., Andritschke, R., Arefiev, V., et al. 2021, Astronomy Astrophysics, 647, A1

Pshirkov, M. S., Tinyakov, P. G., & Urban, F. R. 2016, , 116, 191302

Putman, M. E., Peek, J. E. G., & Joung, M. R. 2012, , 50, 491

Rafferty, D. A., McNamara, B. R., Nulsen, P. E. J., & Wise, M. W. 2006, The Astrophysical Journal, 652, 216–231

Ramesh, R., Nelson, D., Heesen, V., & Brüggen, M. 2023, arXiv e-prints, arXiv:2305.11214

Rees, M. J. & Ostriker, J. P. 1977, , 179, 541

Reichardt, C. L., Stalder, B., Bleem, L. E., et al. 2013, , 763, 127

Revaz, Y. & Jablonka, P. 2018, , 616, A96

Robotham, A. S. G. & Obreschkow, D. 2015, , 32, e033

Rossetti, M., Gastaldello, F., Ferioli, G., et al. 2016, , 457, 4515

Rosswog, S. & Brüggen, M. 2011, Introduction to High-Energy Astrophysics

Ruan, J. J., McQuinn, M., & Anderson, S. F. 2015, , 802, 135

Rubin, K. H. R., Prochaska, J. X., Koo, D. C., et al. 2014, , 794, 156

Rudnick, L. 2019, arXiv e-prints, arXiv:1901.09074

Sabater, J., Best, P. N., Hardcastle, M. J., et al. 2019, Astronomy Astrophysics, 622, A17

Sadler, E. M., Jackson, C. A., Cannon, R. D., et al. 2002, , 329, 227

Sandrinelli, A., Falomo, R., Treves, A., Paiano, S., & Scarpa, R. 2020, , 365, 176

Santini, P., Maiolino, R., Magnelli, B., et al. 2014, , 562, A30

Santos, J. S., Rosati, P., Tozzi, P., et al. 2008, Astronomy Astrophysics, 483, 35–47

Sarazin, C. L. 1986, Reviews of Modern Physics, 58, 1

Scannapieco, C., Wadepuhl, M., Parry, O. H., et al. 2012, , 423, 1726

Scannapieco, E. & Oh, S. P. 2004, , 608, 62

Scannapieco, E., Thacker, R. J., & Couchman, H. M. P. 2008, , 678, 674

Schaan, E., Ferraro, S., Amodeo, S., et al. 2021, , 103, 063513

Schaye, J., Crain, R. A., Bower, R. G., et al. 2015, , 446, 521

Schlafly, E. F., Meisner, A. M., & Green, G. M. 2019, The Astrophysical Journal Supplement Series, 240, 30

Schnitzeler, D. H. F. M. 2010, , 409, L99

Scott, K. S., Austermann, J. E., Perera, T. A., et al. 2008, , 385, 2225

Scoville, N., Aussel, H., Brusa, M., et al. 2007, , 172, 1

Sekhar, S., Jagannathan, P., Kirk, B., Bhatnagar, S., & Taylor, R. 2022, , 163, 87

Seppi, R., Comparat, J., Nandra, K., et al. 2023, , 671, A57

Shabala, S. S., Ash, S., Alexander, P., & Riley, J. M. 2008, , 388, 625

Shabala, S. S., Jurlin, N., Morganti, R., et al. 2020, , 496, 1706

Shimwell, T. W., Röttgering, H. J. A., Best, P. N., et al. 2017, , 598, A104

Shimwell, T. W., Tasse, C., Hardcastle, M. J., et al. 2019, , 622, A1

Shull, J. M., Smith, B. D., & Danforth, C. W. 2012, The Astrophysical Journal, 759, 23

Silk, J. & Mamon, G. A. 2012, Research in Astronomy and Astrophysics, 12, 917

Silk, J. & Rees, M. J. 1998, , 331, L1

Sinigaglia, F., Rodighiero, G., Elson, E., et al. 2022, , 935, L13

Smith, B. D., Hallman, E. J., Shull, J. M., & O'Shea, B. W. 2011, , 731, 6

Smolčić, V., Delvecchio, I., Zamorani, G., et al. 2017, Astronomy Astrophysics, 602, A2

Sobrin, J. & SPT-3G Team. 2022, 2022, G14.002

Sokołowska, A., Mayer, L., Babul, A., Madau, P., & Shen, S. 2016, , 819, 21

Somerville, R. S. & Davé, R. 2015a, , 53, 51

Somerville, R. S. & Davé, R. 2015b, , 53, 51

Spacek, A., Scannapieco, E., Cohen, S., Joshi, B., & Mauskopf, P. 2016, , 819, 128

Spacek, A., Scannapieco, E., Cohen, S., Joshi, B., & Mauskopf, P. 2017, , 834, 102

Spacek, A., Scannapieco, E., Cohen, S., Joshi, B., & Mauskopf, P. 2017, The Astrophysical Journal, 834, 102

Springel, V., Pakmor, R., Pillepich, A., et al. 2018, , 475, 676

Stern, D., Assef, R. J., Benford, D. J., et al. 2012, The Astrophysical Journal, 753, 30

Stocke, J. T., Keeney, B. A., Danforth, C. W., et al. 2014, , 791, 128

Sunyaev, R., Arefiev, V., Babyshkin, V., et al. 2021, , 656, A132

Sunyaev, R. A. & Zeldovich, Y. B. 1970, , 7, 20

Sunyaev, R. A. & Zeldovich, Y. B. 1972, Comments on Astrophysics and Space Physics, 4, 173

Sunyaev, R. A. & Zeldovich, Y. B. 1980, , 190, 413

Suresh, J., Nelson, D., Genel, S., Rubin, K. H. R., & Hernquist, L. 2019, , 483, 4040

Suresh, J., Rubin, K. H. R., Kannan, R., et al. 2017, , 465, 2966

Taylor, A. R., Stil, J. M., & Sunstrum, C. 2009, , 702, 1230

Tepper-García, T., Richter, P., Schaye, J., et al. 2011, , 413, 190

Thacker, R. J., Scannapieco, E., & Couchman, H. M. P. 2006, , 653, 86

Thomas, T., Pfrommer, C., & Pakmor, R. 2022, arXiv e-prints, arXiv:2203.12029

Timmerman, R., van Weeren, R. J., Botteon, A., et al. 2022

Tissera, P. B., White, S. D. M., & Scannapieco, C. 2012, , 420, 255

Tozzi, P. 2007, X-ray emission from Clusters of Galaxies

Treu, T., Ellis, R. S., Liao, T. X., & van Dokkum, P. G. 2005, , 622, L5

Tumlinson, J., Peeples, M. S., & Werk, J. K. 2017, , 55, 389

Tumlinson, J., Thom, C., Werk, J. K., et al. 2011, Science, 334, 948

Turner, R. J., Rogers, J. G., Shabala, S. S., & Krause, M. G. H. 2017, Monthly Notices of the Royal Astronomical Society, 473, 4179–4196

Turner, R. J. & Shabala, S. S. 2015, , 806, 59

Ubertosi, F., Gitti, M., Torresi, E., Brighenti, F., & Grandi, P. 2021, , 503, 4627

Vacca, V., Oppermann, N., Enßlin, T., et al. 2016, , 591, A13

van de Voort, F., Springel, V., Mandelker, N., van den Bosch, F. C., & Pakmor, R. 2019, , 482, L85

van Dokkum, P. G., Whitaker, K. E., Brammer, G., et al. 2010, , 709, 1018

Vavagiakis, E. M., Gallardo, P. A., Calafut, V., et al. 2021, , 104, 043503

Veilleux, S., Meléndez, M., Sturm, E., et al. 2013, , 776, 27

Vogelsberger, M., Genel, S., Sijacki, D., et al. 2013, , 436, 3031

Vogelsberger, M., Genel, S., Springel, V., et al. 2014, , 444, 1518

Wampler, E. J., Chugai, N. N., & Petitjean, P. 1995, , 443, 586

Wang, L., Farrah, D., Oliver, S. J., et al. 2013, , 431, 648

Weaver, J. R., Kauffmann, O. B., Ilbert, O., et al. 2022, , 258, 11

Welter, G. L., Perry, J. J., & Kronberg, P. P. 1984, , 279, 19

Werk, J. K., Prochaska, J. X., Cantalupo, S., et al. 2016, , 833, 54

Werk, J. K., Prochaska, J. X., Tumlinson, J., et al. 2014, , 792, 8

Werner, N., McNamara, B. R., Churazov, E., & Scannapieco, E. 2019, , 215, 5

White, S. D. M. & Frenk, C. S. 1991, , 379, 52

Whiting, M., Voronkov, M., Mitchell, D., & Askap Team. 2017, 512, 431

Wiener, J., Pfrommer, C., & Oh, S. P. 2017, , 467, 906

Wieringa, M., Raja, W., & Ord, S. 2020, in Astronomical Society of the Pacific Conference Series, Vol. 527, Astronomical Data Analysis Software and Systems XXIX, ed. R. Pizzo, E. R. Deul, J. D. Mol, J. de Plaa, & H. Verkouter, 591

Willott, C. J., Rawlings, S., Blundell, K. M., & Lacy, M. 1999, Monthly Notices of the Royal Astronomical Society, 309, 1017

Wilson, G. W., Abi-Saad, S., Ade, P., et al. 2020, 11453, 1145302

Wright, E. L., Eisenhardt, P. R. M., Mainzer, A. K., et al. 2010, The Astronomical Journal, 140, 1868–1881

Wright, E. L., Eisenhardt, P. R. M., Mainzer, A. K., et al. 2010, , 140, 1868

Yates-Jones, P. M., Turner, R. J., Shabala, S. S., & Krause, M. G. H. 2022, , 511, 5225